Numerical Prediction of Jet Noise Using Compressible Lattice Boltzmann Method

by

Khalid Noah

A thesis
presented to the University of Waterloo
in fulfillment of the
thesis requirement for the degree of
Doctor of Philosophy
in
Mechanical and Mechatronics Engineering

Waterloo, Ontario, Canada, 2020

Examining Committee Membership

The following served on the Examining Committee for this thesis. The decision of the Examining Committee is by majority vote.

Supervisor	Professor: Fue-Sang Lien Department of Mechanical and Mechatronic Engineering University of Waterloo, Waterloo, Ontario, Canada
External Examiner	Professor: Chao Zhang Department of Mechanical and Materials Engineering Western University, London, Ontario, Canada
Internal Member	Professor: Xianguo Li Department of Mechanical and Mechatronic Engineering University of Waterloo, Waterloo, Canada
Internal Member	Assistant Professor: Jean-Pierre Hickey Department of Mechanical and Mechatronic Engineering University of Waterloo, Waterloo, Ontario, Canada
Internal-external Member	Professor: Francis Poulin Department of Applied Mathematics University of Waterloo, Waterloo, Ontario, Canada

AUTHOR'S DECLARATION

I hereby declare that I am the sole author of this thesis. This is a true copy of the thesis, including any required final revisions, as accepted by my examiners.

I understand that my thesis may be made electronically available to the public.

Abstract

The study of computational fluid dynamics (CFD) encompasses a variety of numerical methods. Some are dependent on macroscopic model representatives, which are solved using the finite volume, finite element, or finite difference method, while others rely on a microscopic description. The lattice Boltzmann method (LBM) is considered a mesoscopic particle method, with its scale lying between macroscopic and microscopic. LBM works well for solving incompressible flow problems, but limitations are associated with the solving of compressible flows, particularly at high Mach numbers. In the research conducted in this thesis, this limitation has been overcome with the use of a higher-order Taylor series expansion of the Maxwell equilibrium distribution function and the Kataoka and Tsutahara (KT) models of compressible flows [1], [2]. A multiple relaxation time (MRT) approach associated with the collision term of the lattice Boltzmann equation (LBE) was adopted in order to enhance the numerical stability of the code, while a large-eddy simulation (LES) scale model was implemented in LBM as a means of simulating compressible jet flows at the high subsonic speeds pertinent to jet noise problems. A three-dimensional simulation was employed using 19- and 15-lattice velocities with D3Q19 and D3Q15 models, respectively. Compressible LBM was also applied for the simulation of both heated and unheated jets in order to demonstrate the ability of the nonadiabatic fifth-order equilibrium distribution

function to solve nonadiabatic compressible flows. The near-field flow physics and noise simulations were performed using the compressible LBM. The results from the LBM simulation were then employed in Kirchhoff's surface integral approach in order to predict far-field jet noise. Because of the ability of the lattice Boltzmann technique to be used in parallel computing and with the goal of improving LBM computational efficiency with respect to the numerical simulations of turbulent flows in predicting far-field noise, the final step in this research was to use compute unified device architecture (CUDA) for implementing the LBM in a graphics processing unit (GPU), thus creating a hybrid code, LBM-MRT-LES, through the utilization of the Kirchhoff integral method, a powerful tool for simulating aeroacoustics problems.

Acknowledgements

First and foremost, I am honoured to take this opportunity to express my warmest gratitude to my supervisor, Fue-Sang Lien, for his continual support for my Ph.D. studies and research. Professor Lien's patience, motivation, enthusiasm, and immense knowledge have been deeply appreciated. His careful guidance and thoughtful suggestions have been an enormous help throughout my thesis preparation, providing me with all the necessary support and scientific consultation to carry out my work, as well as inspiring me to improve and successfully implement my research.

I would also like to thank the examining committee members for their efforts in reviewing my thesis and providing expert and helpful suggestions.

Finally, I wish to thank my family for all their care and help, with special gratitude going to my wife for her sacrifice, understanding, patience, encouragement, and love.

Dedication

I dedicate my dissertation to my family – my dear and sweet wife, Kadria; my children, Farah, Seba, Idris, and Hala; my parents; and my brothers and sisters.

Table of contents

List of Figures

List of Tables

Nomenclature

c	Particle velocity
C	Smagorinsky constant
C_i	Discrete velocities
c_s	Speed of sound
c_∞	Speed of sound in freestream/ambient conditions
D	Special diagonal matrix
D_j	Diameter of the jet exit
D_{lbm}	Diameter of the jet exit (LBM units)
f	Distribution function
f^{eq}	Local equilibrium distribution function
G	Green function
M	Transformation matrix
m	Moment
m^{eq}	Equilibrium moment
M_j	Jet Mach number = $\frac{U_j}{c_j}$
p	Pressure
$\acute{p}$	Sound pressure
Q_{ij}	Non-equilibrium stress tensor
R	Specific gas constants

r	Radial coordinate
Re_d	Reynolds number
rms	Root mean square
S	Diagonal matrix
S_0	Kirchhoff surface
St	Strouhal number
$\lvert\bar{S}\rvert$	Magnitude of the large-scale strain-rate tensor
T_∞	Freestream/ambient temperature
T_j	Jet static temperature at the jet exit
T_{ij}	Lighthill's stress tensor
u	Instantaneous streamwise velocity (m/s)
u_x/U_j	Fluctuating streamwise velocity (m/s)
U	Mean velocity value
U_c	Local centerline velocity (m/s)
U_∞	Freestream/ambient velocity
U_j	Jet velocity at the jet exit, assuming a fully expanded flow
u_x	Streamwise velocity
ν	Kinematic viscosity
x	Streamwise coordinate
y	Transverse coordinate

Φ Flow field variable (acoustic variable)

τ Relaxation time

τ' Retarded time

τ_w Effective relaxation time

ρ Fluid density

γ Specific heat ratio

λ Wavelength

η Control parameter

v_t Turbulent viscosity

v_0 Laminar viscosity

δ_{ij} Kronecker delta function

Δ Filter width

Δt Time step

Δt_{lbm} Time step (LBM units)

Δx_{lbm} Grid spacing, *x*-direction (LBM units)

Δy_{lbm} Grid spacing, *y*-direction (LBM units)

Δz_{lbm} Grid spacing, *z*-direction (LBM units)

ω Collision frequency

ω_i Lattice weight factors

Ω Collision operator

Acronyms

BGK Bhatnagar, Gross, and Krook

CAA Computational aeroacoustics

CFD Computational fluid dynamics

CFM Computational fluid mechanics

CUDA Compute unified device architecture

DNS Direct numerical simulation

FDM Finite difference method

FEM Finite element method

FVM Finite volume method

FW-H Ffowcs Williams and Hawkings

HO High-Order equilibrium distribution function

GPU Graphics processing unit

KSIM Kirchhoff's surface integral method

KT Kataoka and Tsutahara

LBE Lattice Boltzmann equation

LBM Lattice Boltzmann method

LES Large-eddy simulation

LGA Lattice gas automata

MRT Multiple relaxation time

RANS Reynolds-averaged Navier-Stokes

RLBE Relaxation lattice Boltzmann equation

SIMT Single instruction, multiple threads

SRT Single relaxation time

SPL Sound pressure level

SGS Subgrid scale

URANS Unsteady Reynolds-averaged Navier-Stokes

Chapter 1

Introduction

1.1 Background

Fluid dynamics is one of two branches of fluid mechanics; it involves the study of flow behaviour and how it is affected by boundary forces. The other branch, called fluid statics, deals with fluids at rest. Historically, the ancient Greeks applied relatively simplistic methods for solving fluid mechanics algebraic equations, which were used until Claude-Louis Navier (1822) and George Gabriel Stokes (1842) derived the Navier-Stokes equations. These equations are nonlinear partial differential equations in the general case, enabling flow to be described in a real situation. To solve Navier-Stokes equations, a numerical method is used for approximating the solutions of equations when exact solutions cannot be determined via algebraic methods. This strategy has given birth to a new branch of fluid dynamics called computational fluid dynamics (CFD).

Today, since computers have become powerful tools for simulating large-domain flows within a satisfactory run time, CFD has become the main focus of fluid dynamics. The core of CFD is to numerically solve the governing equations that govern flows based on the use of initial and boundary conditions for identifying

the behaviour of the flow parameters (e.g., velocity, density, pressure) in flow fields. In computational fluid mechanics, either macroscopic or microscopic models are employed for solving problems related to fluid mechanics. For solving the Navier-Stokes or the Euler equation, the governing equations must first be discretized through the application of techniques such as the finite volume method (FVM), the finite element method (FEM), or the finite difference method (FDM). In most CFD methods, they required the adoption of an advection scheme (e.g., central, upwind, hybrid) in order to solve the resulting discretized linearized system. The macroscopic model works well in many situations, but if complex geometry is involved, difficulties will arise with respect to solving the nonlinear differential equations [3].

A mesoscopic approach (e.g., the lattice Boltzmann equation (LBE)) provides an impressive bridge between the microscopic and macroscopic scales [4]. The LBE is a new methodology based on microscopic particle models and mesoscopic kinetic equations [5]. The basic idea behind LBM is to construct simplified kinetic models that incorporate only the essential physics principles underlying the microscopic or mesoscopic processes so that the averaged values of the macroscopic properties obey the desired macroscopic equations. Unlike other conventional CFD methods, kinetic-theory-based LBM simulates the flow domain by tracking the evolution of the particle distribution function and then accumulates the distribution in order to

obtain averaged values for the macroscopic properties, such as density, velocity, and pressure [6].

Over the past two decades, LBM has emerged as a competitive scheme for simulating a number of complex flows. It has also enabled other numerical limitations to be overcome [7], such as difficulties associated with running in a parallel computing environment. Since physical insight is clear, and it is a particle-based method, LBM can be successfully implemented in a parallel computing environment [8] when an explicit time-stepping scheme is employed. LBM is effective for solving incompressible flow problems, but it is still in its infancy with respect to the solving of compressible turbulent flow problems, particularly at high Mach numbers involving shock waves. Over the last few years, much of LBM development has been directed toward solving compressible turbulent flows [9]. In the work presented in this thesis, priority has been given to research relevant to the case study that was conducted for this thesis, with the goal of solving a compressible flow at a high subsonic Mach number.

1.2 Motivation and objectives

Computational fluid dynamics software, such as ANSYS FLUENT and STAR-CCM+, has become a valuable tool for solving both compressible flows and aeroacoustics problems. At the same time, block-structured-grid and unstructured-grid methods, together with specifications for compatible boundary conditions, have

been introduced to traditional CFD for solving flows in complex geometries. The goal of the research presented in this thesis was to use compressible LBM in order to develop a solution procedure for predicting the aeroacoustics related to turbulent jet flow.

LBM has been gaining in popularity in recent years and is ideally suited for parallel computing [10]. However, it can present difficulties when applied at high Mach numbers. The root cause of these problems is that the Maxwellian distribution function in an exponential form for relative velocity cannot be easily integrated into the velocity space using the Gauss Hermite quadrature. This challenge can be addressed with the use of a truncated Taylor series expansion of the Maxwell function in terms of the Mach number in an equilibrium condition [11] and the application of the explicit form of the Hermite polynomials, at the second and third orders.

In this research, Hermite polynomials at the sixth order were employed in order to avoid the LBM compressibility limitation. For turbulence flow simulation purposes, multiple relaxation times (MRT) were also implemented in the LBM, and the models developed by Kataoka and Tsutahara (KT) [1] in 2004 were applied for the compressible Euler equations. Kataoka and Tsutahara found that the use of their models prevented a free choice of specific heat ratio, so they developed new models

(D1Q5, D2Q9, D3Q15) of Euler equations and (D2Q16) of Navier-Stokes equations [1]. They also introduced a new constant related to the specific heat ratio [1].

Based on the above considerations, the research presented here involved the application of a large eddy simulation (LES) in the D3Q15 and D3Q19 models in order to simulate a jet flow and the far-field aeroacoustics around a jet in three dimensions (3D). The LES scale model was implemented in LBM as a means of simulating compressible jet flows at the high subsonic speeds associated with jet noise problems. The results obtained from the LBM-LES simulation were used for studying and analyzing near-field jet acoustics and the characterization of their properties. As well, the results obtained from simulating the near-field jet acoustics were also used for predicting far-field jet noise when LBM-LES is combined with the Kirchhoff surface integral method as a hybrid approach to assessing far-field noise. As a final element, because of LBM's efficacy for use in parallel computing, it was implemented in a GPU, thus demonstrating the potential of LBM as a powerful technique for simulating aeroacoustics problems.

1.3 Focus of this research

As reviewed and discussed in the body of this thesis, the existing literature related to LBM reveals its limitations with respect to the solving of compressible flows. These limitations arise from the use of the Maxwell distribution function, which is in the exponential form of particle velocity and cannot be directly applied

in the LBE, which forms the basis of the kinetic theory of gases and provides a simplified explanation of many fundamental gaseous properties, including diffusion and pressure.

The specific objectives of the work conducted for this thesis and the new contributions arising from this research are as follows.

- LBM works well for solving incompressible flow problems, but a number of limitations are associated with solving compressible flows, particularly at high Mach numbers. An improved lattice Boltzmann model for compressible flow problems is therefore presented here. A higher-order Taylor series expansion of the Maxwell equilibrium distribution function has been employed for overcoming the LBM limitations with respect to solving flows involving high Mach numbers.
- The study presented here represents an integration of other research work, such as the KT models for compressible flows, in order to simulate the aeroacoustics of subsonic jets at high Reynolds numbers.
- To obtain stability and increase LBM capability so that high Reynolds number flows can be simulated, this work also incorporated an MRT approach into the compressible LBM models.
- In this thesis work, LBM was used for simulating turbulent jet flows using subgrid modelling for LBM based on LES, which is currently widely used in

the industry for simulating turbulent flows because of its relatively low computational needs compared to direct numerical simulation (DNS).

- A further goal of the work was to solve the LBE in a 3D (D3Q19 and D3Q15) simulation in order to provide accurate results similar to those derived from the experimental method applied to the study of far-field jet noise.
- One of the main contributions of our research was implementing the Kirchhoff's integral method into compressible LBM models through the application of MRT combined with LES. The combined methods permit the prediction of propagated sound based on the pressure and its derivatives in time and space obtained on Kirchhoff's control surface located in the linear flow region.
- A final objective was to implement the lattice Boltzmann method on a GPU for Predicting Near-Field and Far-field Jet Noise, which is beneficial and reduces the time by 120X compared to employing a CPU.

1.4 Thesis outline

This thesis is divided into nine chapters. Following the introduction (Chapter 1), Chapter 2 provides an overview of LBM. The chapter also presents a literature review of the fundamental conventional LBM for solving incompressible flows in 3D for single and multiple relaxation times. Chapter 3 explains the LBM limitations with respect to solving high Mach number flows as well as techniques for

overcoming these limitations through the application of high-order distribution functions (HO) and the use of KT models. Chapter 4 describes the implementation of the LES method in LBM for single and multiple relaxation times. In Chapter 5, integral methods in computational aeroacoustics are introduced, with a focus on Kirchhoff's surface integral method (KSIM) and its use for predicting far-field noise, as detailed in Chapter 7 and Chapter 8. Chapter 6 presents the application of alternative methods (high-order equilibrium distribution function and KT model) for simulating free jet flows for a variety of conditions as well as a comparison of the results with the available experimental data. Chapter 7 is concentrated on an examination of the near-field and far-field jet acoustics using the lattice Boltzmann approach. Chapter 8 explains the application of the LBM results in KSIM for predicting far-field jet noise as well as the implementation of LBM in a graphics processing unit (GPU) in order to reduce the simulation time and create a new simulation technique for this research area. The final chapter offers a brief conclusion for the thesis and indicates possible directions for future research related to this topic.

Chapter 2

Incompressible Lattice Boltzmann Method

2.1 Introduction

In the late 1980s, the lattice Boltzmann method (LBM) grew out of the lattice gas model. Both methods are based on the fundamental behaviour that gas molecules exhibit when they move forward and scatter as they collide with one another, but LBM avoids the major disadvantages of its predecessor while retaining its strengths. It also facilitated a stronger theoretical grounding in the physical theory of gases [12]. More recently, researchers have been attracted to LBM for a number of reasons, including its simplicity, its scalability on parallel computers, and its efficiency with respect to simulating complex geometries. LBM has thus become a new and promising computational fluid dynamics (CFD) method for solving computational fluid mechanics problems, such as those related to porous media, multiphase flow, and binary and ternary complex flows [13].

2.2 Lattice Boltzmann method

LBM was developed from lattice gas automata (LGA), which are a type of cellular automaton used for simulating fluid flows [14]. Lattice Boltzmann is a promising method for solving nonlinear partial differential equations and is quite different from its traditional CFD counterpart. The motivation for the development

of the Boltzmann equation lies in a desire to deduce the macroscopic behaviour of a gas based on its microscopic properties [15].

The Boltzmann equation for a system without an external force can be expressed as

$$\frac{\partial f_i}{\partial t} + \vec{c}_i \,.\nabla f_i = \Omega \tag{2.1}$$

where Ω is the collision operator, f_i is the distribution function, $\vec{c}_i$ is the lattice velocity, and *t* is time.

As is evident in Eq. (2.1), solving the lattice Boltzmann equation (LBE) is quite complicated due to the collision term. In 1954, Bhatnagar, Gross, and Krook (BGK) [16] proposed a simplification of the collision integral operator as a means of facilitating the calculation of the Boltzmann equation. The BGK model is based on the assumption that the net effect of collisions causes the distribution function to relax toward its local equilibrium distribution with a characteristic time equal to the mean free time, as expressed below:

$$\Omega = \omega(f^{eq} - f) = \frac{\Delta t}{\tau}(f^{eq} - f) \tag{2.2}$$

where $\omega = {\Delta t}/{\tau}$ is the collision frequency, τ is the relaxation factor, and f^{eq} is the local equilibrium distribution function. Substituting Eq. (2.2) into Eq. (2.1) gives

$$\frac{\partial f}{\partial t} + \vec{c}.\nabla f = \frac{\Delta t}{\tau}(f^{eq} - f) \tag{2.3}$$

or, in a specific particle velocity direction,

$$\frac{\partial f_i}{\partial t} + \vec{c}_i . \nabla f_i = \frac{\Delta t}{\tau}\left(f_i^{eq} - f_i\right) \tag{2.4}$$

This equation can be discretized in time using the "streaming operator," as in

$$f_i(x + \vec{c}_i \Delta t, t + \Delta t) - f_i(x, t) = \frac{\Delta t}{\tau}\left(f_i^{eq}(x, t) - f_i(x, t\right) \tag{2.5}$$

where f_i is the distribution function; f_i^{eq} is the equilibrium function; $\vec{c}_i$ is the particle velocity; and Δt and Δx are time and space increments, respectively.

As can be seen, the beauty of this equation lies in its simplicity, and it can be applied to many fluid mechanics problems. In LBM, the physical domain is different from the solution domain. Although the mapping between the two domains is an easy process, it is more intuitive to present results in physical dimensions.

The Maxwell equilibrium distribution function f^{eq} is given as

$$f^{eq}(\rho, \mathrm{u}, \theta) = \rho(2\pi\theta)^{-D/2} e^{\left[\frac{(\vec{c} - \mathrm{u}^2)}{2\theta}\right]} \tag{2.6}$$

where D=3 and $\theta = RT$

The discrete equilibrium distribution f^{eq} can be derived from an expansion of the Maxwell-Boltzmann distribution function f^{eq} in Hermite polynomials. Using the Gauss-Hermite quadrature, the following discrete equilibrium distribution f^{eq} can be obtained in terms of Mach numbers as follows:

$$f_i^{eq}(x,t) = \omega_i \rho \left(1 + \frac{3\vec{c}_i \,.\, \mathrm{u}}{c_s^2} + \frac{9(\vec{c}_i \,.\, \mathrm{u})^2}{2c_s^4} - \frac{3\mathrm{u}^2}{2c_s^2} \right) + O(\mathrm{u}^3) \qquad (2.7)$$

where $\vec{c}_s$ is the speed of sound $= \frac{\vec{c}_i}{\sqrt{3}}$, $\vec{c}_i$ is a unit vector along the streaming direction $\vec{c}_i = \frac{\Delta x}{\Delta t} i + \frac{\Delta y}{\Delta t} j = 1$, lead to $\Delta t = \Delta x = \Delta y = 1$ and $\mathrm{u} = ui + vj$, where i and j are unit vectors along the x and y directions, respectively. The final element, ω_i, represents the lattice weight factors and must satisfy the relation

$$\sum_{i=0}^{i=n-1} \omega_i = 1 \qquad (2.8)$$

where n is the total number of discrete particle velocities, which is dependent on the lattice model (e.g., in the case of D3Q19, n = 19).

2.3 Equilibrium distribution function

The Maxwell-Boltzmann distribution is a statistical probability distribution used for describing particle speeds for ideal gases when the particles move freely inside a stationary container [13]. The interaction between particles is neglected, except for very brief collisions that lead to minor changes in energy and momentum within the environment. A good choice of the equilibrium distribution function is a key factor in the successful application of LBM to a wide range of fluid flow problems in different conditions [17]. For this reason, it seemed necessary to choose equilibrium distribution functions for compressible LBM that differ from those used

in incompressible LBM. The 3D version of Maxwell's distribution function can be written in a number of formulas as follows:

$$f^{eq} = \frac{\rho}{2\pi/3} e^{-\frac{3}{2}(\vec{c}_i - \mathrm{u})^2} \tag{2.9}$$

f^{eq} can be written in terms of the macroscopic quantities of density ρ and fluid velocity u as

$$f^{eq} = \frac{\rho}{2\pi/3} e^{-\frac{3}{2}\left(\vec{c}_i{}^2\right)} e^{\frac{3(\vec{c}_i.\mathrm{u} - \mathrm{u}^2)}{2}} \tag{2.10}$$

By Taylor series expansion the equilibrium distribution function along a discretized velocity direction is then given as follows:

$$f^{eq} = \frac{\rho}{\frac{2\pi}{3}} e^{-\frac{3}{2}\left(\vec{c}_i{}^2\right)} \left[1 + 3(\vec{c}_i.\mathrm{u}) - \frac{3}{2}\mathrm{u}^2 + \ldots\right] \tag{2.11}$$

2.4 Single relaxation time

The collision operator can be approximated as in the BGK formulation, which is commonly referred to as the lattice BGK (LBGK) or the single relaxation time (SRT) model. This collision model is numerically the most effective, but not for highly advection-dominated transport phenomena [18]. In the case when the Peclet number is below 10, $\tau = 1$ could be selected. A BGK approximation for the collision operator can be expressed as follows:

$$\Omega_i = -\frac{\Delta t}{\tau}\left[f_i(x,t) - f_i^{eq}(x,t)\right] \tag{2.12}$$

where τ is the relaxation time.

LBM with SRT in the collision operator is computationally efficient and algorithmically simple, but this approach tends to be less stable, particularly for high-Reynolds-number flows [19]. To alleviate the potential instability problems associated with LBM-SRT, other researchers introduced a multiple relaxation times (MRT) model, as described below.

2.6 Multiple relaxation times

The relaxation lattice Boltzmann equation (RLBE) was introduced by Higuera and Jimenez in 1989 [20]. The RLBE allowed some of the challenges associated with lattice gas automata (LGA) to be addressed and also permitted the resolution of 3D problems. In 1986, d'Humières [21], [22] introduced a generalized LBM based on the concept of using MRT to overcome the shortcomings of the BGK model, i.e., the numerical instability caused by low viscosity when an SRT is adopted.

As we know from the BGK approximation, the LBM formula is

$$f_i(x + \vec{c}_i\Delta t, t + \Delta t) - f_i(x,t) = -\Omega\left[f_i(x,t) - f_i^{eq}(x,t)\right] \tag{2.13}$$

where Ω is the collision operator, which can be based on either a single or multiple relaxation times (i.e., SRT or MRT). In the case of MRT, the collision operator is a

matrix. The collision step will then be in the moment space rather than in the velocity space, as follows:

$$f_i(x + \vec{c}_i\Delta t, t + \Delta t) - f_i(x,t) = -M^{-1}S[m(x,t) - m^{eq}(x,t)] \qquad (2.14)$$

Here, m is a *n*-component moment vector,

$$m = (m_0, m_1, m_2, .. m_{n-1})^T \qquad (2.15)$$

and m^{eq} is its local equilibrium counterpart. A linear transformation between velocity and momentum spaces can be achieved by solving Eq. (2.16) below. The transformation should be carried out explicitly, mapping *f* to *m* and vice versa.

$$m = Mf \text{ and } f = M^{-1}m \qquad (2.16)$$

There are many MRT models, such as D2Q9, D3Q15, and D3Q19. For the work presented in this thesis, D3Q15 and D3Q19 lattice models were employed. The lattice arrangement for a D3Q15 model is illustrated in Figure 2.1.

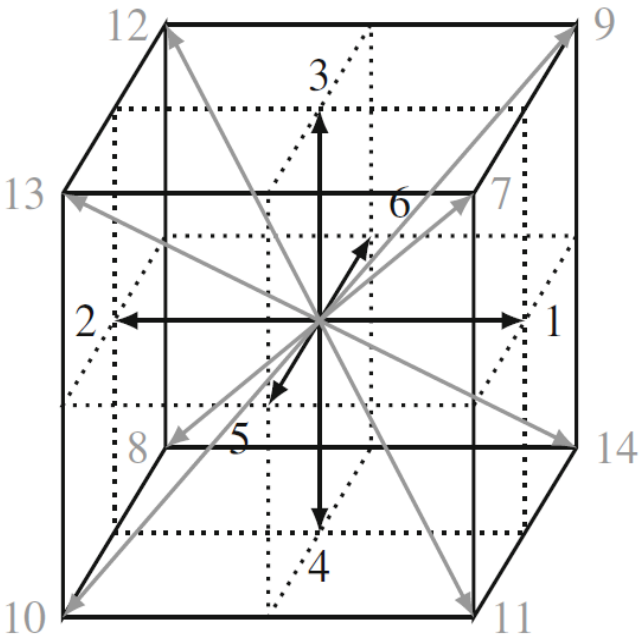

Figure 2.1: D3Q15 lattice arrangement for 3D problems.

In the D3Q15 lattice model, the discrete velocities are

$$c_i = \begin{cases} (0,0,0) & i = 0 \\ (\pm 1,0,0), (0,\pm 1,0), (0,0,\pm 1) & i = 1,2,\dots,6 \\ (\pm 1,\pm 1,\pm 1) & i = 7,8,\dots,14 \end{cases} \qquad (2.17)$$

The moment vectors correspond to Hermite polynomials of the LBM velocities c_i and can be derived from the conservation equations to get the corresponding moments components of the macroscopic density, momentum vector and stress. [23]

$$m = \left(\rho, e, \epsilon, j_x, q_x, j_y, q_y, j_z, q_z, 3p_{xx}, p_{ww}, p_{xy}, p_{yz}, p_{zx}, t_{xyz}\right)^T \qquad (2.18)$$

The corresponding equilibrium moments are as follows:

$$m^{eq} = \left(1, \mathrm{u}^2 - 1, -1, u_x, -\frac{7}{3}u_x, u_y, -\frac{7}{3}u_y, u_z, -\frac{7}{3}u_z - 3u_x^2 - \mathrm{u}^2, u_y^2 - u_z^2, u_x u_y, u_y u_z, u_z u_x, 0\right) \tag{2.19}$$

For the D3Q15 lattice model, the transformation matrix M in Eq. (2.16) is as exemplified below:

$$\boldsymbol{M} = \begin{pmatrix} 1 & 1 & 1 & 1 & 1 & 1 & 1 & 1 & 1 & 1 & 1 & 1 & 1 & 1 & 1 \\ -2 & -1 & -1 & -1 & -1 & -1 & -1 & 1 & 1 & 1 & 1 & 1 & 1 & 1 & 1 \\ 16 & -4 & -4 & -4 & -4 & -4 & -4 & 1 & 1 & 1 & 1 & 1 & 1 & 1 & 1 \\ 0 & 1 & -1 & 0 & 0 & 0 & 0 & 1 & -1 & 1 & -1 & 1 & -1 & 1 & -1 \\ 0 & -4 & 4 & 0 & 0 & 0 & 0 & 1 & -1 & 1 & -1 & 1 & -1 & 1 & -1 \\ 0 & 0 & 0 & 1 & -1 & 0 & 0 & 1 & 1 & -1 & -1 & 1 & 1 & -1 & -1 \\ 0 & 0 & 0 & -4 & 4 & 0 & 0 & 1 & 1 & -1 & -1 & 1 & 1 & -1 & -1 \\ 0 & 0 & 0 & 0 & 0 & 1 & -1 & 1 & 1 & 1 & 1 & -1 & -1 & -1 & -1 \\ 0 & 0 & 0 & 0 & 0 & -4 & 4 & 1 & 1 & 1 & 1 & -1 & -1 & -1 & -1 \\ 0 & 2 & 2 & -1 & -1 & -1 & -1 & 0 & 0 & 0 & 0 & 0 & 0 & 0 & 0 \\ 0 & 0 & 0 & 1 & 1 & -1 & -1 & 0 & 0 & 0 & 0 & 0 & 0 & 0 & 0 \\ 0 & 0 & 0 & 0 & 0 & 0 & 0 & 1 & -1 & -1 & 1 & 1 & -1 & -1 & 1 \\ 0 & 0 & 0 & 0 & 0 & 0 & 0 & 1 & 1 & -1 & -1 & -1 & -1 & 1 & 1 \\ 0 & 0 & 0 & 0 & 0 & 0 & 0 & 1 & -1 & 1 & -1 & -1 & 1 & -1 & 1 \\ 0 & 0 & 0 & 0 & 0 & 0 & 0 & 1 & -1 & -1 & 1 & -1 & 1 & 1 & -1 \end{pmatrix}.$$

The diagonal matrix S in Eq. (2.14) is

$$S = \left(0, s_e, s_\varepsilon, 0, s_q, 0, s_q, 0, s_q, s_v, s_v, s_v, s_v, s_v, s_t\right) \tag{2.20}$$

The kinematic and the bulk viscosities in relation to s_v and s_e are

$$\nu = \frac{1}{3}\left(\frac{1}{s_v} - \frac{1}{2}\right)\Delta_t \quad , \quad \zeta = \frac{2}{9}\left(\frac{1}{s_e} - \frac{1}{2}\right)\Delta_t \tag{2.21}$$

The lattice arrangement for the D3Q19 model is illustrated in Figure 2.2.

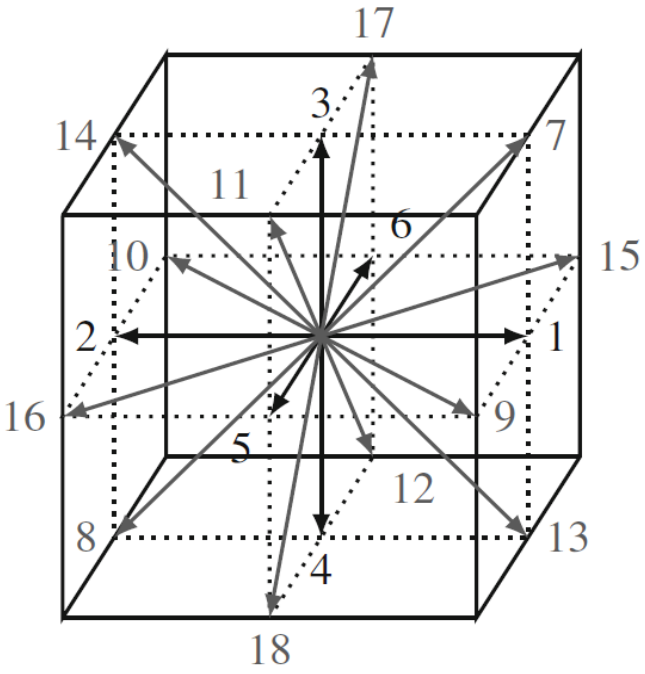

Figure 2.2: D3Q19 lattice arrangement for 3D problems.

In the D3Q19 model, the discrete velocities are

$$c_i = \begin{cases} (0;\ 0;\ 0) & i = 0 \\ (\pm 1;\ 0;\ 0);\ (0; \pm 1;\ 0);\ (0;\ 0\ \pm\ 1) & i = 0,2, \dots, 6 \\ (\pm 1; \pm 1;\ 0);\ (\pm 1;\ 0; \pm 1);\ (0; \pm 1; \pm 1) & i = 7,8, \dots, 18 \end{cases} \quad (2.22)$$

The corresponding moments for this model are [23]

$$m = \left(\rho, e, \epsilon, j_x, q_x, j_y, q_y, j_z, q_z, 3p_{xx}, 3\pi_{xx},\ p_{ww}, \pi_{ww,} p_{xy}, p_{yz}, p_{zx}, t_x, t_y, t_z\right)^T \quad (2.23)$$

and the corresponding equilibrium moments are

$$m^{eq} = \rho\left(-11 + 19\mathrm{u}^2, \alpha\,, \beta\mathrm{u}^2\,, u_x, -\frac{2}{3}u_x, u_y, -\frac{2}{3}u_y, u_z, -\frac{2}{3}u_z, 3u_x^2 - \mathrm{u}^2, \frac{\gamma p_{xx}^{eq}}{\rho}, u_y^2 - u_z^2, \frac{\gamma p_{ww}^{eq}}{\rho}, u_x u_y, u_y u_z, u_z u_x, 0\right) \tag{2.24}$$

where the free parameters α, β, and γ are

$$\alpha = 3\,, \beta = -\frac{11}{2}, \quad \text{and } \gamma = -\frac{1}{2} \tag{2.25}$$

The transformation matrix M is as follows:

$$M = \begin{pmatrix}
1 & 1 & 1 & 1 & 1 & 1 & 1 & 1 & 1 & 1 & 1 & 1 & 1 & 1 & 1 & 1 & 1 & 1 & 1 \\
-30 & -11 & -11 & -11 & -11 & -11 & -11 & 8 & 8 & 8 & 8 & 8 & 8 & 8 & 8 & 8 & 8 & 8 & 8 \\
12 & -4 & -4 & -4 & -4 & -4 & -4 & 1 & 1 & 1 & 1 & 1 & 1 & 1 & 1 & 1 & 1 & 1 & 1 \\
0 & 1 & -1 & 0 & 0 & 0 & 0 & 1 & -1 & 1 & -1 & 1 & -1 & 1 & -1 & 0 & 0 & 0 & 0 \\
0 & -4 & 4 & 0 & 0 & 0 & 0 & 1 & -1 & 1 & -1 & 1 & -1 & 1 & -1 & 0 & 0 & 0 & 0 \\
0 & 0 & 0 & 1 & -1 & 0 & 0 & 1 & 1 & -1 & -1 & 0 & 0 & 0 & 0 & 1 & -1 & 1 & -1 \\
0 & 0 & 0 & -4 & 4 & 0 & 0 & 1 & 1 & -1 & -1 & 0 & 0 & 0 & 0 & 1 & -1 & 1 & -1 \\
0 & 0 & 0 & 0 & 0 & 1 & -1 & 0 & 0 & 0 & 0 & 1 & 1 & -1 & -1 & 1 & 1 & -1 & -1 \\
0 & 0 & 0 & 0 & 0 & -4 & 4 & 0 & 0 & 0 & 0 & 1 & 1 & -1 & -1 & 1 & 1 & -1 & -1 \\
0 & 2 & 2 & -1 & -1 & -1 & -1 & 1 & 1 & 1 & 1 & 1 & 1 & 1 & 1 & -2 & -2 & -2 & -2 \\
0 & -4 & -4 & 2 & 2 & 2 & 2 & 1 & 1 & 1 & 1 & 1 & 1 & 1 & 1 & -2 & -2 & -2 & -2 \\
0 & 0 & 0 & 1 & 1 & -1 & -1 & 1 & 1 & 1 & 1 & -1 & -1 & -1 & -1 & 0 & 0 & 0 & 0 \\
0 & 0 & 0 & -2 & -2 & 2 & 2 & 1 & 1 & 1 & 1 & -1 & -1 & -1 & -1 & 0 & 0 & 0 & 0 \\
0 & 0 & 0 & 0 & 0 & 0 & 0 & 1 & -1 & -1 & 1 & 0 & 0 & 0 & 0 & 0 & 0 & 0 & 0 \\
0 & 0 & 0 & 0 & 0 & 0 & 0 & 0 & 0 & 0 & 0 & 0 & 0 & 0 & 0 & 1 & -1 & -1 & 1 \\
0 & 0 & 0 & 0 & 0 & 0 & 0 & 0 & 0 & 0 & 0 & 1 & 1 & -1 & -1 & 0 & 0 & 0 & 0 \\
0 & 0 & 0 & 0 & 0 & 0 & 0 & 1 & -1 & 1 & -1 & -1 & 1 & -1 & 1 & 0 & 0 & 0 & 0 \\
0 & 0 & 0 & 0 & 0 & 0 & 0 & -1 & -1 & 1 & 1 & 0 & 0 & 0 & 0 & 1 & -1 & 1 & -1 \\
0 & 0 & 0 & 0 & 0 & 0 & 0 & 0 & 0 & 0 & 0 & 1 & 1 & -1 & -1 & -1 & -1 & 1 & 1
\end{pmatrix}.$$

The diagonal matrix S in Eq. (2.14) is

$$S = \left(0, s_e, s_\varepsilon, 0, s_q, 0, s_q, 0, s_q, s_v, s_\pi s_v, s_\pi, s_v, s_v, s_v, s_t, s_t, s_t\right) \qquad (2.26)$$

The kinematic and the bulk viscosities in relation to s_v and s_e are

$$\nu = \frac{1}{3}\left(\frac{1}{s_v} - \frac{1}{2}\right)\Delta_t \qquad , \quad \zeta = \frac{2}{9}\left(\frac{1}{s_e} - \frac{1}{2}\right)\Delta_t \qquad (2.27)$$

2.6 Boundary and initial conditions

A CFD methodology is highly dependent on the surrounding environment. This influence is delineated mathematically via the prescription of appropriate boundary conditions, which play a key role, since they determine the selection of solutions with external constraints. LBM has recently been proposed as an alternative numerical method for simulating fluid mechanics problems that are governed by the Euler equation or the Navier-Stokes equations. Unlike traditional CFD methods that solve for macroscopic variables such as velocity and density, LBM is a mesoscopic particle method based on a particle distribution function [6]. After the distribution function for the flow domain has been solved, the macroscopic quantities can be easily obtained through moment integrations of the distribution function. Unique values for fluid density, velocity, pressure, and temperature can be determined from the distribution function. The initial and boundary conditions have a significant influence on LBM accuracy, stability, and convergence. In LBM applications, the treatment of initial and boundary conditions is therefore crucial.

Several different LBM boundary condition schemes have been devised and adopted: the periodic scheme, the bounce-back scheme, the curved boundary scheme, etc. This section discusses only the boundary conditions employed for this research. For simplicity, the example of the implementation of the boundary condition for the D2Q9 model is explained.

2.6.1 Bounce-back scheme

Bounce-back boundaries constitute a straightforward scheme whose simplicity has played a major role in making LBM popular among CFD researchers [24]. A bounce-back scheme can be used for simulating a fluid flow characterized by complex geometries such as those found in two-phase flow and porous media. The feature of this boundary scheme is that one needs only to designate a particular node as a solid obstacle by determining the boundary nodes required in the geometry, following which, the particle incoming toward the solid boundary is bounced back into the flow domain.

As can be seen in Figure 2.3, the distribution function can be obtained in all directions except ones toward the domain. Thus, f_0, f_1,, f_3, f_4, f_7, and f_8 are known from the flow simulation, and f_2, f_5, and f_6 are unknown but can be derived from the following equations. For example, f_7 at node assume it (i, j) is equal to f_7 of node $(i+1, j+1)$, similarly for f_8 which is came from node $(i-1, j+1)$ to be after

streaming equal to f_8 at node $(i, j+1)$. In a bounce-back scheme, the boundary condition must be applied after the streaming process, as follows:

$$f_7(i,j) = f_7(i+1, j+1)$$
$$f_8(i-1, j+1) = f_8(i, j+1) \tag{2.28}$$

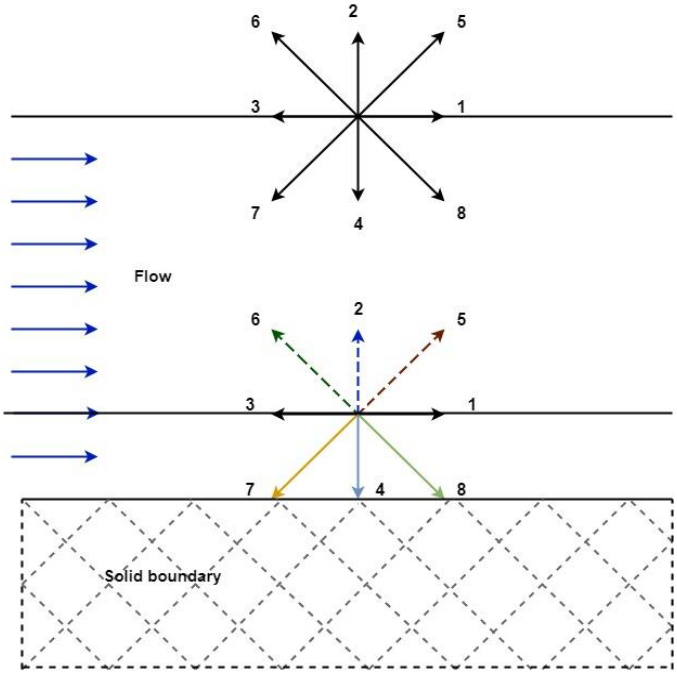

Figure 2.3: Bounce-back scheme.

2.6.2 Simple bounce-back scheme

For this research, a simple bounce-back scheme was also used by simply letting $f_5 = f_7$; $f_2 = f_4$, and $f_6 = f_8$, where f_7, f_4, and f_8 are known from the streaming process. The main idea of the bounce-back scheme is to set these unknown

distribution functions to be equal to their opposite directions following the streaming process. As shown in Figure 2.4, the lattices are located directly at the solid surface rather than at the middle plane.

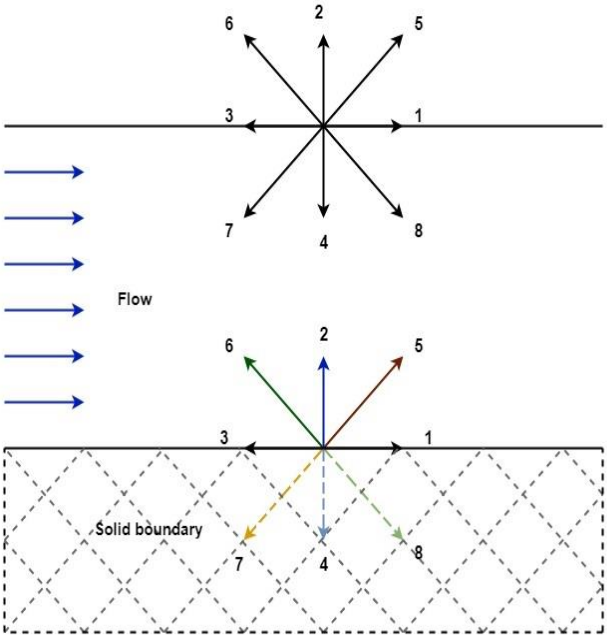

Figure 2.4: Simple bounce-back scheme.

2.6.3 Boundary condition with known velocity

In CFD simulations, some flow properties are typically known, for example, the velocity, pressure, and density at the boundary domain, such as the inlet velocity or the outlet pressure. Zou and He [25] introduced a method for calculating three unknown distribution functions at the boundary based on mass and momentum conservation equations at the appropriate location according to the conservation of mass:

$$\rho = f_0 + f_1 + f_2 + f_3 + f_4 + f_5 + f + f_7 + f_8 \tag{2.29}$$

The momentum equation in the x-direction would be

$$\rho u = f_1 + f_5 + f_8 - f_6 - f_3 - f_7 \tag{2.30}$$

and the momentum equation in the y-direction would be

$$\rho v = f_5 + f_2 + f_6 - f_7 - f_4 - f_8 \tag{2.31}$$

Solving the above equation requires knowing which equilibrium condition will be normal to the boundary:

$$f_n^{(+)} - f_n^{eq(+)} = f_n^{(-)} - f_n^{eq(-)} \tag{2.32}$$

where *n* denotes the condition normal to the boundary, (+) means in the positive direction, and (-) indicates in the negative direction. For more detailed explanations see page 75 chapter 5 [18]. Figure 2.5 illustrates the distribution functions at the boundaries of a domain.

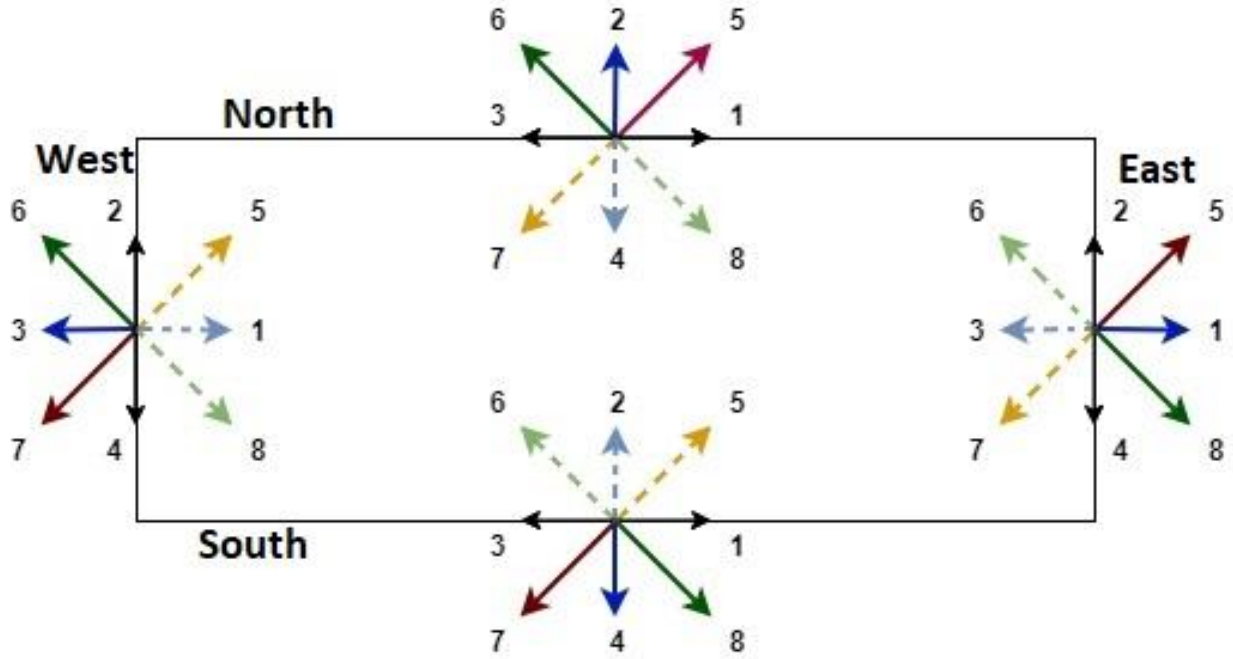

Figure 2.5: Distribution functions at the boundaries of a domain.

Chapter 3

Compressible Lattice Boltzmann Method

3.1 Introduction

With the conventional lattice Boltzmann method (LBM), the low-Mach-number limitation arises from the use of a truncated version (typically up to the second order) of the Maxwell equilibrium distribution function, as set out in Eq. (2.7). The goal is to facilitate the integration of the Boltzmann equation in a discrete velocity space using the Gauss-Hermite quadrature. However, the higher-order truncated terms in the Taylor series expansion of the Maxwell equilibrium distribution function $f^{eq}{}_i$ become significant when the Mach number increases.

The literature includes reports of several remedies developed for overcoming this limitation and finding a better equilibrium distribution function as a replacement for the truncated f_i^{eq} included in Eq. (2.7). The aim is to solve compressible flow problems at high Mach numbers using LBM. As can be seen in the equation, the higher-order terms can be neglected when the Mach number is small, and it can be applied directly to LBM models to solve incompressible flow problems. On the other hand, the truncated higher-order terms can become significant at high Mach numbers, resulting in numerical instability. LBM researchers have developed

models for high-Mach-number flows, in an attempt to overcome the limitation in two ways: (1) by solving the Maxwell equilibrium distribution function based on the inclusion of additional higher-order terms, or (2) by finding an alternative distribution function rather than using the Maxwell equilibrium distribution function to avoid the truncation errors.

Recently published studies have reported several successful developments with respect to compressible LBM. In 1997, Shouxin et al. [26] introduced a new model for the density distribution function, with three energy levels. Their 2D model involves 13 or 17 lattice velocities. In the same year, Shan and He [27] presented a new model for use with compressible LBM based on a third-order equilibrium distribution function in conjunction with the Gauss-Hermite quadrature to determine the weight coefficients ω_i in Eq. (2.7). In 1999, Guangwu et al. [28] used standard D2Q9 lattice models with new coefficients in their equilibrium distribution functions. In 2004, Kataoka and Tsutahara [1], [2] introduced two compressible LBM models to solve the Euler and Navier-Stokes equations. They found that the specific heat ratio cannot be chosen freely, so they developed a new distribution function to overcome this deficiency and solve compressible flow problems. In 2007, Qu et al. [29] proposed a new alternative method for constructing a circular equilibrium distribution function in order to use LBM to simulate an inviscid compressible flow at high Mach numbers. The circular function is a probability

distribution function on a unit circle, which is simple to integrate into the particle velocity space and, more importantly, applicable with respect to the Navier-Stokes equation.

3.2 Limitations of the LBM approach

As explained, LBM has wide applications for the simulation of a variety of incompressible flows. In contrast, the limitations with respect to simulating compressible flows become evident in the case of a high Mach number. The major source of this limitation is the equilibrium distribution functions used in LBM. The Chapman-Enskog expansion (Appendix A) provides a framework in which the hydrodynamics equations for a gas can be derived from the Boltzmann equation. This feature requires the equilibrium distribution functions to be in a polynomial form of particle velocity in order to recover the Navier-Stokes equations. The Maxwellian distribution function in the exponential form of particle velocity cannot be applied directly in the Boltzmann equation, so to discretize the equilibrium distribution function in the velocity space we have to use a polynomial form of the Maxwell Boltzmann distribution function, which can be expressed through the exponential weight function of Hermite polynomials, so then the moment integrals are in a form which lets us evaluate them exactly as a discrete sum over the polynomial integrand evaluated at specific points. The discrete equilibrium

distribution f_i^{eq} was therefore derived via an expansion of the continuous Maxwell-Boltzmann distribution f_i^{eq} in the truncated sum of Hermite polynomials in terms of the Mach number. The polynomial form of the distribution function inevitably limits the Mach number that can be applied in the equation, which must be less than 0.1 in order to reduce the error of simulation, which occurred because of the using a truncated form of the Maxwell Boltzmann distribution function. The Maxwell-Boltzmann distribution is a statistical probability distribution that is used for describing particle speeds in ideal gases, where the particles move freely inside a stationary container.

The equilibrium distribution can be written in terms of the macroscopic quantities of density ρ, fluid velocity u, and temperature T as

$$f^{eq}(\rho, \mathrm{u}, T, \vec{c}) = \frac{\rho}{(2\pi RT)^{\frac{d}{2}}} e^{-\frac{(\vec{c}-\mathrm{u})^2}{2RT}} \tag{3.1}$$

where d is the number of spatial dimensions and R is the gas constant.

The lattice Boltzmann method is based on kinetic theory of gases and operates on distribution functions in phase-space, thus requiring, in addition to a space and time discretization, a discretization of the velocity space as well.

The discretization of the lattice Boltzmann equation is expressed as

$$f_i(x + \vec{c}_i\delta t, t + \delta t) - f_i(x,t) = -\frac{1}{\tau}\left[f_i(x,t) - f_i^{eq}(x,t)\right] \qquad (3.2)$$

The general form of the equilibrium distribution function can be expressed as

$$f_i^{eq} = \Phi\omega_i[A + B\vec{c}_i.\,\mathrm{u} + C(\vec{c}_i.\,\mathrm{u})^2 + D\mathrm{u}^2] \qquad (3.3)$$

where u is the macroscopic velocity. A, B, C, and D are constants determined from the mass, momentum, and energy equations. The Φ scalar parameter is equal to the summation of all of the equilibrium distribution functions.

$$\Phi = \sum_{i=0}^{i=n} f_i^{eq} \qquad (3.4)$$

where n is the number of lattice sites. At a stagnation point, the fluid velocity is zero, and Eq. (3.3) can then be reduced to

$$f_i^{eq} = \Phi A\omega_i \qquad (3.5)$$

It turns out that A is equal to unity, where $\sum_{i=0}^{i=n}\omega_i = 1$. The weighting factor for LBM models see page 88 chapter 3 [12].

Expanding Eq. (3.1) in a Taylor series and integrating the truncated version of Eq. (3.3) in the particle velocity space using the Gauss-Hermite quadrature enables the following f_i^{eq} to be obtained in terms of Mach numbers as

$$f_i^{eq}(x,t) = \omega_i \rho \left(1 + \frac{3\vec{c}_i \,.\, \mathrm{u}}{c_s^2} + \frac{9(\vec{c}_i \,.\, \mathrm{u})^2}{2c_s^4} - \frac{3\mathrm{u}^2}{2c_s^2} \right) + O(\mathrm{u}^3) \quad (3.6)$$

where

for D3Q15 and D3Q19 models $c_s = \frac{1}{\sqrt{3}}$ in the lattice units $\Delta x = \Delta y = \Delta t = 1$ [23], and $\mathrm{u} = ui + uj$

As can be seen in Eq. (3.6), the higher-order terms can be neglected when the Mach number is small, and it can be applied directly to solve incompressible flows. Other the other hand, the truncated higher-order terms can become significant at high Mach numbers, resulting in numerical instability. LBM researchers have developed models for high-Mach-number flows, in an attempt to overcome the limitation in two ways: (1) by solving the Maxwell equilibrium distribution function based on the inclusion of additional higher-order terms, and (2) by finding a suitable alternative distribution function for compressible LBM.

3.3 Higher-order equilibrium distribution function

To solve incompressible flows in conventional LBM, the Maxwell-Boltzmann equilibrium distribution function is usually used for solving the Boltzmann equation, which is often expanded as a Taylor series in macroscopic velocity to the second order. In 1998, Shan and He [30] used a third-order expansion of the equilibrium distribution function together with the BGK collision term. They also proved that the discretization of the Boltzmann equation with a BGK collision term into values

at the nodes (or abscissas) of a quadrature formula is equivalent to the truncation of the third-order terms in the Hermite spectral space. To alleviate the compressibility limitations in conventional LBM, the sixth-order Hermite polynomials of the Maxwell equilibrium distribution function, as set out in Eq. (3.7), were adopted for solving the LBE with the D3Q19 lattice model, as depicted in Figure 3.1.

$$
\begin{aligned}
f_i^{eq}(x,t) = \ \omega_i \rho \Bigg\{ & 1 + \ c_{i\alpha}.u_\alpha + \frac{1}{2}\ [(c_{i\alpha}.u_\alpha)^2 - u_\alpha^2] + \frac{(T-1)}{2}\left(c_{i\alpha}^2 - D\right) \\
& + \frac{c_{i\alpha}.u_\alpha}{6}[(c_{i\alpha}.u_\alpha)^2 - 3u_\alpha^2] + \frac{T-1}{2}(c_{i\alpha}.u_\alpha)\left(c_{i\alpha}^2 - D - 2\right) \\
& + \frac{1}{24}[(c_{i\alpha}.u_\alpha)^4 - 6(c_{i\alpha}.u_\alpha)^2 u_\alpha^2 + 3u_\alpha^2] \\
& + \frac{T-1}{4}\left[\left(c_{i\alpha}^2 - D - 2\right)((c_{i\alpha}.u_\alpha)^2 - u_\alpha^2) - 2(c_{i\alpha}.u_\alpha)^2\right] \\
& + \frac{(T-1)^2}{8}[c_{i\alpha}^4 - 2(D+2)c_{i\alpha}^2 + D(D+2)] \\
& + \frac{u_\alpha}{120}[(c_{i\alpha}u)^4 - 10(c_{i\alpha}.u_\alpha)^2 u_\alpha^2 + 15u_\alpha^5] \\
& + \frac{T-1}{12}u_\alpha\left[\left(c_{i\alpha}^2 - D - 4\right)(c_{i\alpha}.u_\alpha)^2 - u_\alpha^2\right) - 2(c_{i\alpha}.u_\alpha)^2] \\
& + \frac{(T-1)^2}{8}u_\alpha[c_{i\alpha}^4 - 2(D+2)c_{i\alpha}^2 + (D+2)(D+4)]\Bigg\}
\end{aligned}
\tag{3.7}
$$

where α denotes the spatial directions in Cartesian coordinates, D is the spatial dimension, T is the temperature, u is fluid velocity, and ρ is the fluid density.

The macroscopic variables are

$$\rho = \sum_i f_i \tag{3.8}$$

$$\rho u = \sum_i f_i \, c_i \tag{3.9}$$

$$\rho \epsilon = \frac{1}{2} \sum_i f_i |c - u|^2 \tag{3.10}$$

The discrete velocities are

$$(c_{i1}, c_{i2}, c_{i3}) = \begin{cases} (0;\ 0;\ 0) & i = 0 \\ (\pm 1;\ 0;\ 0);\ (0; \pm 1;\ 0);\ (0;\ 0\ \pm\ 1) & i = 0, \dots, 6 \\ (\pm 1; \pm 1;\ 0);\ (\pm 1;\ 0; \pm 1);\ (0; \pm 1; \pm 1) & i = 7, \dots, 18 \end{cases} \tag{3.11}$$

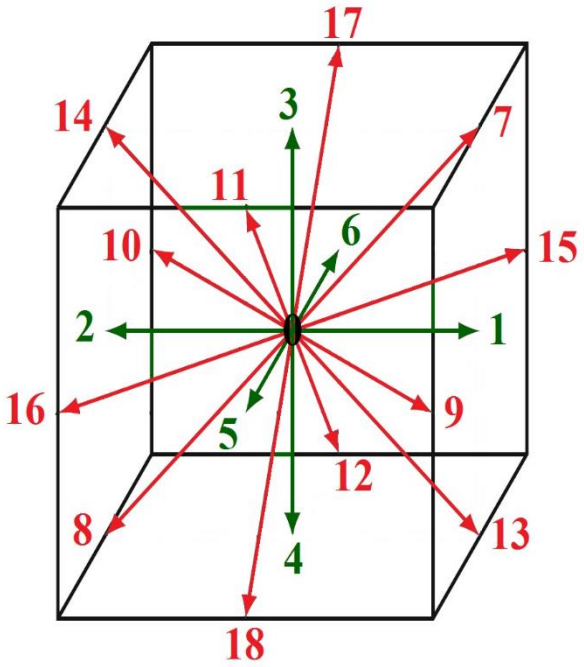

Figure 3.1: D3Q19 lattice model.

3.5 Kataoka and Tsutahara models

In 2004, Kataoka and Tsutahara (KT) [1], [2] developed two models for solving compressible flows using the LBE. The first model was created for solving the compressible Navier-Stokes equation with a flexible specific heat ratio, and the second model was devised for solving the compressible Euler equation. Because the two models are equivalent for subjoining the internal degrees of freedom to achieve the goal of adjusting the specific heat ratio, a new variable η is introduced for controlling the specific heat ratio at each point in the lattice structure. Both models are dependent on the specific heat ratio, which cannot be chosen freely. As well, the single relaxation time (SRT) is a given function of the density and the temperature. The goal is to apply a compressible LBM in a large-eddy simulation (LES) of a turbulent jet at high subsonic speeds in three dimensions. In this research, the KT LBM model was therefore implemented using the 3D D3Q15 lattice arrangement shown in Figure 3.2 for solving the compressible Navier-Stokes equation. Employing an LES subgrid scale (SGS) model enables the effects of turbulence to be taken into account.

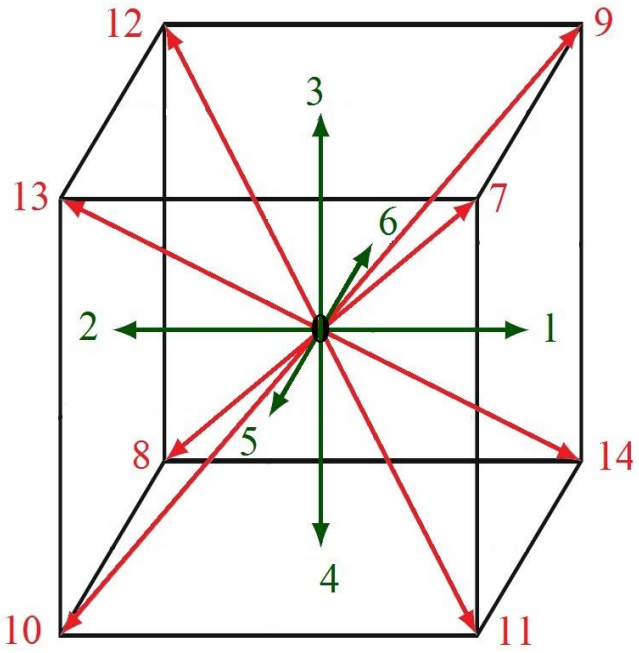

Figure 3.2: D3Q15 lattice model.

The macroscopic variables in the KT model are

$$\rho = \sum_{i=1}^{15} f_i \tag{3.12}$$

$$\rho u_\alpha = \sum_{i=1}^{15} f_i \, c_{i\alpha} \tag{3.13}$$

$$P\delta_{\alpha\beta} + \rho u_\alpha u_\beta = \sum_{i=1}^{15} f_i \, c_{i\alpha} c_{i\beta} \tag{3.14}$$

$$\rho(bRT + u_\alpha^2) = \sum_{i=1}^{15} f_i\left(c_{i\alpha}^2 + \eta_i^2\right) \tag{3.15}$$

where b is a given constant related to the specific heat ratio, expressed as

$$b = \frac{2}{\gamma - 1}. \tag{3.16}$$

and

$$\eta_i = \begin{cases} \eta_0 & i = 1 \\ 0 & i = 2, \ \ldots, 15 \end{cases} \tag{3.17}$$

The 15 lattice velocities are as follows:

$$(c_{i1}, c_{i2}, c_{i3}) \begin{cases} (0,0,0) & i = 1 \\ v_1(\pm 1,0,0), v_1(0,\pm 1,0), v_1(0,0,\pm 1) & i = 2, \ \ldots, 7 \\ \frac{v_2}{\sqrt{3}}(\pm 1, \pm 1, \pm 1) & i = 8, \ \ldots, 15 \end{cases} \tag{3.18}$$

The equilibrium distribution function is

$$f_i^{eq} = \rho\left(A_i + B_i u_\alpha c_{i\alpha} + D_i u_\alpha c_{i\alpha} u_\beta c_{i\alpha}\right) \quad i = 1, \ldots, 15 \tag{3.19}$$

where A_i, B_i, and D_i are given as

$$A_i = \begin{cases} \dfrac{b-3}{\eta_0^2}T & i = 1 \\ \dfrac{1}{6(v_1^2 - v_2^2)}\left[-v_2^2 + \left((b-3)\dfrac{v_2^2}{\eta_0^2} + 3 \right) T + \dfrac{v_2^2}{v_1^2}u_\alpha^2 \right] & i = 2,\ldots,7 \\ \dfrac{1}{8(v_2^2 - v_1^2)}\left[-v_1^2 + \left((b-3)\dfrac{v_1^2}{\eta_0^2} + 3 \right) T + \dfrac{3v_1^2 - v_2^2}{2v_2^2}u_\alpha^2 \right] & i = 2,\ldots,7 \end{cases} \quad (3.20)$$

$$B_i = \begin{cases} 0 & i = 1 \\ \dfrac{-v_2^2 + (b+2)T + u_\beta^2}{2v_1^2(v_1^2 - v_2^2)} & i = 2,\ldots,7 \\ \dfrac{3[-v_1^2 + (b+2)T + u_\beta^2}{8v_2^2(v_2^2 - v_1^2)} & i = 8,\ldots,15 \end{cases} \quad (3.21)$$

$$D_i = \begin{cases} 0 & i = 1 \\ \dfrac{1}{2v_1^4} & i = 2,\ldots,7 \\ \dfrac{9}{16v_2^4} & i = 8,\ldots,15 \end{cases} \quad (3.22)$$

The parameters included in Eqs. (3.14) to (3.22) were chosen to be $v_1 = 1$, $v_2 = 3$, and $\eta_0 = 2$.

Chapter 4

Large-Eddy Simulation Using the Lattice Boltzmann Method

4.1 Introduction

The direct numerical simulation (DNS) of fluid is based on the solving of the governing equations such as the Navier–Stokes equations, the Euler equation, or the lattice Boltzmann equation (LBE) without the imposition of any additional physical assumptions or the incorporation of subgrid scale models. In DNS, all scales of the fluid motion are resolved explicitly in the simulation. As a consequence, the mesh grid and the time step must be chosen to be fine enough to capture the dynamics of the flow from the largest (integral) to the smallest (viscous) scales. Needless to say, DNS is prohibitively computationally expensive to conduct for high-Reynolds-number flows over a large simulation domain. Owing to this fact, an alternative is provided by large-eddy simulation (LES) [31], which is intermediate in incurred computational cost between DNS and turbulence closure schemes that are representative of Reynolds-averaged Navier-Stokes (RANS) approaches. The basic idea behind LES is to ignore the solving of the smallest-length scales by means of a filtering model for the governing equation, which reduces the computational cost.

4.2 Subgrid scale modelling of turbulent flows using the lattice-Boltzmann method

LBM has recently gained in popularity because of its simplicity, ability to handle complex geometries (as with the immersed boundary method widely used in the CFD community), and the fact that it can be executed efficiently on graphics processing units (GPUs) in parallel processing systems [32]. The concept behind LES models is to include the physical effects that unresolved motion has on the resolved fluid motion [13]. For modelling the unresolved scales of motion at high Reynolds numbers, subgrid-scale (SGS) models such as the Smagorinsky model [31] are typically employed. In LES, the SGS models are applied following the performance of a spatial filtering operation on the Navier-Stokes equations [33], which is used to model the residual (fictitious) stresses arising from the application of a spatial filtering operation on the Navier-Stokes equation. In the case of the Smagorinsky SGS model, the anisotropic part of the Reynolds stress term is modelled as follows:

$$\tau_{\alpha\beta} - \frac{\delta_{\alpha\beta}}{3}\tau_{kk} = -2v_t\bar{S}_{\alpha\beta} = -2C^2\Delta^2|\bar{S}|\bar{S}_{\alpha\beta} \tag{4.1}$$

where δ_{ij} is the Kronecker delta function, C is the Smagorinsky constant, Δ is the filter width, and $|\bar{S}|$ is the magnitude of the large-scale strain rate tensor:

$$|\bar{S}| = \sqrt{2\bar{S}_{\alpha\beta}\,\bar{S}_{\alpha\beta}} \tag{4.2}$$

$$\bar{S}_{\alpha\beta} = \frac{1}{2}\left(\frac{\partial \bar{u}_\alpha}{\partial x_\beta} + \frac{\partial \bar{u}_\beta}{\partial x_\alpha}\right). \tag{4.3}$$

Furthermore, v_t is the eddy viscosity of the residual fluid motion which is modeled as $v_t = 2C^2\Delta^2|\bar{S}|$.

Employing LBM-LES to solve compressible turbulent flows using the higher-order equilibrium distribution function and the Kataoka and Tsutahara (KT) model described in sections 3.5 and 3.2 requires that the (effective) relaxation time τ be adjusted locally. The basic goal of applying LES in the LBM framework is to define a space-filtered particle distribution, which is dependent on the relaxation process. This concept is equivalent to Prandtl's mixing-length hypothesis, which suggests that a particle-free path is affected by the local strain intensity [34]. For this reason, the turbulent relaxation time τ_t is introduced into the effective relaxation time τ_w in order to take into account the effects of small-scale fluid motion.

The application of the SGS models in the LBM framework is accomplished through the introduction of a filtered particle distribution $\bar{f}$, defined as

$$\bar{f}_i(x + c_i\delta t, t + \delta t) - \bar{f}_i(x,t) = \frac{1}{\tau_w}\left[\bar{f}_i(x,t) - \bar{f}_i^{eq}(x,t)\right] \tag{4.4}$$

where τ_w is the effective relaxation time and can be written as

$$\tau_w = \tau_0 + \tau_t \tag{4.5}$$

The total viscosity can then be given as

$$v_w = v_0 + v_t \tag{4.6}$$

where v_0 is the laminar viscosity and v_t is the turbulent viscosity:

$$v_0 = \left(\tau_0 - \frac{1}{2}\right) c_s^2 \delta t \tag{4.7}$$

$$v_t = \tau_t c_s^2 \delta t \tag{4.8}$$

In LBM, $v_0 = \frac{(2\tau_0 - 1)}{6}$, and $v_t$can be calculated using the following Smagorinsky model:

$$v_t = C^2 \Delta^2 |S| \tag{4.9}$$

The effective lattice relaxation time τ_w is related to the total viscosity v_w according to the following relation:

$$\tau_w = \frac{1}{2} + \frac{v_w}{c_s^2 \delta t} = \frac{1}{2} + \frac{1}{c_s^2 \delta t}(v_t + v_0) = \frac{1}{2} + \frac{1}{c_s^2 \delta t}(v_0 + C^2 \Delta^2 |\bar{S}|) \tag{4.10}$$

Substituting Eq. (4.7) into Eq. (4.11) enables τ_w to be obtained as a function of laminar relaxation time τ_0, as follows:

$$\tau_w = \tau_0 + \frac{C^2 \Delta^s}{c_s^2 \delta t} |\bar{S}| \tag{4.11}$$

To proceed further, the resolved strain-rate tensor $\bar{S}_{\alpha\beta}$ and the non-equilibrium stress tensor Q_{ij} can be obtained as

$$\bar{S}_{\alpha\beta} = \frac{1}{2\rho_0 c_s^2 \tau_w} \bar{Q}_{ij} \tag{4.12}$$

The non-equilibrium stress tensor can be calculated locally as follows:

$$\bar{Q}_{\alpha\beta} = \sum_i \vec{c}_{(i,\alpha)}\, c_{i,\beta} \left[\bar{f}_i - \bar{f}_i^{eq}\right] \tag{4.13}$$

The magnitude of the non-equilibrium stress tensor $|\bar{Q}|$ defined in terms of $Q_{\alpha\beta}$ analogously to how the magnitude of the resolved strain-rate tensor $|\bar{S}|$ is defined in terms of $S_{\alpha\beta}$) is related to $|\bar{S}|$

$$|\bar{S}| = \frac{|\bar{Q}|}{2\rho_0 c_s^2 \tau_w} \tag{4.14}$$

Substituting Eq. (4.14) in Eq. (4.10) results in quadratic equation for the determination of τ_w given by

$$\tau_w^2 - \tau_0 \tau_w - \frac{C^2 \Delta^2}{2\rho_0 c_s^4 \delta t} |\bar{Q}| = 0 \tag{4.15}$$

When the above equation is solved analytically for τ_w, and after some simplifications, the total relaxation time can be expressed as

$$\tau_w = \frac{1}{2}\left(\sqrt{\tau_0^2 + \frac{2C^2\Delta^2}{\rho_0\, c_s^4\, \delta t}|\bar{Q}|} - \tau_0\right) \tag{4.16}$$

Using a uniform mesh grid, $\vec{c}_{(i,\alpha)} = \frac{\delta x}{\delta t} = 1$, this leads to $c_s^2 = \frac{1}{3}$ [23]

The effective relaxation time τ_w of Eq. (4.16) is used to define the BGK collision term in the LBE for the filtered discrete particle distribution function Eq. (4.4).

4.3 Subgrid scale modelling for LBM-MRT

This section explains the implementation of the LBE for LES in the context of the D3Q19 LBM-MRT model in conjunction with the Smagorinsky subgrid model. In 2006, Yu and others [35] were implementing an LES model for a multiple relaxation time (MRT) model of the D3Q19 model of a turbulent square jet. In the course of their research, they derived a transformation matrix M for LES, as shown below.

The LBM with an MRT collision operator can be expressed as

$$f(x_i + c_i\Delta t, t + \Delta t) - f(x_i+, t) = \Omega(x_i+, t)$$
$$= -M^{-1}.S.[m - m^{eq}] \tag{4.17}$$

The mapping between the velocity and moment spaces can be performed using a linear transformation:

$$m = M.f\ , f = M^{-1}.m \tag{4.18}$$

where M is a matrix:

$$f(x_i + \vec{c}_i\delta t, t_n + \delta t) = \left(f_0(x_i, t + \delta t), \dots, f_Q\left(x_i + c_Q\delta t, t_n + \delta t\right)\right)^T \tag{4.19}$$

$$f(x_i, t_n) = \left(f_0(x_i, t_n), f_1(x_i, t_n) \dots, f_Q(x_i, t_n)\right)^T \tag{4.20}$$

$$m(x_i, t_n) = \left(m_0(x_i, t_n), m_1(x_i, t_n) \dots, m_Q(x_i, t_n)\right)^T \tag{4.21}$$

$$m^{eq} = \left(m_0^{eq}(x_i, t_n), m_1^{eq}(x_i, t_n) \dots, m_Q^{eq}(x_i, t_n)\right)^T \tag{4.22}$$

where T is the transpose operator.

For the D3Q19 model, the moments are arranged in the following order [35]:

$$m_0 = \delta\rho,\ m_1 = \vec{c},\ m_2 = \varepsilon,\ \ m_{3,5,7} = j_{x,y,z,}\ \ m_{4,6,8} = q_{x,y,z} \tag{4.23}$$

The equilibria of the moments m^{eq} are [35]:

$$m_1^{eq} = -11\delta\rho + \frac{19}{\rho_0}\mathrm{j.j}, \quad m_2^{eq} = \omega_\varepsilon\delta\rho + \frac{\omega_{\varepsilon i}}{\rho_0}\mathrm{j.j}$$

$$m_{4,6,8}^{eq} = -\frac{2}{3}j_{x,y,z}$$

$$m_9^{eq} = \frac{1}{\rho_0}(3j_x^2 - j.j), \qquad m_{11}^{eq} = \frac{1}{\rho_0}\left(j_y^2 - j_z^2\right), \tag{4.24}$$

$$m_{10}^{eq} = \omega_{xx}m_9^{eq}, \qquad m_{12}^{eq} = \omega_{xx}m_{11}^{eq},$$

$$m_{13}^{eq} = \frac{1}{\rho_0}j_xj_y, \qquad m_{14}^{eq} = \frac{1}{\rho_0}j_yj_z, m_{15}^{eq} = \frac{1}{\rho_0}j_zj_x$$

$$m_{16}^{eq} = m_{17}^{eq} = m_{18}^{eq} = 0$$

The parameters of the equilibria are chosen as follows in order to optimize the linear stability of the model:

$$\omega_\varepsilon = \omega_{xx} = 0 \text{ and } \omega_{\varepsilon j} = -475/63$$

In LBM, the speed of sound $c_s = \vec{c}_i/\sqrt{3}$, where $\delta_x = \delta_t = 1$, so the viscosity is

$$\nu = \frac{1}{3}\left(\frac{1}{s_\nu} - \frac{1}{2}\right)c^2\delta_t, \quad \vec{c}_i = \frac{\delta_x}{\delta_t} = 1 \tag{4.25}$$

For LES, the total viscosity $= v_0 + v_t$, where v_0 is the molecular viscosity and v_t is the turbulent viscosity (eddy viscosity), with $v_t = (C_s\Delta_x)^2\bar{S}$, where C is the Smagorinsky constant, Δ is the filter width, and $\bar{S}$ is the magnitude of the large-scale strain rate tensor.

If the above new paramours are used in the relaxation matrix, LBM can then simulate high Reynolds number flows. The MRT-LES model enhances numerical stability, accuracy, and the achievable Reynolds number.

Chapter 5

Sound Propagation

5.1 Introduction

Over the last few decades, airplane travel has become increasingly popular due to its speed, affordability, and safety. Today's new planes are quieter than older models because designers need to satisfy standards and regulations related to the reduction of noise emissions, but airport community noise continues to be an important environmental issue. Jet noise is one of the primary sources of noise produced by aircraft. It is of particular concern for people living near airports because the number of flights is increasing every day [36]. A greater understanding of jet noise and sound propagation will help researchers reduce noise pollution from aircraft.

Computational aeroacoustics (CAA) is a branch of acoustics science that studies the sound generated by turbulent flow or the aerodynamic force interacting with a surface that generates sound around it. Currently, no complete theory has been developed for use in studying the noise generated by fluid flows, so most aeroacoustics theories rely on acoustic analogies. With this approach, aerodynamic flow equations are written as wave equations. Most flow noise problems require a hybrid solution involving two steps: first, the flow-governing equations for the near-

field must be solved numerically, and second, a wave equation must be applied using the near-field flow properties in order to predict the far-field noise. Solving this kind of problem requires high-performance computing machines [37].

Table 5.1 lists common sources of sound, together with their pressure and decibel levels.

Table 5.1: Typical Sound Pressure Levels (SPL) [38]

Sources at 1 m	Sound Pressure (p)	SPL
Rifle	200 Pa	140 dB
Threshold of pain	20 Pa	120 dB
2 Power Mowers	2 Pa	100 dB
1 Power Mowers	1 Pa	94 dB
Street traffic	0.2 Pa	80 dB
Talking	0.02 Pa	60 dB
Library	0.002 Pa	40 dB
TV Studio	0.0002 Pa	20 dB
Threshold of hearing	0.00002 Pa	0 dB

5.2 Lighthill's acoustic analogy

The derivation of aeroacoustics theory is dependent on the mass conservation equation and momentum equations for compressible flow as a basis for deriving a non-homogeneous wave equation that governs sound propagation in the far-field region. One of the earliest and most popular aeroacoustics theories was developed

in the early 1950s by Sir James Lighthill [39] [40]. Lighthill demonstrated how the problem of aerodynamic sound can be posed as an acoustic analogy for a turbulent jet in cases in which the noise source is surrounded by a quiescent fluid. This approach can be used for determining the equations that describe the generation of sound waves that propagate the sound to the far-field region.

Lighthill's formulation can be applied for calculating acoustic radiation from turbulent flow embedded in a homogeneous fluid. To derive the acoustic inhomogeneous wave equation, Lighthill begins with the summation of the equations for governing continuity and the momentum, which can be written as [37]

$$\frac{\partial \rho}{\partial t} + \frac{\partial \rho u_j}{\partial x_j} = 0 \tag{5.1}$$

$$\rho \frac{\partial u_i}{\partial t} + u_j \frac{\partial \rho u_i}{\partial x_j} = -\frac{\partial p}{\partial x_i} - \frac{\partial \tau_{ij}}{\partial x_j} \tag{5.2}$$

where ρ denotes fluid density, u is the velocity vector, p expresses the overall pressure, and τ_{ij} is a component of the viscous stress tensor, which can be expressed in terms of the velocity gradients as

$$\tau_{ij} = -\mu \left(\frac{\partial u_i}{\partial x_j} + \frac{\partial u_j}{\partial x_i} - \frac{2}{3} \mu \delta_{ij} \frac{\partial u_k}{\partial x_k} \right) \tag{5.3}$$

where μ is the fluid viscosity and δ_{ij} is the Kronecker delta.

If Eq. (5.1) is next multiplied by u_i and the resulting equation is then added to Eq. (5.2), the result is Eq. (5.4):

$$\frac{\partial \rho u_i}{\partial t} = \frac{\partial}{\partial x_j}\left(\rho u_i u_j + \delta_{ij} p + \tau_{ij}\right) \tag{5.4}$$

Subtracting $c_0^2 \partial x_j^2 / \partial x_j^2$ from each sides of Eq. (5.4) and combining the terms yields

$$\frac{\partial^2 \rho}{\partial t} - c_0^2 \frac{\partial^2 \rho}{\partial x_i^2} = -\frac{\partial^2 T_{ij}}{\partial x_i \partial x_j} \tag{5.5}$$

where c_∞ is the speed of sound and T_{ij} is Lighthill's stress tensor, given as

$$T_{ij} = \rho u_i u_j + \delta_{ij}[(p - p_0) - c_0^2(\rho - \rho_0)] - \tau_{ij} \tag{5.6}$$

where ρ_0 is density and p_0 is the pressure of the atmosphere.

$$\frac{\partial^2 \rho'}{\partial t^2} = -c_0^2 \frac{\partial^2 \rho'}{\partial x_i^2} = \frac{\partial^2 T_{ij}}{\partial x_i \partial x_j} \tag{5.7}$$

where $\rho' = \rho - \rho_0$ and $p' = p - p_0$

With the use of some approximations, Lighthill's tensor T_{ij} can be expressed as

$$T_{ij} \approx \rho u_i u_j \tag{5.8}$$

Eq. (5.7) is known as Lighthill's non-homogeneous acoustic wave equation because it treats the turbulent flow as if it contained sound waves propagating in the same manner as in the rest of the surrounding fluid. The left side of the equation (5.7) specifies the propagation of the sound in a uniform medium with sound speed c_0

using density as the dependent variable. The right side of the equation is known as the source term, which contains all of the effects that generate acoustic sound waves [41].

5.3 Ffowcs Williams and Hawkings

The Ffowcs Williams and Hawkings (FW-H) equation is an integral method based on Lighthill's acoustic analogy. The FW-H equation comprises five formal expressions for propagating the sound created by turbulent flow in the presence of arbitrarily moving surfaces [42]. The main goal of using the FW-H analogy is to handle solid surface interactions that are directly involved in the generation of flow sound. Thus far, it is the most appropriate theoretical support for understanding the mechanisms involved in the generation of aerodynamic sound from bodies in a complex motion, such as helicopter rotors and wind turbine wings. The FW-H formulation has been adopted extensively in a broad research area that examines solid surfaces and permeable control surfaces close to a solid body, and it has been widely employed for solving aeroacoustics problems. This section presents the FW-H permeable formulation, which can be applied for predicting jet noise in the far-field. The permeable surface formulation can be used as a control surface in the same way as with the Kirchhoff method [43].

The integral form of the FW-H equation is

$$p'(\vec{x},t) = p'_T(\vec{x},t) + p'_L(\vec{x},t) + p'_Q(\vec{x},t) \tag{5.9}$$

where $p'(\vec{x},t)$ the sound pressure at the far field, $p'_T(\vec{x},t)$ is known as the thickness noise, $p'_L(\vec{x},t)$is the loading noise.

$$p'_T(\vec{x},t) = \frac{1}{4\pi}\int_s \left[\frac{\rho_0\left(\dot{U}_n + U_n\right)}{r(1-M_r)^2}\right]_{ret} dS + \int_s \left[\frac{\rho_0 U_n\left(r\dot{M}_r + c_0(M_r - M^2)\right)}{r^2(1-M_r)^3}\right]_{ret} dS \tag{5.10}$$

and

$$p'_L(\vec{x},t) = \frac{1}{4\pi c_0}\int_s \left[\frac{\dot{L}_r}{r(1-M_r)^2}\right]_{ret} dS + \int_s \left[\frac{L_r - L_M}{r^2(1-M_r)^2}\right]_{ret} dS + \frac{1}{c_0}\int_s \left[\frac{L_r\left(r\dot{M}_r + c_0(M_r - M^2)\right)}{r^2(1-M_r)^3}\right]_{ret} dS \tag{5.11}$$

$$p'_Q(\vec{x},t) = \frac{1}{4\pi}\int_V \left[\frac{1}{r}\frac{\partial^2\left(T_{ij}\delta\right)}{\partial y_i \partial y_j}\right] dV \tag{5.12}$$

More information about these FW-H's formula can be found in Brentner and Farassat paper [44]

Where

$$\dot{U}_n = v_i + \frac{\rho}{\rho_o}(u_i - v_i)$$

$$L_i = P_{ij} + \rho u_i(u_n - v_n)$$

T_{ij} pressure-stress tensor, Lighthill tensor

u_i fluid velocity component in the x_i direction

v_n fluid velocity component normal to the surface

u_n local normal velocity of source surface

r Distance between observer and source

M_r Mach number of sources

L = loading noise component

o = fluid variable in a quiescent medium

Q = quadrupole noise component

ret = quantity evaluated at retarded time

T = thickness noise component

5.4 Kirchhoff surface integration

The Kirchhoff integral theorem, which expresses a wave field in the surrounding region from a control surface of the field's value, is well known and widely used in acoustics problems. The method was developed as a means of

studying light diffraction and electromagnetic waves but was later modified for aeroacoustics applications such as fan noise, wind turbines, and jet noise.

In 1882, Kirchhoff developed an integral surface method using the Green's function identities to derive a solution to a homogeneous wave equation [45]. In 1930, Morgan extended Kirchhoff's formula to be applied to moving surfaces [46]. Then, in 1988, Farassat and Myers [47] provided a modern derivation of Morgan's formula, making Kirchhoff's integral surface a powerful technique in the CAA field.

In many aeroacoustics applications, however, some difficulties are associated with the use of Kirchhoff's surface method. The integral surface must be placed in a region where the flow is completely governed by a homogeneous linear wave equation with constant coefficients and must enclose all of the nonlinear flow effects and noise sources in a region where the linear wave equation is valid [48].

In Kirchhoff's method, it is assumed that the flow is governed by the following homogeneous linear equation:

$$\nabla^2\Phi - \frac{1}{c_\infty^2}\left(\frac{\partial}{\partial t} + u_\infty \frac{\partial}{\partial x}\right)^2 \Phi = 0 \qquad (5.13)$$

where Φ is the flow field variable (acoustic variable), c_∞ is the speed of sound at ambient conditions, and u_∞ is the uniform velocity of the control surface. Assuming that the stationary control surface $u_\infty = 0$, the preceding equation reduces to a simple wave equation:

$$\nabla^2\Phi - \frac{1}{c_\infty^2}\frac{\partial^2\Phi}{\partial t^2} = 0 \qquad (5.14)$$

The variable Φ and its first derivatives $\partial\Phi/\partial t$ and $\partial\Phi/\partial n$ should be continuous outside the control surface S where n is the normal direction.

Morino and others [49], [50] provided a solution to the convective wave equation using the Green function approach to derive a representation solution for the wave equation in terms of the surface pressure and its derivatives. As a solution for the equation, the Green function can be formulated as

$$\nabla^2 G - \frac{1}{c_\infty^2}\frac{\partial^2 G}{\partial t^2} = \delta(x - x', y - y', z - z', t - t') \qquad (5.15)$$

where δ is the Dirac function, (x', y', z') indicates the source location at retarded time t', and $(x, y, z,)$ represents the observer's location at observer or reception time t.

The Green function G must satisfy the causality condition for hyperbolic equations:

$$G = \frac{\partial G}{\partial t} = 0 \quad \text{for } t < t' \qquad (5.16)$$

For a subsonic flow, the solution for Eq. (5. 15) is given by

$$G = \frac{\delta(t' - t + \tau)}{4\pi r_0} \qquad (5.17)$$

where τ is the time delay between the sound source and the observer, given by $\tau = t - t' = \frac{r}{c_\infty}$, where r is the distance between the noise source and the detection.

If the small perturbation theory is applied to aerodynamics, a similarity exists in space and time for which, in subsonic flow, the distance between the noise source and the observer, in Prandtl-Glauert coordinates, is expressed as follows:

$$x_0 = x, \qquad y_0 = y\beta, \quad z_0 = z\beta \tag{5.18}$$

$$r_0 = \sqrt{(x - \acute{x})^2 + \beta^2[(y - \acute{y})^2 + (z - \acute{z})^2]} \tag{5.19}$$

$$\tau = \frac{[r_0 - M_\infty(x - \acute{x})]}{c_\infty \beta^2} \tag{5.20}$$

$$\beta = \sqrt{(1 - M_\infty^2)} \tag{5.21}$$

where the subscript o denotes the Prandtl-Glauert base value and M_∞ is the free-stream Mach number.

Lyrintzis and Mankbadi [51] presented the following solution for the simple wave detailed in Eq. (5.13):

$$\mathrm{M}_\infty G = -\frac{\delta}{\tau'} \tag{5.22}$$

where $\tau' = t - \tau$ is the retarded time.

Here, the potential function solution can be written as

$$4\pi\Phi(x,t) = \int_{S_0} \left[\frac{\Phi}{r_0^2}\frac{\partial r_0}{\partial n_0} - \frac{1}{r_0}\frac{\partial \Phi}{\partial n_0} + \frac{1}{c_\infty r_0 (1-M_\infty^2)}\frac{\partial \Phi}{\partial \tau}\frac{\partial r_0}{\partial n_0} - M_\infty \frac{\partial x_0}{\partial n_0} \right]_\tau dS_0 \tag{5.23}$$

where S_0 is Kirchhoff surface and n_0 is the outward normal to the Kirchhoff surface.

The pressure field can be expressed with the use of surface integrals [51], as in

$$p(x,y,z,t) = -\frac{1}{4\pi}\int \left[\frac{p}{r_0^2}\frac{\partial r_0}{\partial n_0} + \frac{1}{r_0}\frac{\partial p}{\partial n_0} + \frac{1}{c_\infty r_0 \beta^2}\frac{\partial p}{\partial t}\left(\frac{\partial r_0}{\partial n_0} - M_\infty \frac{\partial \acute{x}_0}{\partial n_0}\right) \right]_\tau dS_0 \tag{5.24}$$

An alternative approach to deriving the Kirchoff formula as a function of the frequency is a first Fourier analysis of the numerically calculated data, working then with the Kirchhoff formula in the frequency domain. In this case, the surface pressure is written as

$$p[(x,y,z),t] = \mathcal{R}\{\hat{p}[(x,y,z)]e^{-\omega t}\} \tag{5.25}$$

$$p(x,y,z,t) = \left(-\frac{\exp(-i\omega t)}{4\pi} \int_{S_0} \left[\frac{\hat{p}}{r_0^2} \frac{\partial r_0}{\partial n_0} + \frac{1}{r_0} \frac{\partial \hat{p}}{\partial n_0} \right.\right.$$

$$\left. + \frac{-i\omega}{c_\infty r_0 \beta^2} \hat{p} \left(\frac{\partial r_0}{\partial n_0} - M_\infty \frac{\partial \acute{x}_0}{\partial n_0} \right) \right] \qquad (5.26)$$

$$\left. \times exp\left\{ i \frac{\omega}{c_\infty \beta^2} [r_0 + M_\infty (x' - x)] \right\} dS_0 \right)$$

where (x', y', z') indicates the source location at retarded time t', and $(x, y, z,)$ represents the observer's location at observer or reception time t.

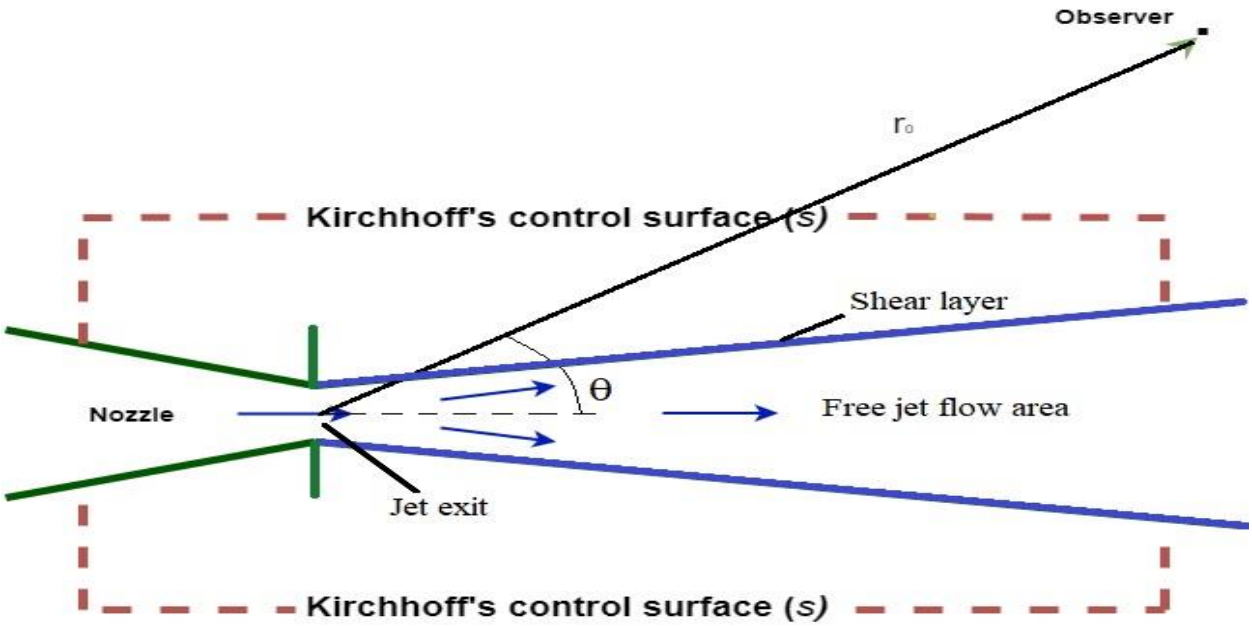

Figure 5.1: Kirchhoff's control surface.

Using the information described on the Kirchhoff surface, which is taken from the compressible LBM solution, enables acoustics information to be obtained at any

observer location in the region outside the Kirchhoff surface. Pan and others [52] proved that, in Kirchhoff's integral methods, the control surface shown in Figure 5.1 must be surrounding the entire source region for the noise generated from the turbulent flow to be predicted efficiently and accurately, and that more nonlinearities can be added outside the control surface. Their methodology showed that the predictions of the far-field jet sound pressure levels within the cone of silence agreed with the experimental data.

Chapter 6

Numerical Simulation of Turbulent Free Jets Using Lattice Boltzmann Method

6.1 Introduction

Computational fluid dynamics (CFD) features a variety of numerical methods, some of which are dependent on macroscopic model representatives. These models can be solved by finite-volume, finite-element or finite-difference methods based on a microscopic description. However, the lattice Boltzmann method (LBM) is considered to be a mesoscopic particle method lying between the macroscopic and microscopic scales. LBM is ideal for solving incompressible flow problems, but it is subject to some limitations with respect to solutions involving compressible flows, particularly at high Mach numbers. An improved lattice Boltzmann model for compressible flow problems is presented in this thesis. A higher-order Taylor series expansion of the Maxwell equilibrium distribution function has been used as a means of overcoming the LBM limitations associated with solving high-Mach-number flows. Large-eddy simulation (LES) is implemented in LBM for simulating turbulent jet flows. The results have been validated against available experimental data for turbulent compressible free jet flow at subsonic speeds.

As an alternative numerical method for modelling physical phenomena in fluid flows, LBM is a relatively new approach. It was originally developed from the lattice gas automata method (LGA) [53], which can be constructed as a simplified fictitious molecular dynamics model in which space, time, and particle velocities are all discrete [5]. LBM is known to be a powerful new tool for simulating a variety of incompressible flows. However, as mentioned above, it has also been found to have significant limitations with respect to solving high-Mach-number compressible flows. The major cause of these limitations is the contraction in the Maxwellian distribution function, which should be in the polynomial form of particle velocity [13]. The truncated equilibrium distribution function therefore inevitably limits the range of the applicable Mach number.

The literature contains numerous reports of recent successful models for using LBM to solve compressible flow problems. Shouxin et al. [26] introduced two lattice models, D2Q13 and D3Q17, which are dependent on three energy levels for their density distribution function. The difficulty of using these two models is that many of the parameters in the models were chosen based on physical concepts. Shan and He [11] devised a new model for compressible LBM using a third-order Maxwell-Boltzmann equilibrium distribution function to reduce the truncation error, demonstrating success in solving compressible flow problems with Mach numbers up to $M_\infty = 0.6$. Other researchers proposed the development of alternative

equilibrium distribution functions rather than higher-order Maxwell-Boltzmann equilibrium distribution functions.

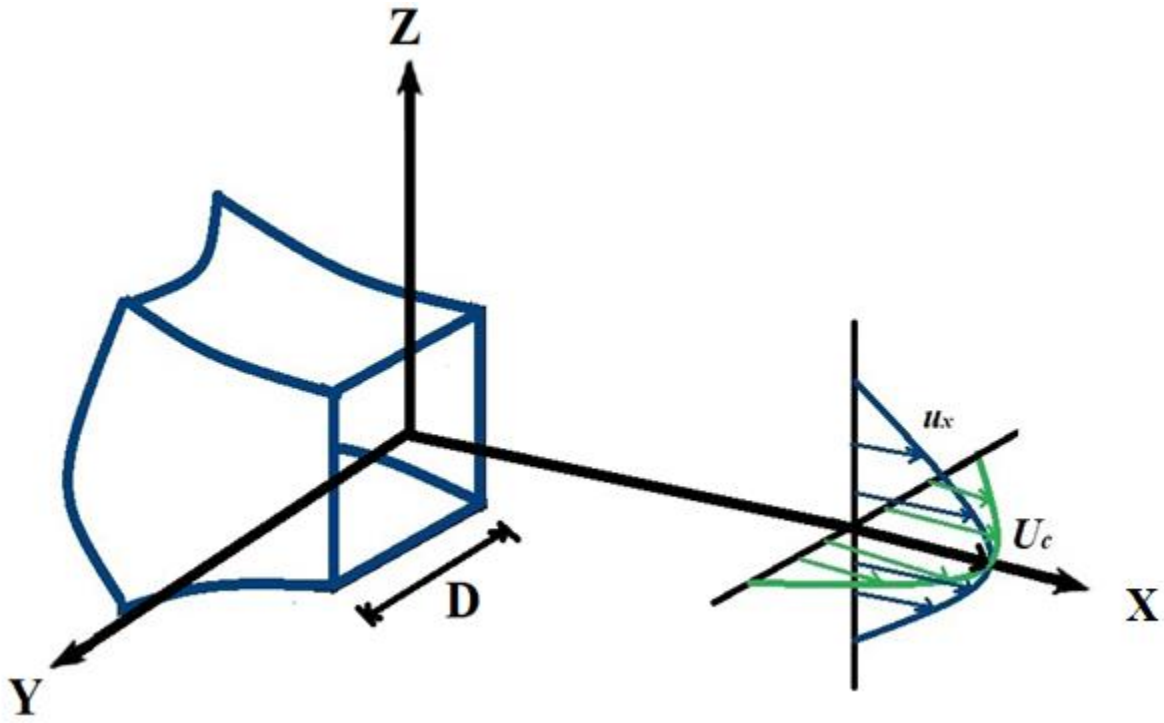

Figure 6.1: Schematic and reference system of a square jet nozzle.

Table 6.1 Free square jet characteristics

Test case characteristics	
Jet diameter	$D_j = 0.056\, m$
Jet exit velocity	$U_j = 100\, m/s$
Kinematic viscosity	$\nu = 1.516 * 10^{-5}\ m^2/s$
Reynolds number	$R_{eD} = \frac{U_j D_j}{\nu} = 3 * 10^5$
Mach number	$M_j = U_j/c = 0.3$
Simulation dimension (LBM) LBM grid sizing unit =1	Grid size (LBM units) $D_{lbm} = 10\ units$ $N_x = 20D_{lbm}\ , N_y = 5D_{lbm}, N_z = 5D_{lbm}$ Total number of grid points # 500000
Δx=0.0028, $\Delta y = 0.00112$, $\Delta z = 0.00112$,	LBM (Δx_{lbm}=Δy_{lbm}=Δz_{lbm} =1) $\Delta t_{lbm} = 1$
$CFL = \frac{u\Delta t}{\Delta x} = \frac{1}{\sqrt{3}}\ M_j$ =0.1732	time step $\Delta t = 0.485 * 10^{-5}$ sec
Total time steps	44000

6.2 Results and discussion

In this case study, characterized by a high Reynolds number and Mach number 0.3, the results were validated against experimental data for a square jet at different locations along the centerline of the jet $0 < x/D < 4$,where the streamwise velocity is almost constant. The Reynolds number plays an important role in jet development. The mean velocity along the centerline of the jet and the cross-section velocity

profile at different distances from the jet exit U_j were compared with experimental results. Figure 6.1 provides a schematic and reference system of the square jet nozzle, where U_c is the local centerline velocity and u_x is the instantaneous streamwise velocity at any (y, z) location.

The evolution of the mean velocity distributions and the streamwise turbulence intensity at $x/D = 0.5$, along with the experimental results from Ghasemi [54], are shown in Figure 6.2. The mean velocity of the jet and the turbulence intensity are normalized to the exit velocity of the jet at the centerline, which is the maximum mean velocity $U_{max}(x)$. The results indicated in Figure 6.2 (a) reveal no effect from the free shear layer, which means that the mean velocity is constant and equal to the exit velocity of the jet. Figure 6.2 (b) details the turbulence intensity distributions, which are dependent primarily on the Reynolds number [35].

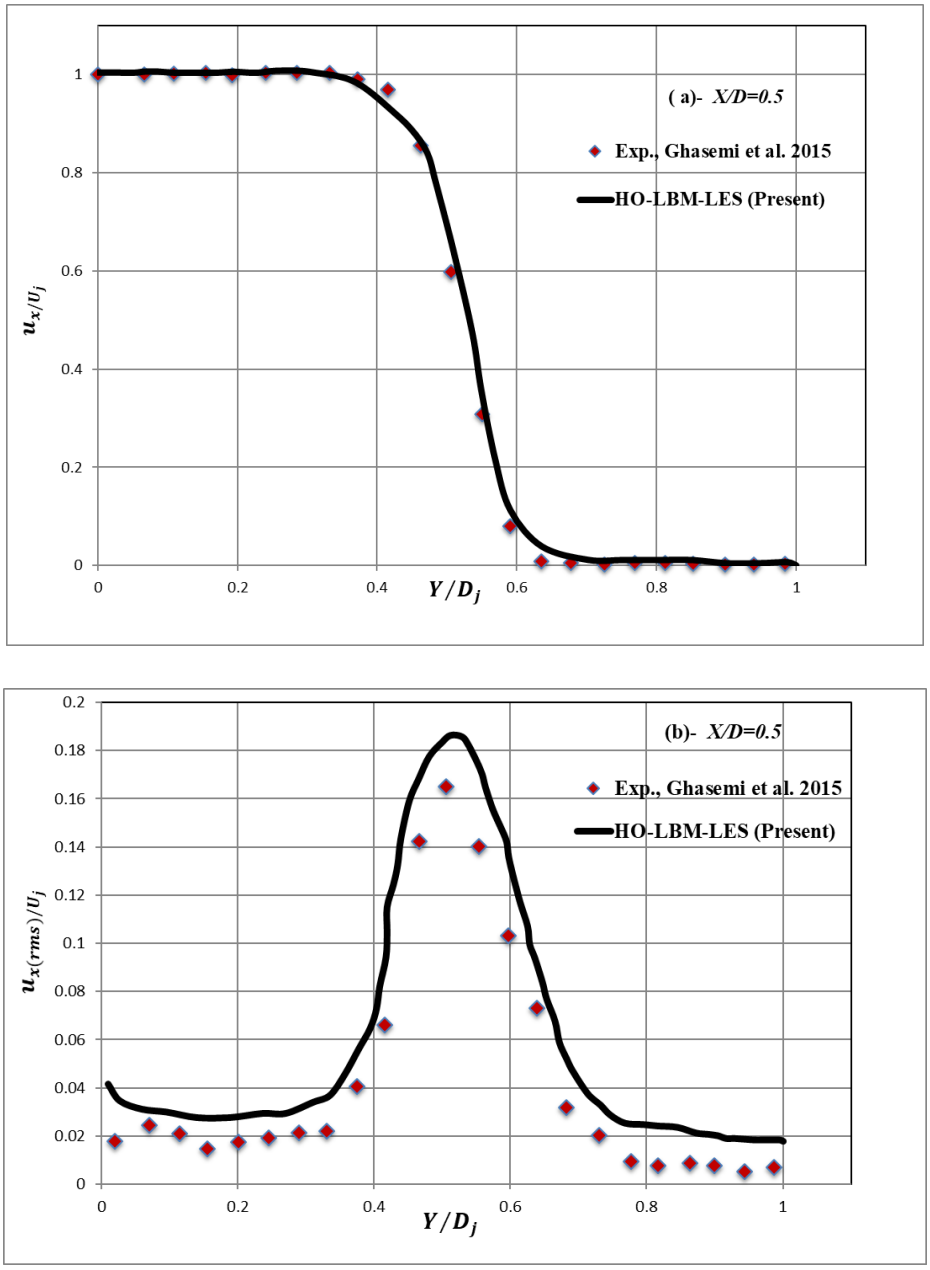

Figure 6.2: (a) Spanwise distribution of the mean streamwise velocity u_x/U_j; (b) streamwise turbulence intensity $u_{x(rms)}/U_j$.

These distributions appear to decrease with an increase in the Reynolds number. The turbulence intensity is confined to the centerline region of the jet, where no effects from the mixing shear layer are yet evident. The jet square exit shape and

the use of initial perturbation increase the turbulence intensity compared to Ghasemi's experimental results. Figure 6.3 provides the spanwise velocity profiles of the mean streamwise velocity at different locations along the axial direction of the jet ($x/D = 1$, 2, 3, 4, and 5) in the near-field region of the square jet. In Figure 6.3 (a) ($x/D = 1$), the flow is unaffected by the nearby free shear layer, and the velocity is almost constant between ($y/D = 0$) and ($y/D = 0.4$), which is equal to the exit velocity of the jet U_j. Figures 6.3 (b) and 6.3 (c) reveal that, a little farther from the jet exit ($x/D = 2$ and $x/D = 3$, respectively), the free shear layer has some effect on the core flow of the jet, and the velocity begins to resemble the Gaussian profile, but it still has a flat hat at ($y/D = 0 - 0.3$). As shown in Figures 6.3 (d) and 6.3 (e), toward the end of the near-field flow region at ($x/D = 4$ and $x/D = 5$, respectively), the flow is fully developed, and the velocity exhibits a top-hat distribution. In general, the mean streamwise velocity profiles u_x/U_j decrease along the jet *X*-axis and in the radial direction away from the jet centerline, where free shear layers and mixing layers create a turbulent flow region. At all locations along the streamwise direction, these figures indicate good agreement between the experimental and LBM-LES results.

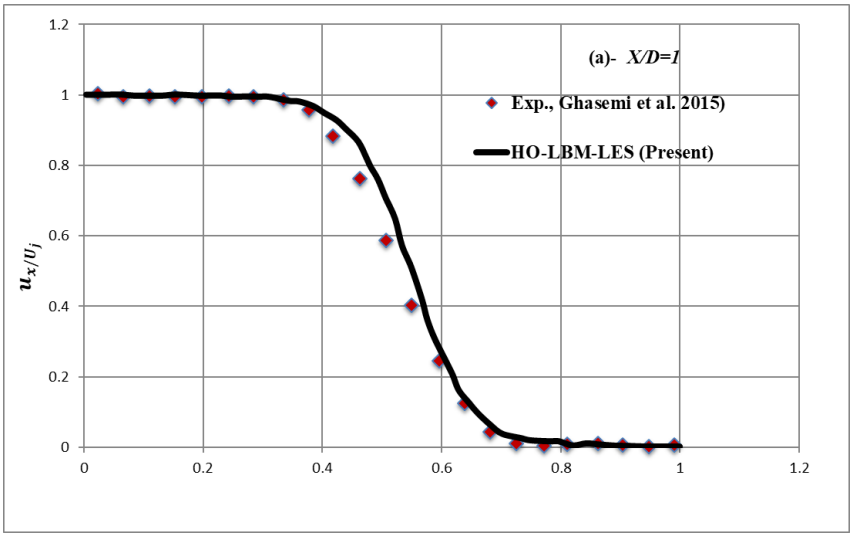
(a)- X/D=1
Exp., Ghasemi et al. 2015)
HO-LBM-LES (Present)
u_x/U_j
1.2
1
0.8
0.6
0.4
0.2
0
0
0.2
0.4
0.6
0.8
1
1.2

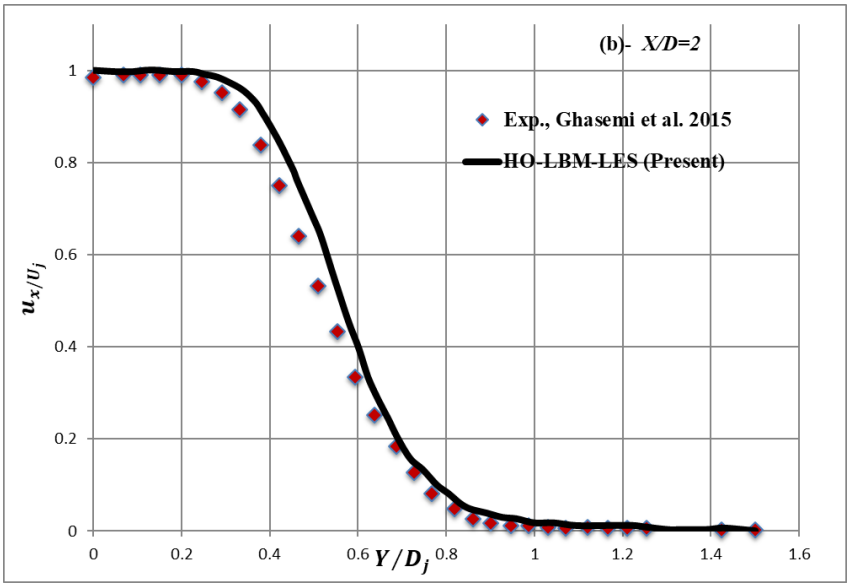
(b)- X/D=2
Exp., Ghasemi et al. 2015
HO-LBM-LES (Present)
u_x/U_j
Y/D_j
1
0.8
0.6
0.4
0.2
0
0
0.2
0.4
0.6
0.8
1
1.2
1.4
1.6

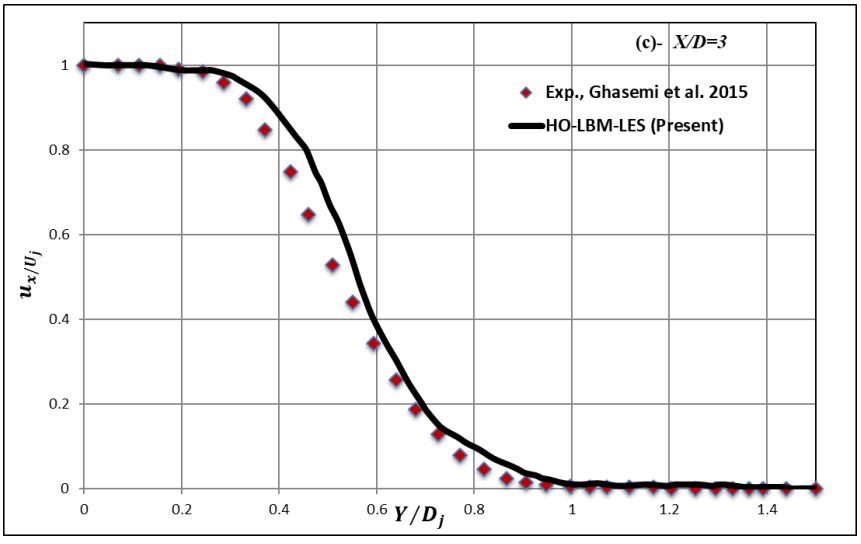
(c)- X/D=3
Exp., Ghasemi et al. 2015
HO-LBM-LES (Present)
u_x/U_j
Y/D_j
1
0.8
0.6
0.4
0.2
0
0
0.2
0.4
0.6
0.8
1
1.2
1.4

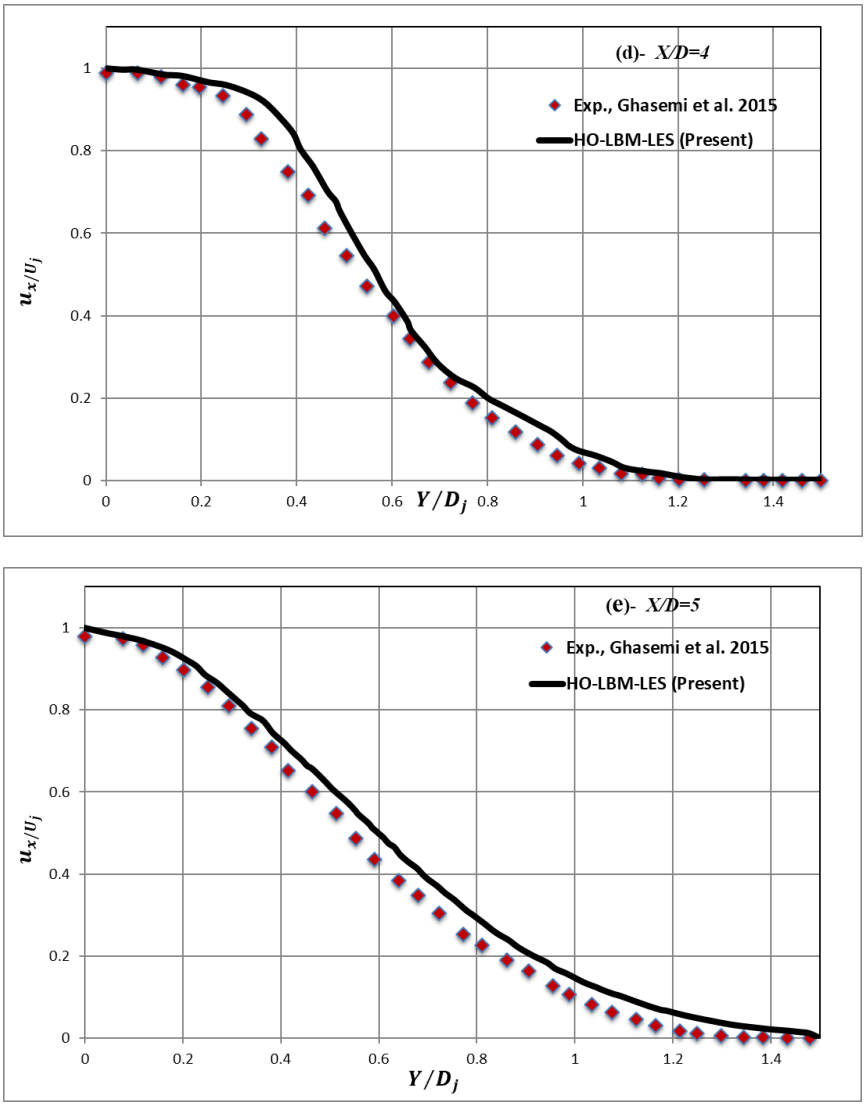

Figure 6.3: Mean streamwise velocity profiles of the square jet at different locations along the jet X-axis: (a) x/D = 1; (b) x/D= 2; (c) x/D= 3; (d) x/D= 4; (e) x/D = 5.

In conclusion, a new version of LBM has been developed for solving compressible turbulent flow with the use of a higher-order distribution function, and LBM has been combined with a LES subgrid scale (SGS) model in order to simulate a free jet at a subsonic flow regime. The essential idea behind the application of LES in LBM is to define a space-filtered particle distribution and to allow the dynamics

of the filtered particle distribution to feature a space-dependent relaxation. The LBM-LES results compare well with the experimental data in terms of the mean streamwise velocity, the turbulence intensity at different downstream locations, and the spreading rate of the jet. The use of LBM for compressible flows is still under development and has proven an exciting research area with many possible applications.

Chapter 7

Predicting Near-Field and Far-Field Jet Noise Using the Compressible Lattice Boltzmann Method

7.1. Introduction

Over the last few years, much of the attention given to LBM development has been directed at solving compressible turbulent flows [55]. Large-eddy simulation (LES), a powerful technique for simulate turbulent flow, has been successfully applied to a number of industrial problems because the LES computational time is significantly less than that required for direct numerical simulations (DNS). Thus far, LBM has been employed as a DNS method for solving relatively low Reynolds number flows [33]. However, LBM can be combined with LES (LBM-LES) as a means of predicting instantaneous flow characteristics and of handling large turbulent flow structures, in contrast to the traditional Reynolds-averaged Navier-Stokes (RANS) approach, which provides only time-averaged flow quantities [56].

Researchers have been working with LBM in combination with other approaches to solving a variety of issues. To simulate a free surface flow in a wide rectangular duct, Fernandino et al. [57] integrated the Smagorinsky subgrid scale

(SGS) model into LBM. While discrepancies were evident in the mean flow structure due to the use of a coarse grid close to the wall, overall, a good qualitative agreement between the experimental and the simulation results were achieved. Dong et al. [58] proposed an inertial-range-consistent Smagorinsky model in LBM for the D3Q19 lattice model as a means of assessing the effectiveness of the LBM-LES technique for solving isotropic turbulent flow at low Mach numbers. In 2008, Dong and Sagaut [59] examined the effect of different subgrid models on time correlations of isotropic turbulence in order to investigate the performance of several Smagorinsky model variants and model coefficients with respect to their time correlation properties in turbulence within an LBM framework. Overall, their findings revealed that the LBM-LES model generally yielded results that were in good agreement with the experimental outcomes as well as with other numerical studies for low-Reynolds-number cases.

In 2009, Chen [60] developed a novel and simple LES-based lattice Boltzmann model for simulating two-dimensional turbulent flows rather than solving the Navier-Stokes equations using the vorticity stream-function equations, and he reported encouraging results. Si and Shi [61] implemented an SGS LES model in LBM in order to demonstrate that LBM-LES can be employed to simulate fluid flow at high Reynolds numbers. To establish the ability of LBM-LES with respect to solving such high-Reynolds-number flows, they presented a detailed

quantitative comparison of the vortex position for turbulent flow inside a cavity. However, the limited ability of conventional LBM in regard to solving compressible flows, especially at Mach numbers higher than 0.1 is well known [15].

At about the same time, Buick and others [62] investigated the capability of the Bhatnagar, Gross, and Krook (BGK) model with respect to simulating sound waves at small density variations, while Lew and others [63] used a commercial code based on the LBM kernel PowerFLOW to predict near-field and far-field jet noise at a Mach number of 0.4. In addition to finding near-field statistics in agreement with other experimental results, the researchers also discovered that the behaviour of the simulated sound waves was in good agreement with analytic expressions. Yu and others [64] employed a multiple relaxation time (MRT) LBM to predict near-field rectangular jet noise at low a Mach number around 0.17. They found the MRT-LBM to be a potentially reliable computational tool for the LES of turbulence even at high Reynolds numbers. Based on this solid research foundation, the goals of the work presented in this thesis were 1) to adopt and extend other related work in order to use LBM-LES in subsonic flow regimes for an examination of compressible turbulent free jets, and 2) to investigate the near-field turbulent jet noise at subsonic speeds using LBM. In the final stage of this research, the LBM approach was combined with Kirchhoff's surface integral theorem in order to predict far-field jet noise.

7.2 Predict jet flow variables

The work conducted in this study was validated via two test cases: isothermal and non-isothermal compressible free jet flow using two LBM models in conjunction with LES. The first model features a high-order equilibrium distribution function (HO) and an isothermal and a non-isothermal compressible flow, while the second employs the Kataoka and Tsutahara (KT) model for an isothermal and a non-isothermal compressible free jet flow. The results were validated against experimental results for circular heated and unheated jets, which established the axial mean velocity profile $U_c(x)$ along the jet axis X/D_j as well as the turbulence intensity $u_x(rms)$. The compressible LBM was used for performing LES that involved the application of two models (the higher-order equilibrium distribution function and the KT model) in order to examine an isothermal and a thermal axisymmetric jet flow at a Mach number of 0.5. The numerical results were validated against the available experimental data from Bridge [34] and Laurendeau [65], and also against Lew's numerical results [63].

Figure 7.1 provides a schematic of the circular (axisymmetric) jet nozzle with reference to the coordinate system used to describe the geometry, where U_c is the mean streamwise velocity along the centerline of the jet at (y = z = 0) and u_x is the streamwise velocity at a cross-stream location.

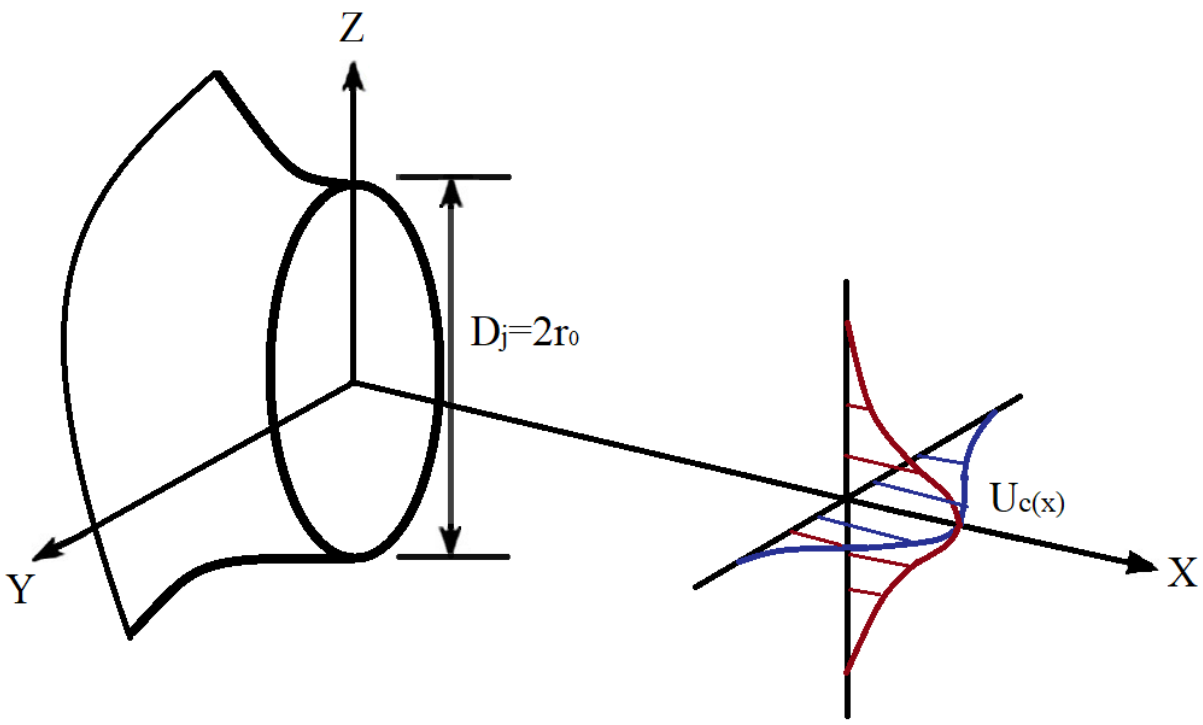

Figure 7.1: Schematic and reference system of a circular jet nozzle.

Table 7.1: Free circular jet characteristics

Test case characteristics	
Jet diameter	$D_j = 0.0508\, m$
Jet exit velocity	$U_j = 130{,}170{,},205\, m/s$
Kinematic viscosity	$\nu = 1.516 * 10^{-5}\ m^2/s$
Reynolds number	$R_{eD} = \frac{U_j D_j}{\nu_j} = 4.35 * 10^5, 5.7 * 10^5,$
Mach number	$M_j = U_j/c = 0.4, 0.5, 0.6$
Simulation dimension (LBM) LBM grid sizing unit =1	$D_{lbm} = 13\ units$ $N_x = 20, 30 D_{lbm}$, $N_y = 5, 6 D_{lbm}$, $N_z = 5, 6 D_{lbm}$ Total number of grid points # $1 * 10^6$, $1.5 * 10^6, 1.6 * 10^6, 1.37 * 10^6$
	$D_{lbm} 18\ units$ $N_x = 20 D_{lbm}$, $N_y = 5 D_{lbm}$, $N_z = 5 D_{lbm}$ Total number of grid points # $2.9 * 10^6$
Δx=0.0020833, $\Delta y = 0.00127$, $\Delta z = 0.00127$,	LBM (Δx_{lbm}=Δy_{lbm}=Δz_{lbm} =1) $\Delta t_{lbm} = 1$
$CFL = \frac{u \Delta t}{\Delta x} = \frac{1}{\sqrt{3}}\ M_j$ =0.23	time step $\Delta t = CFL \frac{\Delta x}{U_j} = 0.5 * 10^{-5}$ sec
Total time steps	44000

7.3 High-order equilibrium distribution function results

One of the first ideas for solving high-Mach-number flows using LBM was to use a high-order equilibrium distribution function (as described in section 3.4) to reduce the truncation error that occurs in the solving of the Maxwell-Boltzmann distribution function. In the work conducted for this thesis, the 6th-order term of the Hermite polynomial expansion of the equilibrium distribution function was applied as a means of alleviating this limitation that is associated with the use of conventional LBM for high-Mach-number flows.

7.3.1 Isothermal compressible free jet flow

Figure 7.2 indicates the decay in the mean streamwise velocity $U_c(x)/U_j$ along the jet centerline axis x/D_j, where U_j is the exit velocity at the jet nozzle and $U_c(x)$ is the local mean streamwise velocity of the jet at its centreline. The case-study LBM-LES results compare very well with Bridges' experimental findings [34] and with Lew's FDM-LES and PowerFLOW [www.exa.com] commercial code results [63]. With the exception of a plateau near the jet exit where the jet core has not yet been obliterated, the mean centerline velocity decays inversely with the jet X-axis. Near the jet exit, the mean velocity is almost constant, and no shear layer effects are yet apparent.

Near to the jet exit $x/D_j < 5$, the mean streamwise velocity $U_c(x)$ at the jet centerline is equal to the jet nozzle exit velocity Uj and this feature of the mean flow

is captured well by all the predicted results (e.g., LBM-LES, FDM-LES, and PowerFlow).

At a slight distance from the jet exit $x/D_j > 5$, in an interaction region where shear layers from the surrounding and the development of turbulent flow downstream affects the centre velocity, the mean velocity at the jet centre decays rapidly with increasing x/D_j . Generally speaking, compared to the experimental and numerical results, the new LBM-LES predictions agree much more closely with the experimental data than Lew's CFD results [63].

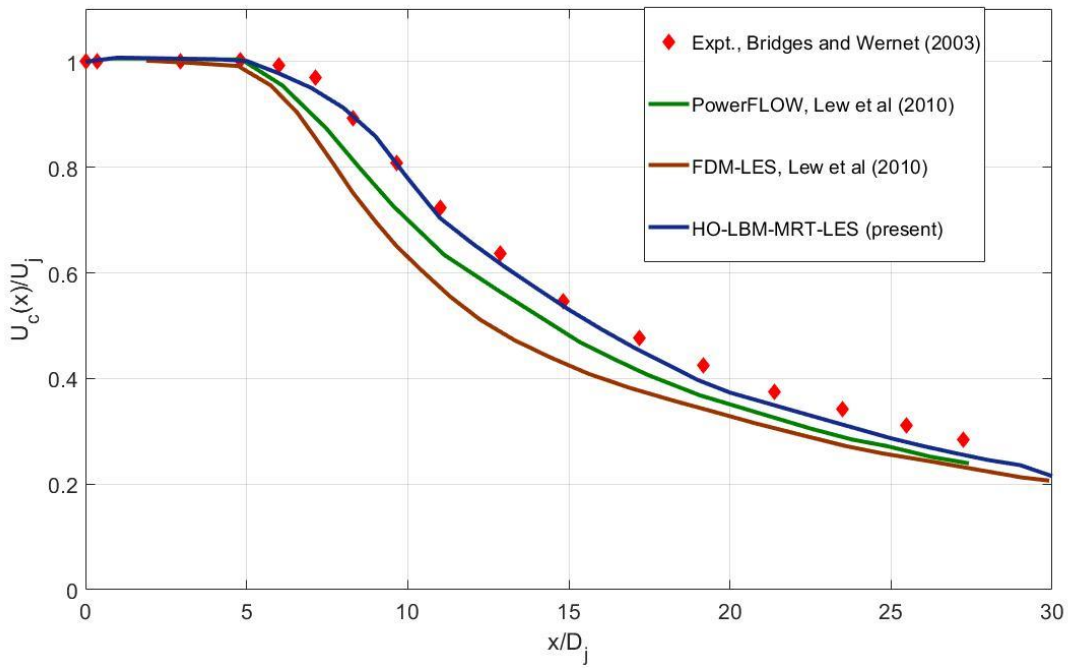

Figure 7.2: Development of the mean streamwise velocity along the centerline of an isothermal round jet for a Mach number, M_j = 0.5.

Figure 7.3 displays our LBM-LES predictions of the downstream development of the normalized streamwise turbulence intensity $u_{rms}(x)$

(normalized by the nozzle jet velocity U_j) along the centerline of the jet at a Mach number of $M_j = 0.5$. These predictions have been compared to similar numerical results obtained by Lew et al. [63] using a finite difference LES code (FDM-LES) and the commercial LBM code PowerFlow. These numerical results are also compared with some experimental data for the streamwise turbulence intensity for an isothermal round jet obtained at a Mach number $M_j = 0.3$. by Laurendeau et al. [65].

For $x/D_j > 10$, the predictions of the streamwise turbulence intensity provided by LBM-LES, FDM-LES, and PowerFlow are generally in good agreement with the experimental measurements, albeit the simulations are seen to slightly overestimate the streamwise turbulence intensity over this range of downstream fetches. For downstream fetches in the range $x/D_j < 10$ the LBM-LES predictions of $u_{rms}(x)$ are in better conformance with the experimental data than the predictions provided by FDM-LES and PowerFlow. All three numerical models predict that the normalized streamwise turbulence intensity attains a peak value at a normalized downstream distance $x/D_j$of about 18 and decreases with increasing downstream fetch thereafter. Furthermore, all three numerical simulations predict a similar rate of decrease of the streamwise turbulence intensity with increasing downstream fetch for $x/D_j > 18$. Finally, over the range of downstream fetches x/D_j between about

5 and 18, the streamwise turbulence intensity is seen to increase with increasing downstream distance. In this regime of development, the entrainment of the ambient fluid into the jet (viz., the external irrotational fluid is engulfed into the core of the jet through its increasingly convoluted outer edge) results in the increase of the local intensity of the turbulent fluctuations in the jet.

In conclusion, the LBM-LES results, the upper jet boundary is more unstable and exhibits a region of greater turbulence intensity $7 < x/D_j < 18$. As well, the shear layers of the jet actively participate in the entrainment of ambient fluid, and the growth of turbulent flow fluctuates rapidly. At the lower jet boundary $x/D_j > 18$, the turbulence intensity starts to decrease slightly with an increase in the axial distance because the mean velocity decreases downstream. Although the results produced by the new LBM are slightly higher than the experimental findings, they compare well with Lew's numerical conclusions [63] .

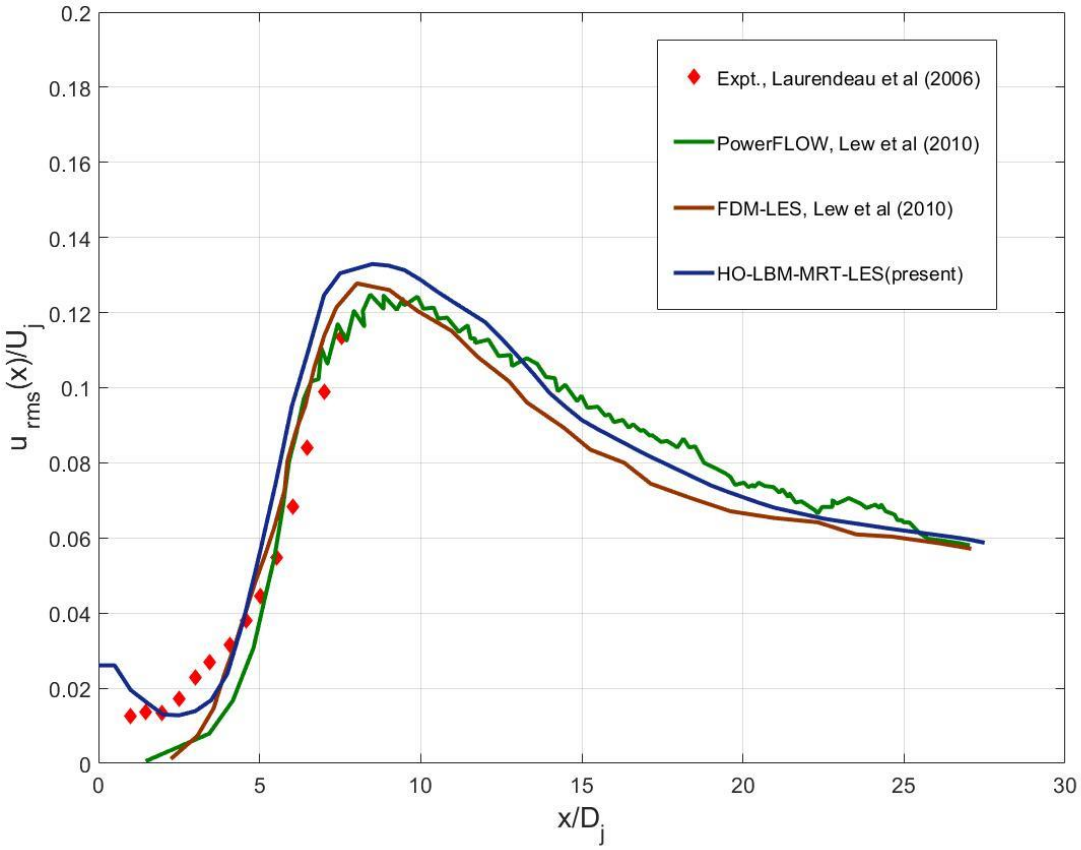

Figure 7.3: Development of the streamwise turbulence intensity along the centerline of an isothermal round jet for a Mach number, M_j = 0.5.

7.3.2 Non-isothermal compressible free jet flow

This section describes the assessment of a non-isothermal free jet conducted with the goal of examining the effect of temperature on the mean centerline velocity and the turbulence intensity along the jet x-axis. For non-isothermal jet flow, the distribution function was applied in its full version, so any terms that have a relative temperature T_j/T_0 in the equilibrium distribution function given in Eq. (3.7) do not vanish. The full version of the equilibrium distribution function was also used with

two relative temperatures: $T_j/T_0 = 0.95$ and $T_j/T_0 = 1.76$. where T_0 is the ambient temperature and T_j is the jet exit temperature.

Figures 7.4 and 7.5 reveal that temperature has a significant effect on velocity and turbulence intensity distributions [34]. In the fully developed zone, the temperature has less effect on the flow, and the turbulence intensity reduces quickly, resulting in a slower mean velocity. Figure 7.4 demonstrates how the centerline mean velocity of a heated jet $T_j/T_0 = 1.76$ decays at a faster rate downstream when the relative temperature T_j/T_0 is increasing. The impact of relative temperature T_j/T_0 on the streamwise (or axial) turbulence intensity along the centerline of the jet is depicted in Figure 7.5.

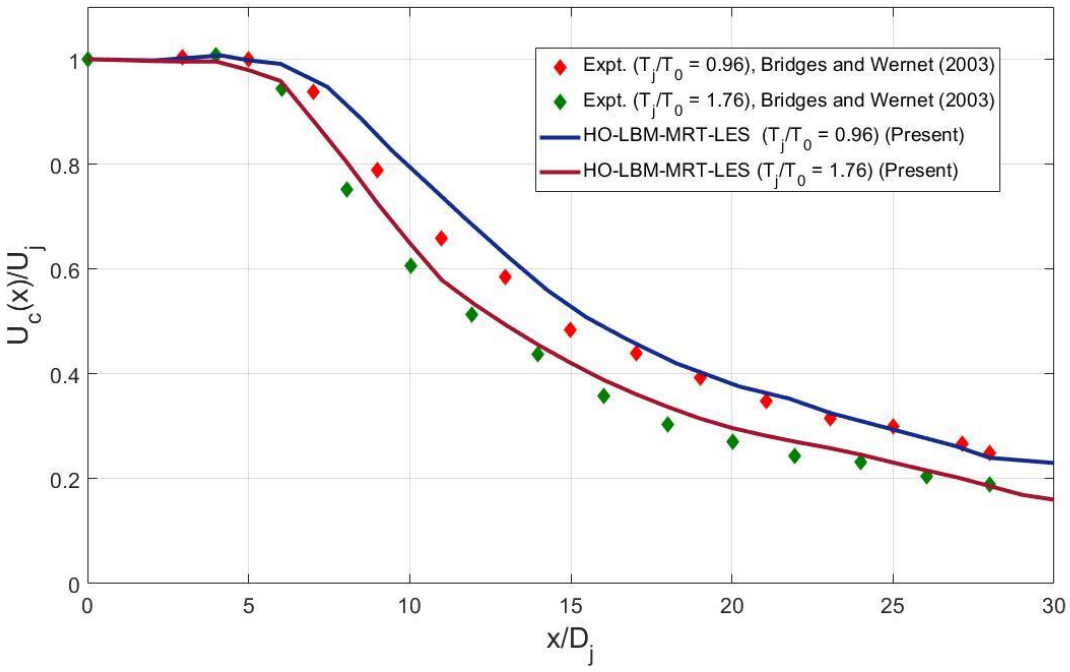

Figure 7.4: Effect of temperature on the distribution of the mean velocity at the centerline, M_j= 0.5.

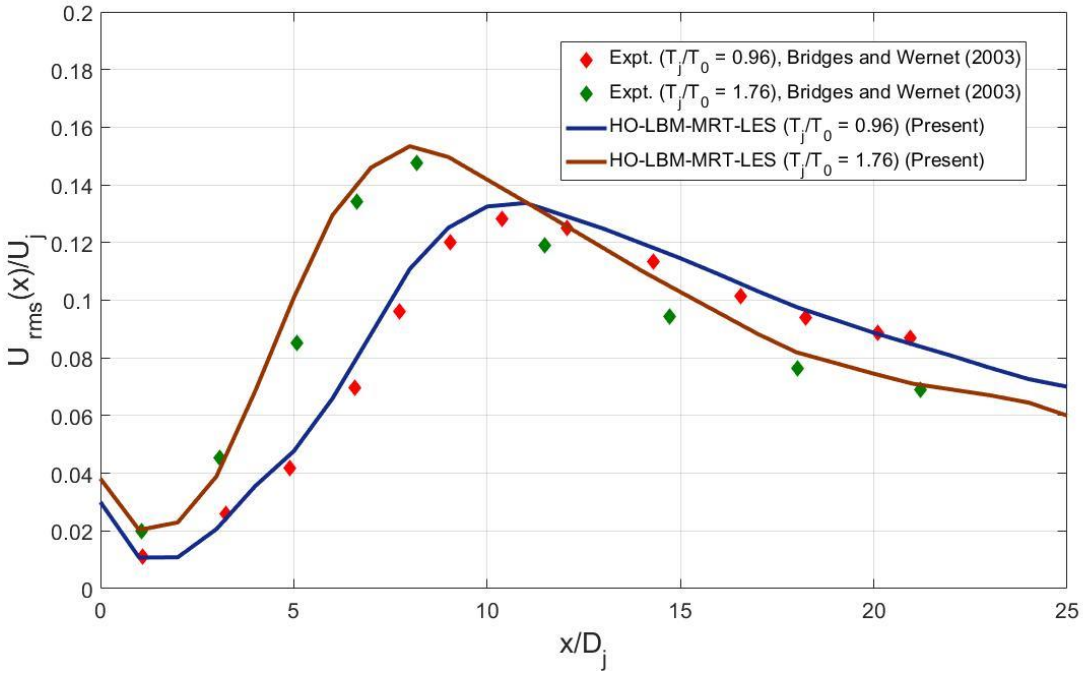

Figure 7.5: The effects of temperature on the downstream development of the normalized streamwise turbulence intensity along the centerline of a heated round jet for a Mach number, M_j = 0.5.

It can be observed that, for a heated jet, the streamwise turbulence intensity at $T_j/T_0 = 1.76$ is greater than that at $T_j/T_0 = 0.95$. The effect of heated jets on the mean velocity along the centerline is a reduction in the centerline velocity of the jet. Meanwhile, the turbulence intensity increases, especially in the region $^{x}/_{D_j} =$ 3 to $^{x}/_{D_j} = 10$, where large local shear leads to high values of turbulence production. This trend is in agreement with both the experimental and numerical results.

7.4 Kataoka and Tsutahara model

In the research for this thesis, the KT version of LBM [2] was used with the D3Q15 model in conjunction with LES in order to solve compressible unheated and heated jet flows. The new KT-LES model was implemented via the simulation of subsonic jet flow, and the predictions produced were compared with the available experimental and numerical results.

7.4.1 Isothermal compressible free jet flow

Figure 7.6 depicts the variations in the mean streamwise velocity u_x/U_j along the centerline of the jet, as obtained with the KT model and compared with Bridges' experimental data [34] and Lew's PowerFLOW (www.exa.com) and FDM-LES results [63]. The u_x-velocity predicted by the KT model decays faster than the values from the experimental data along the centerline of the jet (i.e., in the x/D_j-direction). However, the KT results agree well with those produced by the PowerFLOW commercial code.

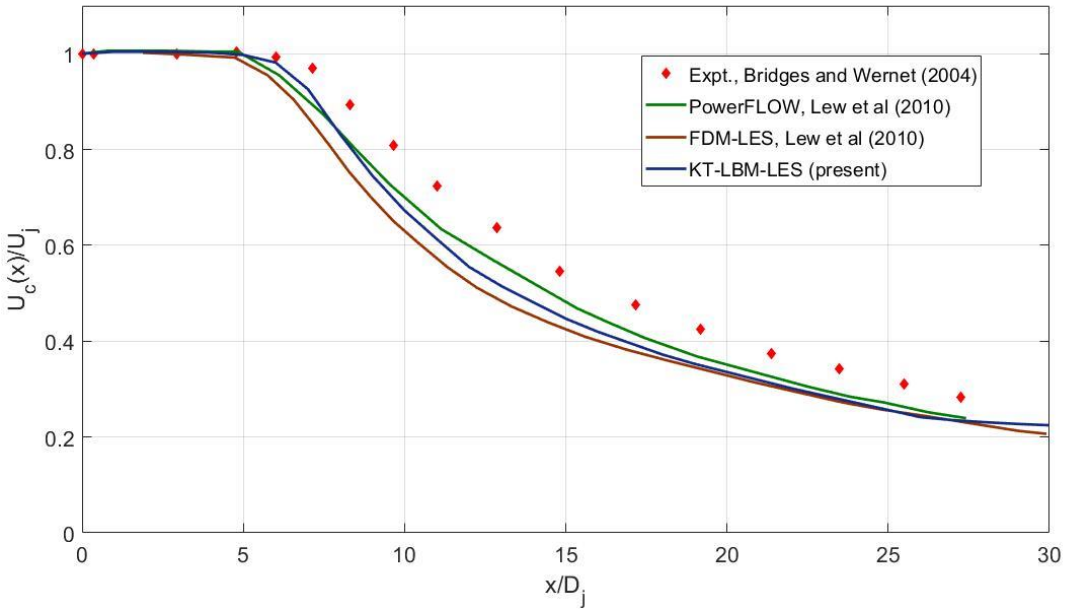

Figure 7.6: Development of the mean streamwise velocity decay along the jet centerline axis obtained with the KT model, M_j = 0.5.

With respect to streamwise (or axial) turbulence intensity, Figure 7.7 shows that the KT model results exhibit some disagreement with the Laurendeau experiments [65] near the entrance region, where $^{x}/_{D_j} < 10$. After that point, however, the KT model predictions compare well with the PowerFLOW and FDM-LES results but not compared very well with the experimental results and this related to the KT model derivation, which has many assumptions and new variables to control the specific heat ration.

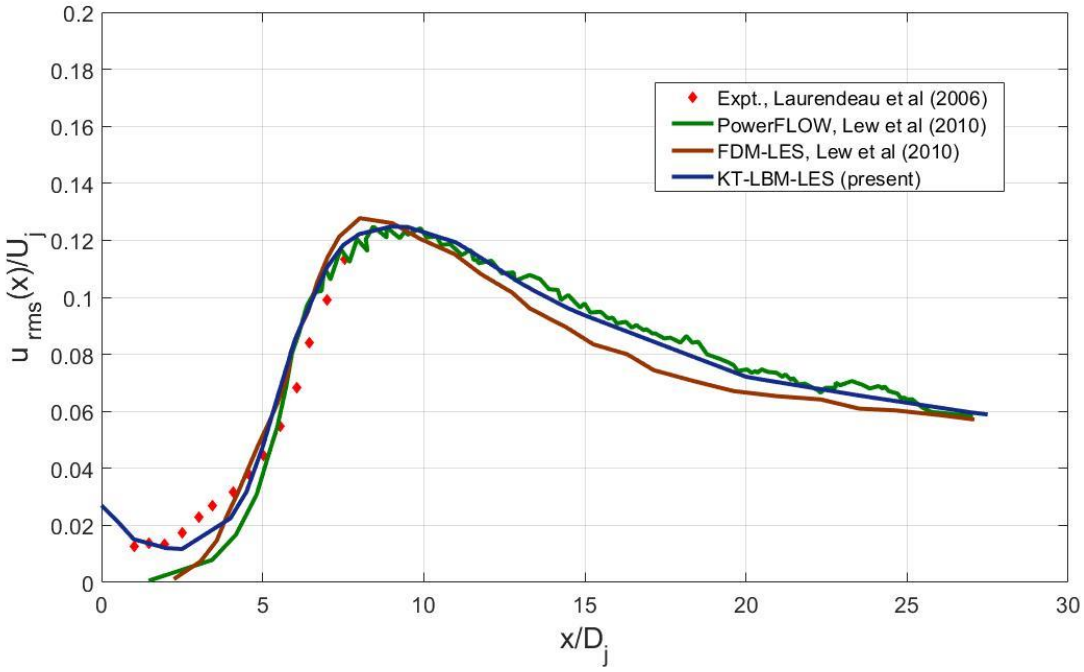

Figure 7.7: Development of the streamwise turbulence intensity along the centerline of an isothermal circular jet obtained with the KT model, M_j = 0.5.

7.4.2 Non-isothermal compressible free jet flow

A re-examination of the same heated jet using the KT model rather than the high-order equilibrium distribution function approach, with two relative temperatures $^{T}/_{T_0} = 0.950$ and $^{T}/_{T_0} = 1.76$, revealed the major effect of temperature when the equilibrium distribution function is used. As the temperature increases, the molecules energize and move more quickly. These changes affect the flow properties of pressure, density, and velocity, which are dependent properties. When a fixed Prandtl number such as 1 is employed in the KT model, the KT-LES

results indicate a small deviation from the experimental results but within an acceptable range.

The non-isothermal KT model results also show that the centerline velocity U_c decays slightly faster than is evident in either the experimental or numerical results because the viscosity has changed with the temperature. Subsequent changes are also evident in the relaxation time, which is a function of fluid viscosity. Compared with the experimental data, the results predicted by the KT model are generally good, as is clear from Figures 7.8 and 7.9. In contrast to the results produced using the high-order equilibrium distribution function approach, the mean velocity and the turbulence intensity along the centerline of the jet obtained with the KT model are slightly lower than the experimental data values due to the application of a different equilibrium distribution function. The type of equilibrium distribution function used plays a key role in the performance of compressible LBM models.

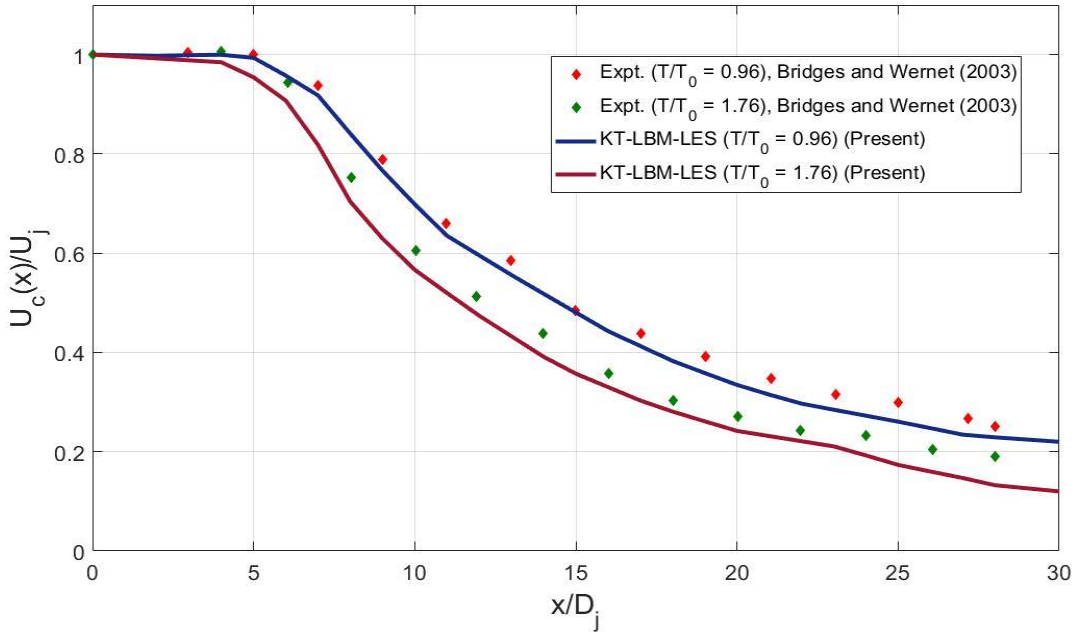

Figure 7.8: The effects of temperature on the centerline distribution of the mean velocity with the KT model, M_j = 0.5.

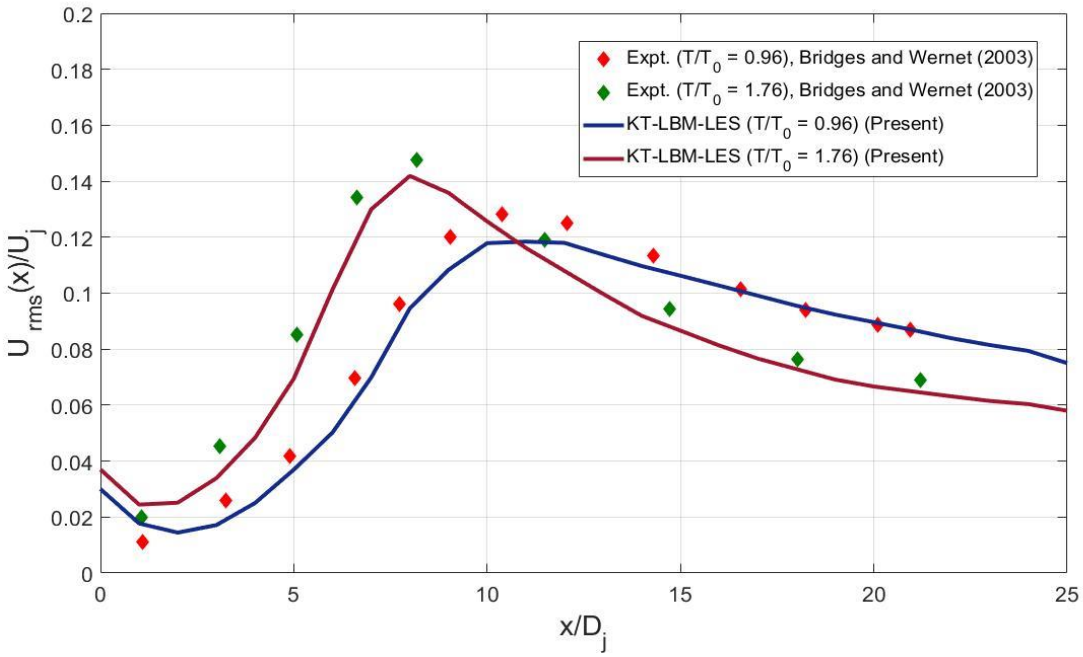

Figure 7.9: The effects of temperature on the downstream development of the normalized streamwise turbulence intensity along the centerline of a heated round jet obtained with the KT model, M_j = 0.5.

With respect to the LES of turbulent jet flows, the results with both the experimental and numerical computations obtained with a 3D code based on D3Q19 and those from the KT models match perfectly.

7.5 Near-field noise predictions

Over the past few decades, experimental and numerical studies have provided the best understanding of jet noise for both near-field and far-field predictions. All of these methods require accurate results for measuring or computing the flow of near-field properties. LBM is currently considered a precise CFD method that offers numerous advantages for predicting near-field and far-field jet acoustics, especially pressure distribution, as calculated in Eq. (3.14). The maximum resolvable Strouhal number for this type of simulation is expressed as $St_{max} = f_{max}\, D_j/U_j = 2$, where the maximum frequency is computed via $f_{max} = c_\infty/\lambda = 4000Hz$, where c_∞ is the speed of sound and λ is the wavelength $\lambda = 12\Delta$, and where Δ is the grid spacing at the probe location $\Delta = 0.8$ mm. This section discusses the near-field flow properties related to noise, such as velocity contour, pressure distribution, and sound pressure level.

Figure 7.10 presents the cross-stream profiles of the normalized mean streamwise velocity at various downstream locations for the isothermal round jet at a Mach number $M_j = 0.5$. As can be seen, the uniform mean streamwise velocity near the exit of the nozzle evolves with increasing downstream fetch x/D_j as the

shape of the velocity profiles transitions from the sharper square pulse shape near the nozzle to a more diffuse Gaussian shape further from the nozzle exit (as the jet evolves into the self-similar regime of development). This development is consistent with the entrainment of the ambient irrotational fluid into the jet core through the convoluted outer edge of the jet, leading to the flow towards the jet that feeds its increasing girth (local jet width). This can be seen more clearly in Figure 10.11, which shows the isocontours for the time-averaged velocity (normalized by the velocity at the jet nozzle) in a horizontal (x-y) plane through the jet at a fixed time. Here, it is evident that the outer edge of the jet is convoluted and corresponds to the interface between two regions of the fluid, representing a sudden transition from the turbulent vorticity field in the jet core to the external (ambient) irrotational fluid. In particular, the free shear layer between the high-vorticity flow in the jet core and the ambient fluid create the convoluted outer edge of the jet, particularly for downstream fetches x/D_j greater than about 8.

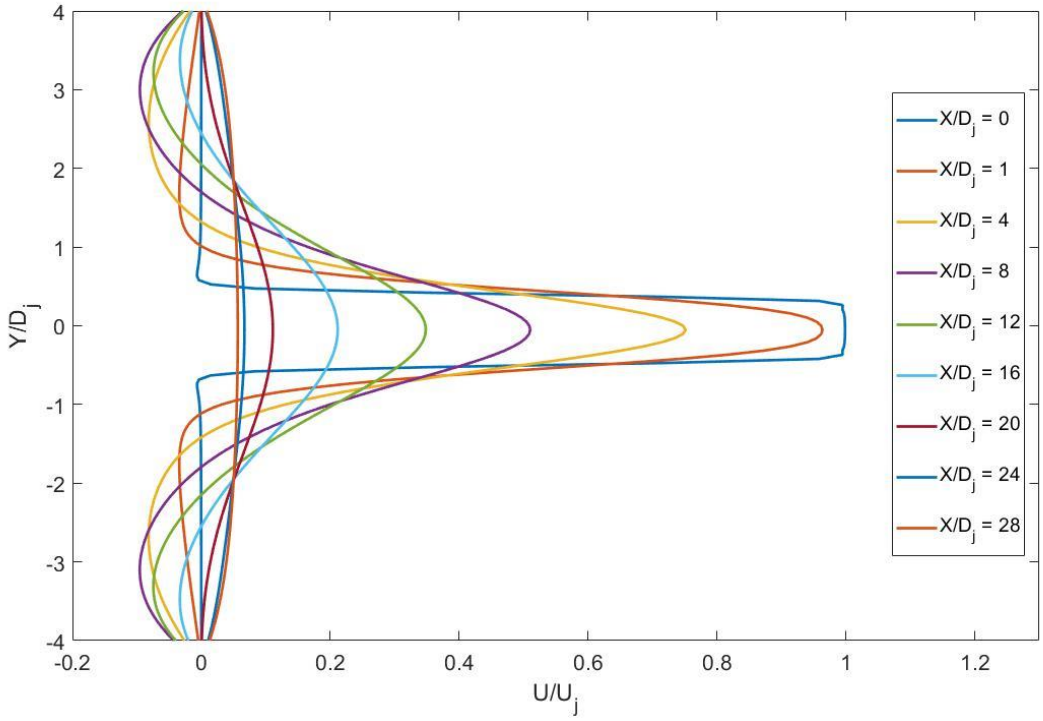

Figure 7.10: Cross-stream profiles of the normalized mean streamwise velocity U/U_j at various downstream locations x/D_j along the centerline of an isothermal round jet at a Mach number , M_j = 0.5.

Figure 7.11 reveals the growth of time-averaged velocity as it moves downstream. The shear layer between the high-vorticity jet flow and the ambient stagnation air create a convoluted edge in the velocity profile and cause the development of turbulence after $x/D_j = 8$, as illustrated in Figure 7.12.

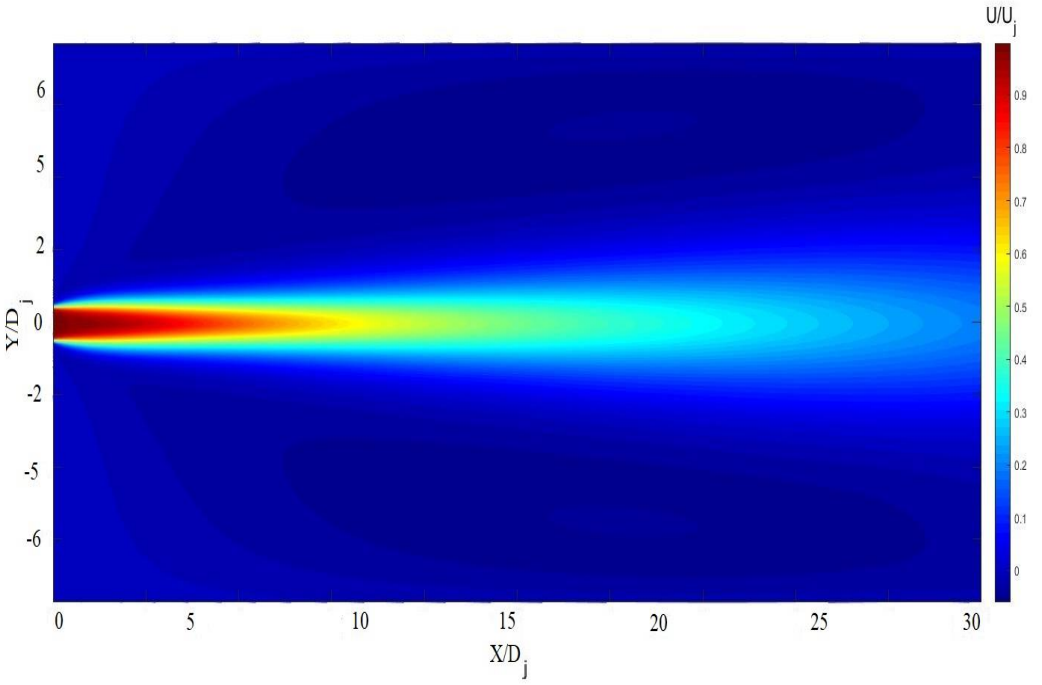

Figure 7.11: Axial time-averaged velocity contour, $U/U_j, M_j = 0.5$.

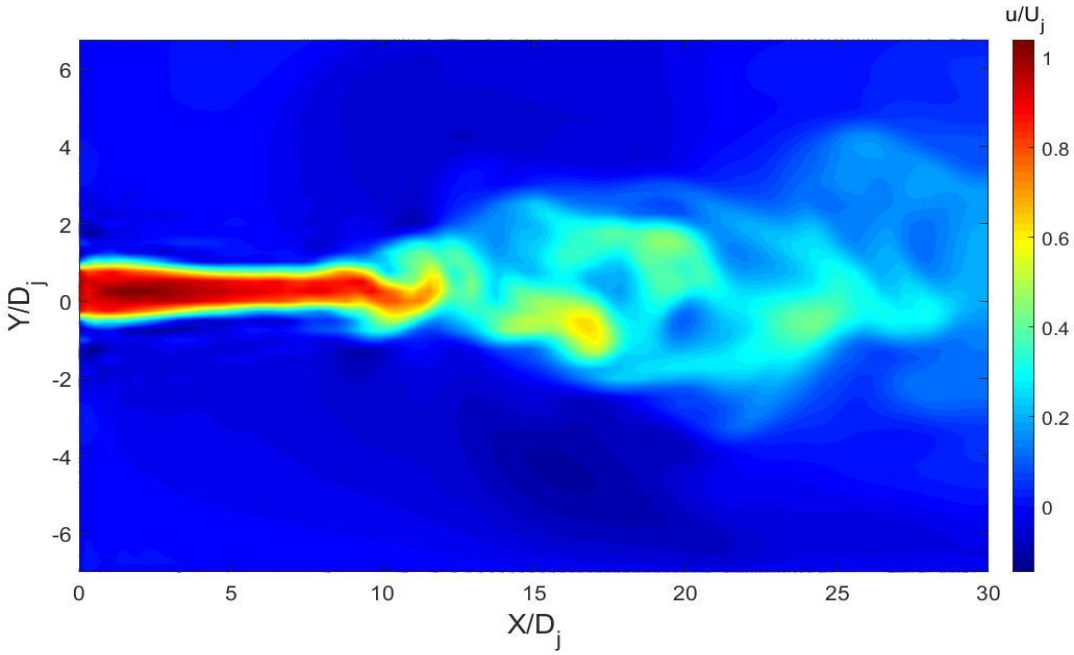

Figure 7.12: Isocontour of the instantaneous streamwise velocity for an isothermal round jet at a Mach $M_j = 0.5$ obtained in a horizontal plane through the jet flow at a fixed instant in time.

Figure 7.13 indicates that the Mach number decreases with increasing x/D_j. When the mixing of the developing region occurs, the Mach number decreases in the radial direction, and an elliptic zone is created above the shear layer zone. This effect means that most of the sound propagation is generated from this area.

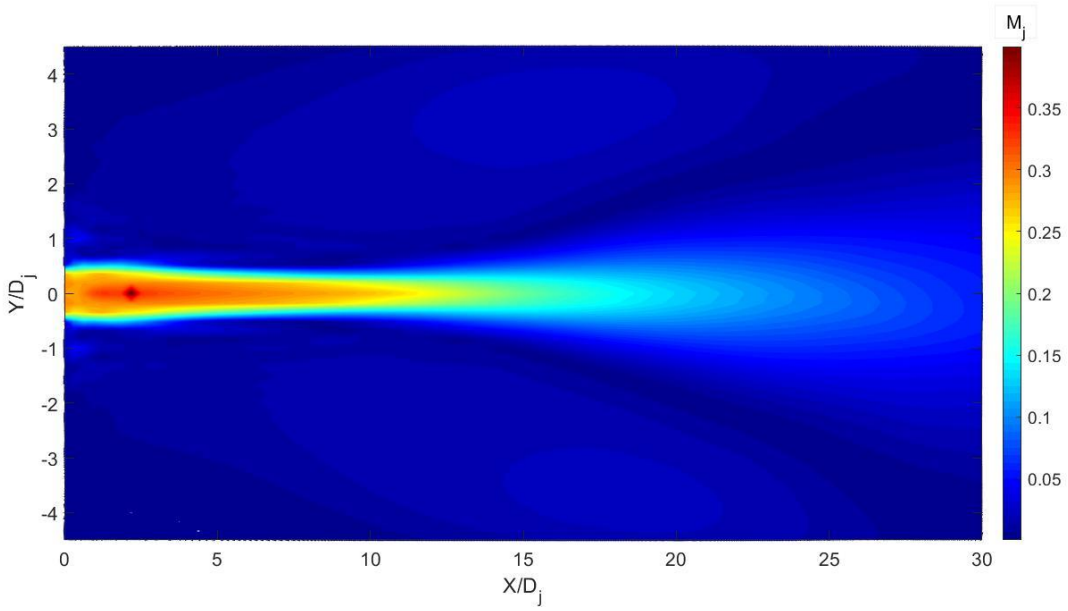

Figure 7.13: Mach contour, M_j = 0.5.

The downstream propagation of high-frequency sound waves from a subsonic jet creates what is called a cone of silence. Figure 7.14 shoes the sound pressure level distribution $SPL == 20\log_{10}\left(\frac{p_{rms}}{p_{ref}}\right)$ in the flow domain, where is $p_{ref} = 20 \times 10^{-5} Pa$ (threshold of hearing). The cone of silence can be seen outside of the shear layer in the developing region.

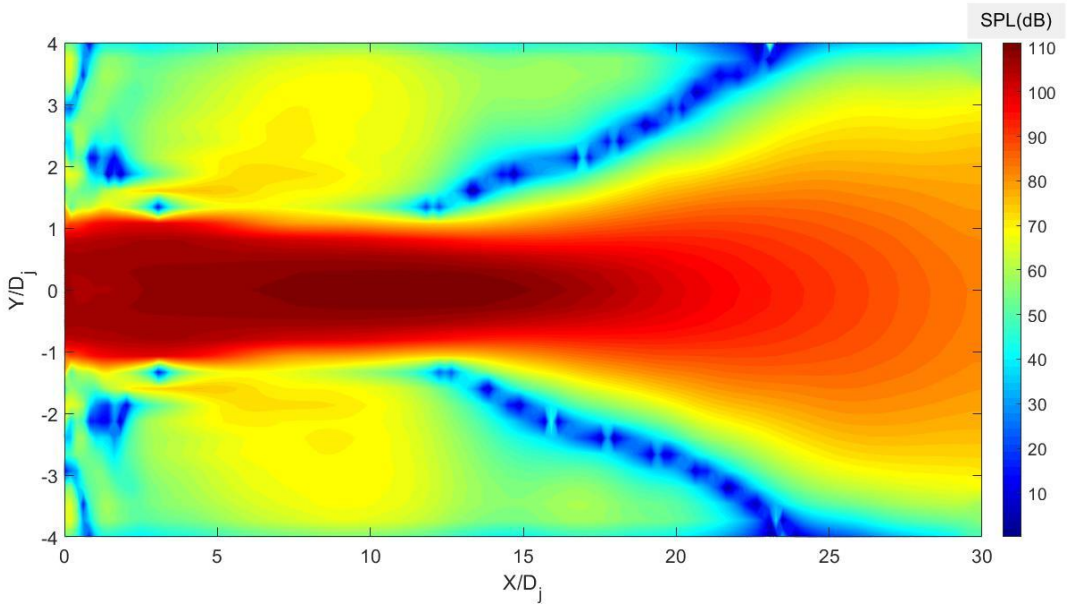

Figure 7. 14: Sound pressure level contour, M_j = 0.5.

To obtain the results plotted in Figure 7.15, sound pressure signals were monitored along the jet x-axis. For subsonic jets, at the radial positions $y = 0, y = 0.5D_j, y = 1D_j$, the lines extend from the jet exit $x = 0$ up to $x = 30D_j$. At the centerline of the jet $y = 0$, the sound pressure level decreases linearly to the developing zone, which compares very well with Mancinelli's experimental results at Mach 0.6 [66]. When moving radially from the centerline of the jet, the sound pressure from the jet exit $x = 0$ begins to increase to the maximum local value of the sound pressure level in the potential core. It then starts to decrease until it reaches the middle of the jet x-axis $x = 15D_j$, where the cone of silence is generated.

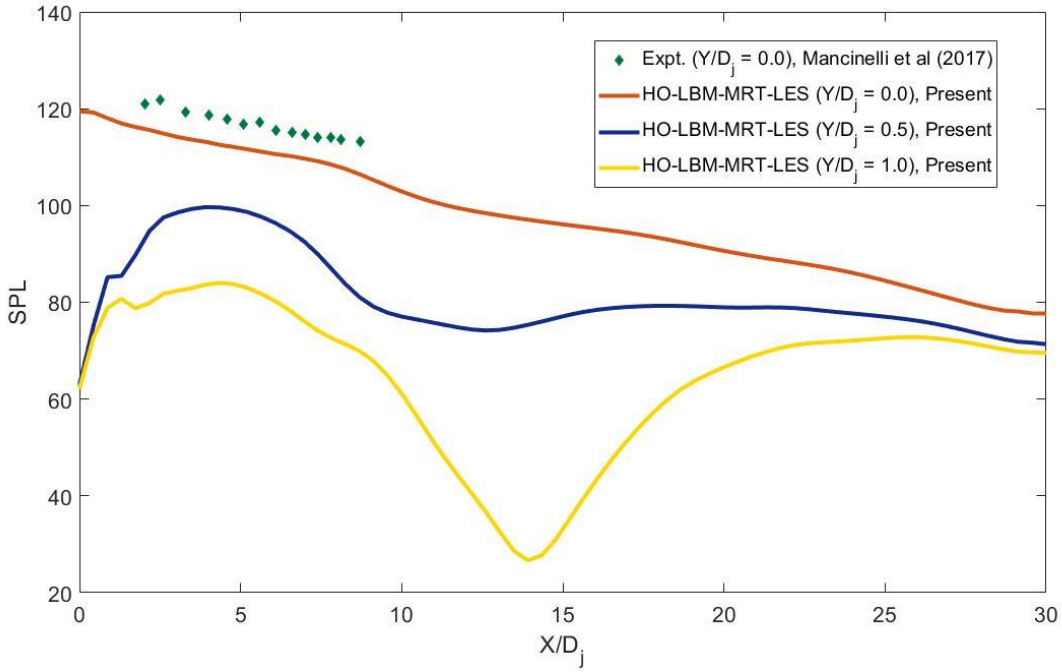

Figure 7.15: Sound pressure level at jet centerline, lip line, and shear layer, $M_j = 0.5$

7.5 Far-field noise predictions

The work in this thesis included a sequential and comprehensive study of the use of compressible LBM for simulating a subsonic free stream jet. After the LBM limitations had been overcome and a free jet flow had been simulated, the next step was to examine near-field jet noise as described in the previous section. This section explains how the Kirchhoff integral approach was applied for predicting noise in the far-field. The sound pressure levels will predict at observer distance $r = 72D_j$ in a range of angles θ = 20º to θ = 90º

The properties of the initial jet disturbances were investigated based on calculations of the spectra of the fluctuating axial velocity at an axial distance

$x = 10D_j$ downstream along the centerline of the jet, as shown in Figure 7.16. Good agreement exists with other numerical results reported by Lew [63] using two different methods: PowerFLOW commercial software and the LES method. The LBM spectra can be seen to fall within a reasonable range compared with Lew's LES calculations.

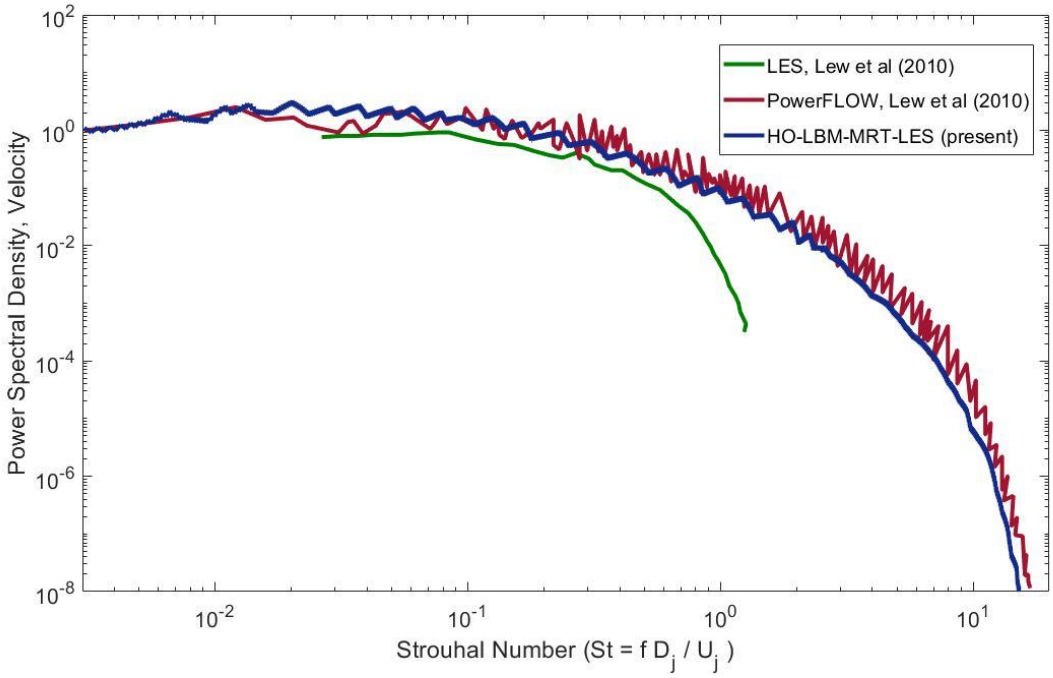

Figure 7.16: Streamwise velocity spectra at $x = 20\mathrm{r}_0$ located along the centerline of the jet, $M_j = 0.5$.

The maximum Strouhal number is $St_{max} = f_{max}D_j/U_j$, whereas the maximum LBM frequency is $f_{max} = u/\lambda$, where u is the jet mean velocity and $\lambda = 12\Delta x$, Δx is the LBM grid spacing at the probe location, at least 12 voxels are needed to resolve one acoustic wavelength [67]. Because LBM-LES can capture smaller

eddies than LES from Lew results due to the coarse grid used in the LES method, LBM-LES is thus more valuable for simulating turbulent flows than other numerical methods. LBM can hence be used with an aeroacoustics hybrid approach for predicting noise generated from turbulence flows in both near- and far-field locations.

The sound pressure levels in the far-field locations shown in Figure 7.18 were obtained from LBM-LES-Kirchhoff and validated against the experimental and numerical results obtained from Tanna [68].

The predicted noise levels are for angles of θ = 15º to θ = 90º from the centerline of the jet within less than 3 dB of deviation from Tanna's [68] experimental measurements (indicated by the dotted lines in the figure). In the aeroacoustics field, the numerical prediction deviation +-3 dB considered in good agreement with the experimental data. The results show that the sound pressure levels increase gradually with rising elevation angles, reaching a peak between θ = 30º and θ = 60º, where the flow exhibits a high-turbulence-intensity velocity, as shown in Figure 7.17.

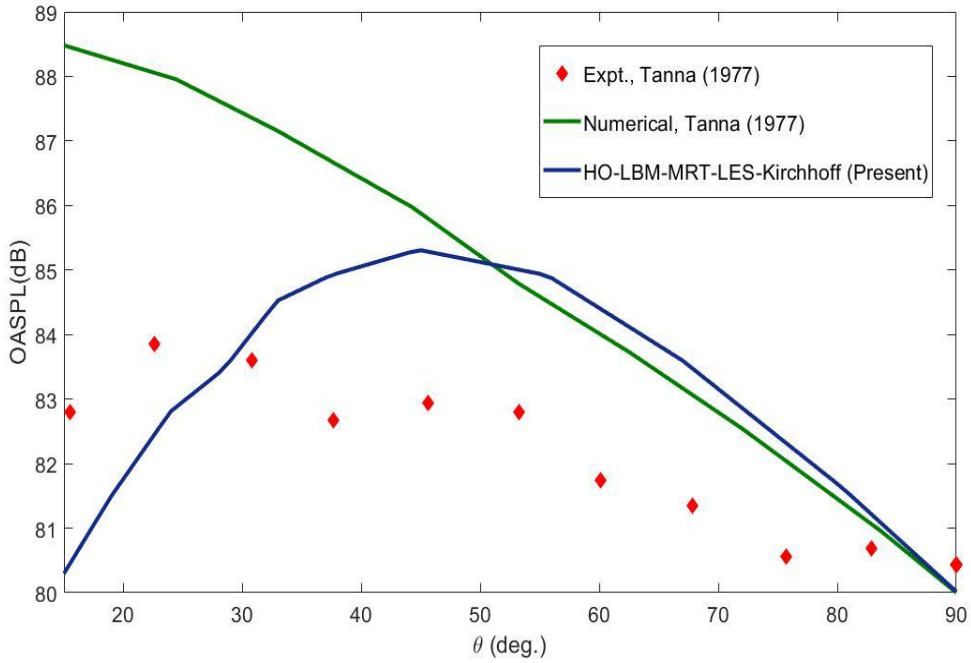

Figure 7.17: Directivity of the overall sound pressure level (OASPL) at $R = 72D_j$, with the observation angle θ measured relative to the jet centerline axis, $M_j = 0.5$.

Figure 7.18 indicates the sound pressure spectrum in the upstream area at *x* = 0 for a fixed radial location (r = 10*Dj*). As the numerical results predict, the sound pressure spectra show distinct peaks at low frequencies because pressure fluctuations are steadier at smaller amplitudes. At high frequencies, however, pressure fluctuations are characterized by high amplitudes, thus generating large sound pressure spectra variations as the pressure frequency increases.

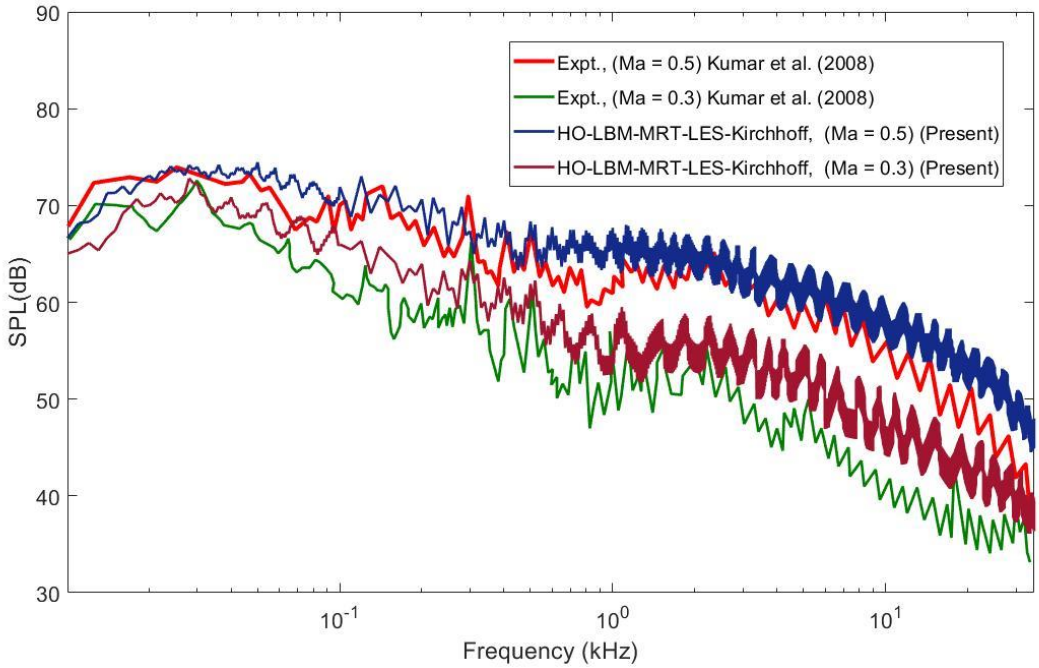

Figure 7.18: Sound pressure spectra at $x = 0$ and $r = 10D_j$, $M_j = 0.3$ and 0.5.

The high-pressure spectra at low frequencies are attributable to the strong tones in the flow field. In general, the pressure spectra are in good agreement with the experimental results introduced at the same location and for a similar flow simulation.

7.6 Summary

This chapter has presented a compressible lattice Boltzmann subgrid model for simulating fluid flows at subsonic flows. The essential concept of applying the subgrid model in a compressible LBM (CLBM) is based on the assumption that all of the physical effects that the unresolved motion has on the resolved fluid motion are included [61]. The results obtained through the application of LES with CLBM

for solving subsonic jet flows show good agreement with the experimental findings. The numerical results indicate a top-hat shape for the streamwise mean velocity distribution at a given axial location, which is well represented by the new compressible LBM for assessing compressible heated and unheated jets using either the high-order equilibrium distribution function approach presented in section 3.4 or the KT model introduced in section 3.5. The agreement between the predictions obtained with the new LBM (in terms of mean velocity and turbulence intensity) and those produced by other numerical and experimental methods is also notably excellent, suggesting that LES models work well for solving compressible lattice Boltzmann problems.

As well, the agreement between the predictions from the new LBM (in terms of mean velocity and turbulence intensity) and the other numerical and experimental results is also excellent, suggesting that the newly developed in-house LBM-LES code has been properly validated. The good agreement between the LBM-LES technique and the experimental data with respect to measuring the velocity field reinforces the relevance of the results presented as a new accurate method for solving compressible flows using traditional compressible LBM models that employ LES for solving compressible turbulence flows. The near-field properties of jet noise have been described in terms of sound pressure distribution, sound pressure levels, and spectra. Their variations from the jet X-axis and radial direction [69], as well as the

sound source distributions, were found to be in good agreement with well-known features of jet noise.

Section 7.5 described the inclusion of the LBM simulation code using the Kirchhoff surface integral approach for predicting far-field jet noise. This innovation was accomplished through the generation of the Kirchhoff control surface around the jet in a radial distance above the jet shear layer in order to include all nonlinearities. The directivity of the overall sound pressure levels observed along arc r = 72*Dj* in the range of angles $\theta = 20^{o}$ to $\theta = 90^{o}$ were simulated and compared with the findings from available experimental studies. The sound pressure spectra near the jet exit were also presented in radial distance running at r = 10*Dj*.

After multiple relaxation times have been applied and the LES approach implemented in LBM, the C++ code can become very cumbersome for execution in CPUs; combining the Kirchhoff approach with all of the other methods [70] likewise causes the computer to run very slowly. To counter this effect, parallel computing, such as with a GPU, was employed because it is faster and easy to install inside a CPU in one chip or more, and the program was then run in single or parallel GPUs. This approach is the focus of the next chapter.

Chapter 8

Efficient Implementation of the Lattice Boltzmann Method on a GPU for Predicting Near-Field and Far-field Jet Noise

8.1 Introduction

Today's new airplanes are generally quieter than older models because the designers must satisfy standards and regulations for reducing noise emissions, and they also wish to please customers who prefer a quieter flight. However, airport community noise still continues to be an important environmental issue because the number of models and sizes of aircraft being manufactured is increasing every day, which means that the additional noise pollution being generated is likely disturbing people who live and work in the vicinity of airports.

One of the primary sources of noise produced by an aircraft is jet noise, which is an important environmental issue for people living or working near airports because of the close proximity of the noise source and the continual increase in the number of flights [71]. The first attempts to characterize sources of aerodynamic jet noise were reported by Sir James Lighthill in 1952 [40]. He based his theory on a rearrangement of the Navier-Stokes equations as wave equations and used the

emission or propagation theory to study the sound radiated in a uniform medium at rest. Whenever a high-speed fluid flow moves from a nozzle, aperture, or orifice into the surrounding region, the velocity shear generates turbulence in the ambient air. The very high velocity and the associated turbulent fluctuations generate noise across long distances from the jet [40]. Sound is a vibration or a sequence of waves of pressure that propagate through compressible media, such as air, water, or solids [72]. The sound wave frequency that is perceptible by humans is about 20 Hz to 20,000 Hz [73]. The velocity, pressure, and density properties of the air determine the speed of the sound, so solving the compressible Navier-Stokes equation provides complete information about sound pressure at observers' locations in near-field and far-field regions.

However, the direct simulation of far-field jet noise can be extremely expensive due to the very large computational domain involved [74]. The term aeroacoustics refers to the noise created by gases flowing at high speed and pressure, which create sound waves that travel through the surrounding media to the observer [75]. The numerical solution of aeroacoustics problems falls within the area of computational aeroacoustics (CAA), which constitutes the most comprehensive method for simulating aeroacoustics problems. CAA simulations involve the computation of pressure disturbances in the flow stream.

For the research presented in this thesis, a lattice Boltzmann method (LBM) was employed for simulating near-field jet flow properties, and Kirchhoff's surface integral method was then applied for predicting sound emissions for the far-field region. Capturing turbulence in the near-field region is essential for the accurate prediction of fluctuations in the source pressure, which is the primary factor in the propagation of the generated sound to the far-field region. A near-field sound region denotes the area closest to the noise source in which the sound pressure decreases by no more than 6 dB when the distance from the source is increased [73]. In this region, the acoustic particle velocity and sound pressure are not in phase. In other words, the near-field region is limited to a distance from the source that is equal to about a wavelength of sound or to three times the largest dimension of the sound source [76].

A far-field noise region begins at the end of the near-field region and extends either to the point at which the sound effect disappears or to infinity. Between the near-field and far-field regions is a small transition region [77], so care should be taken to start the aeroacoustics calculations at the end of the near-field region. In the far-field region, the direct field radiated by most machinery sources decays at the rate of 6 dB each time the distance from the source is doubled [78]. For line sources, such as traffic noise, the decay rate varies between 3 dB and 4 dB each time the distance from the source is doubled [79].

8.2 Literature review

Commercial and fighter aircraft can be subject to new regulations concerning noise emissions due to the noise pollution they create, especially at take-off. Over the past few decades, a number of research programs have been undertaken with the goal of studying the problems associated with the noise pollution from several noise sources, such as vehicles, wind farms, and jet engines because of their detrimental effects on the surrounding environment. Most researchers considered supersonic jets as a primary noise source in airport areas due to the very substantial noise emissions emanating from supersonic aircraft. The numerical prediction of the noise produced from supersonic jets is quite easy because the acoustic source is intense and can be easily captured in a near-field simulation domain. However, the airplane take-off phase, which is the main cause of noise pollution near airports, occurs when the flight is subsonic.

The most valuable experimental studies of jet characteristics and near- and far-field noise were presented by Tanna and others in 1973 [80] with respect to turbulent mixing noise from jets. These researchers investigated the characteristics of the spectra and directivity of turbulent jet mixing noise in the far-field at the subsonic range. They then expanded their study to include supersonic flows over intensive conditions, such as jet exit velocity and temperature effects. Their work

contributed to the body of knowledge about the flow acoustics of jets under a variety of conditions, and they also recommended that further theoretical research be conducted to improve on the experimental results obtained and to apply different conditions of practical interest in order to provide a greater physical understanding.

In 1977, Tanna [68] presented a second paper based on work conducted at a Lockheed-Georgia Company laboratory. His experimental study was centred on shock-free supersonic jet noise and demonstrated the far-field noise of turbulent jets over an extensive set of jet operating conditions. His work included the separate assessment of changes in detailed jet noise caused by varying velocities and exhaust temperatures. Differences were evident between his model and the measurements because of the mean velocity and temperature gradients surrounding the sources.

In related research, in 2002, Harper-Bourne [81] developed practical methods for predicting near-field military jet noise from high-speed jet engine exhaust. He worked from a semi-empirical basis that married aeroacoustics theory with source location data in order to predict the near-field jet mixing noise of both supersonic and subsonic jets. The overall acoustic measurements appeared to be well predicted by the mathematical model, with any discrepancies between the experimental measurements and those of the mathematical model being attributable mainly to the test environment.

More recently, Bogey and others [82] conducted a 2007 experimental study directed at determining the characteristics of noise radiated by both cold and isothermal high-speed round jets. The researchers described this noise in terms of levels and spectra without resorting to extrapolation methods, which might lead to uncertainties in the far pressure fields. The goal of the research was to obtain highly accurate results in order to form a database that can be used for the validation of aeroacoustics prediction methods. One year later, in 2008, Loh and others [83] simulated a subsonic co-annular jet at a high Reynolds number using the finite volume large-eddy simulation (LES) method in three dimensions in order to predict the noise generated in near-field flows. Their simulation proved that the low-order (2^{nd} order) finite-volume LES method can be trusted to capture subsonic co-annular jet properties, but far-field noise was still not accurately characterized in this study.

In the same year, Bodony and Lele [84] employed LES for examining the current status of jet noise predictions. They introduced a computational fluid dynamics (CFD) simulation of compressible jet flow based on a subgrid scale (SGS) model for a wide range of Mach numbers. The study was focussed specifically on the manner in which LES results affect jet noise prediction. The authors concluded that the capability of LES with respect to the accurate prediction of both near-field and far-field turbulent jet noise was significantly increased. They also raised the

issue of the limitation associated with LES for low-Reynolds-number flows, especially when the jets are heated.

In 2015, Mille [85] reported his development of a method for predicting a compressible turbulent jet flow based on an acoustic analogy of the cross-power spectral density in the near-field region of compressible fluid turbulence. In this method, equivalent sources are modelled with a single equation based on steady Reynolds-averaged Navier-Stokes (RANS) equations in relation to predictions of radiation intensity for the near-field and far-field across a wide range of jet Mach numbers and temperature ratios. The method is marred by difficulties related to the prediction of the near-field jet noise intensity, which could impact the accuracy of far-field predictions.

In 2008, Kumar and others [86] published an experimental investigation of axisymmetric jet pulse and steady jet characteristics for Mach numbers from 0.3 to 0.8 with respect to near-field noise. They found that, within the range of parameters studied, the sound pressure level was increased by about 32 dB compared to a steady jet flow at the same flow conditions. The noise measurements for their study were confined to a radial distance less than $10D_j$ from the jet centreline. A few years later, in 2012, Saxena and Morrisy [87] introduced a numerical study for predicting jet noise from single- and dual-stream of high subsonic flow. The researchers employed a parallel unsteady Reynolds-averaged Navier-Stokes (URANS) LES for

performing the turbulent flow simulation, using a modified detached eddy simulation (DES) for generating the turbulence flow. They also applied the Ffowcs Williams and Hawkings (FW-H) equation for measuring the noise spectra at observer locations.

At about the same time, in 2010, Lew and others [63] presented a numerical study for which they used both the LES method and the PowerFLOW commercial code based on the LBM kernel for predicting noise from an unheated turbulent axisymmetric jet. The far-field sound pressure levels were within 3 dB of other experimental results. This study actually provided motivation for the research presented in this thesis, which was conducted with the goals of overcoming the LBM limitations related to the simulation of high-subsonic jets and of applying aeroacoustics theory to an investigation of the sound propagated in far-field surroundings. In Lew and others [63] simulation, the flow intensities in the shear layer region were in poor agreement with the experimental results due to the laminar nature of the exiting boundary layer, since the Reynolds number was very low and the mesh grid insufficiently fine for solving this major problem.

A few years earlier, in 2005, Yu and Girimaji [88] had implemented LES in an LBM D3Q19 lattice model for a study of the near-field flow properties of a rectangular turbulent jet. Their research involved an investigation and explanation of the underlying flow physics without increases in the Mach numbers up to 0.1. It

should be noted that near- or far-field noise can be generated from a high-speed flow and turbulent perturbation. In aeroacoustics, to avoid a large simulation domain, it is useful to employ a hybrid approach that will lower simulation costs.

In 2010, Bres and others [89] developed two formulations of a far-field noise prediction code using the near-field values from LBM results as input to the acoustic analogy solver, based on the FW-H equation. They determined that the control surface around the noise source can be defined either as an impenetrable control surface for solid bodies or as a permeable surface for porous media and free-flow applications. Then, in 2014, Casalino and Lele [90] looked at coaxial jet noise generation using PowerFLOW commercial code to predict the far-field. In their work, they used the FW-H analogy, which is a far-field noise solver coupled with PowerFLOW applied to a fluid surface encompassing the plume. Some deficiencies in this simulation setup have been pointed out and include a premature turbulent breakdown in the shear layer. This failing is actually related to the mesh resolution and the turbulence model used in the simulation.

Several decades earlier, in 1988, Farassat and Myers [47] rederived the Kirchhoff equation using generalized derivatives for evaluating the solution around a subsonically moving surface when the observer is stationary. Their equation can be modified for a moving observer, and it will be used in this research as a hybrid approach with the CLBM models to predict the far-field noise from jets. LBM has

shown significant potential in fluid flow simulations, but performance issues have hindered wider applications due to the large amounts of memory required. In 2015, a parallel direct numerical simulation based on lattice Boltzmann was carried out on a multiple graphics processing unit (GPU) cluster. Developers Lei and others [91] used the single instruction multiple threads (SIMT) characteristics of the GPU cluster. The downside of employing SIMT execution is that thread-specific control flow is performed using masking, which leads to poor utilization when the threads of a processor follow different control-flow paths.

In 2015, Yusuke and Lien [92] developed a compute unified device architecture (CUDA) code for investigating the validity of LBM in GPU processing for turbulent flow simulations using LES. The GPU code was validated with respect to the assessment of a flow over a square cylinder confined in a channel. The researchers mentioned that two parallel GPUs accelerated the running time by 150X compared to a serial run on CPUs. A few years later, in 2018, Markesteijn and Karabasov [93] developed a GPU solver that would accelerate LES calculations for simulating subsonic coaxial jet noise at three different operation points. The GPU solver was combined with the penetrable integral surface formulation of the FW-H method. However, this GPU code was unable to capture low-frequency noise downstream because of the grid resolution beyond the nozzle exit.

8.3 Jet-flow development

When high-speed jet flow enters a quiescent ambient environment of the same fluid, a velocity shear layer is created between the entering and surrounding fluids, generating an envelope of high-speed flow. The envelope containing the turbulence caused by the jet adopts a nearly conical shape. An investigation of the jet development, the velocity profiles, and the turbulence intensity of a three-dimensional compressible turbulent jet is described in this section. Velocity, pressure, and density distribution are the major flow properties required for predicting near- and far-field noise.

Table 8.1: Free circular jet characteristics

Test case characteristics	
Jet diameter	$D_j = 0.0508\, m$
Jet exit velocity	$U_j = 130{,}170{,},205\ and\ 256\, m/s$
Kinematic viscosity	$\nu = 1.516 * 10^{-5}\ m^2/s$
Reynolds number	$R_{eD} = \frac{U_j D_j}{\nu_j} = 4.35 * 10^5, 5.7 * 10^5, 6.87 * 10^5\ and\ 8.6 * 10^5$
Mach number	$M_j = U_j/c = 0.4, 0.5, 0.6, 0.75$
Simulation dimension (LBM) LBM grid sizing unit =1	$D_{lbm} = 18\ units$ $N_x = 120D_{lbm}\ , N_y = 16D_{lbm}, N_z = 16D_{lbm}$ Total number of grid points # $180 * 10^6$,
Δx=0.0020833 $\Delta y = 0.00127$ $\Delta z = 0.00127$	LBM (Δx_{lbm}=Δy_{lbm}=Δz_{lbm} =1) $\Delta t_{lbm} = 1$
$CFL = \frac{u\Delta t}{\Delta x} = \frac{1}{\sqrt{3}}$ M_j =0.23, 0.288, 0.34, and 0.433	time step $\Delta t = CFL\frac{\Delta x}{U_j} = 0.5 * 10^{-5}$
Total time steps	44000

Experimental and numerical observations of the mean turbulent velocity of the jet field show that, in the axial direction of the jet, the axial jet flow can be divided into two main distinct regions. The first region is close to the jet exit ($x = 0$ to $x =$

$5D_j$), where the axial velocity is almost constant and equal to the jet exit velocity U_j, and the turbulence penetrates inward toward the axis or centerline of the jet. As shown in Figure 8.1 and Figures 8.2 (a)-8.2 (b), a wedge-like region of undiminished mean velocity is apparent. This region is commonly known as the flow development region, or potential core region.

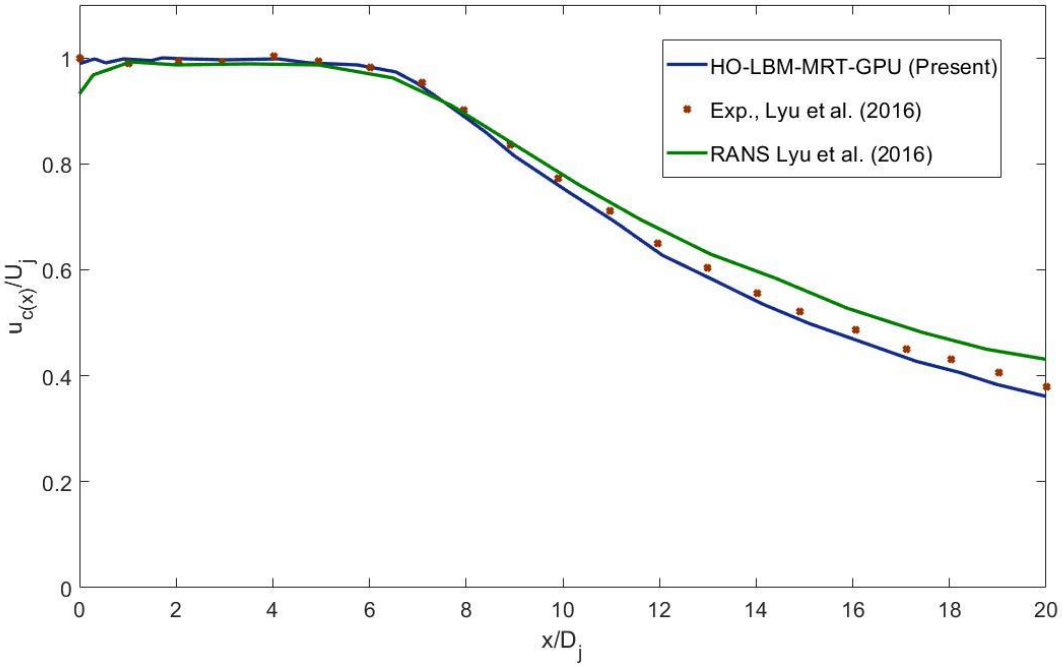

Figure 8.1: Mean streamwise velocity decay along the jet centerline axis, M_j = 0.5.

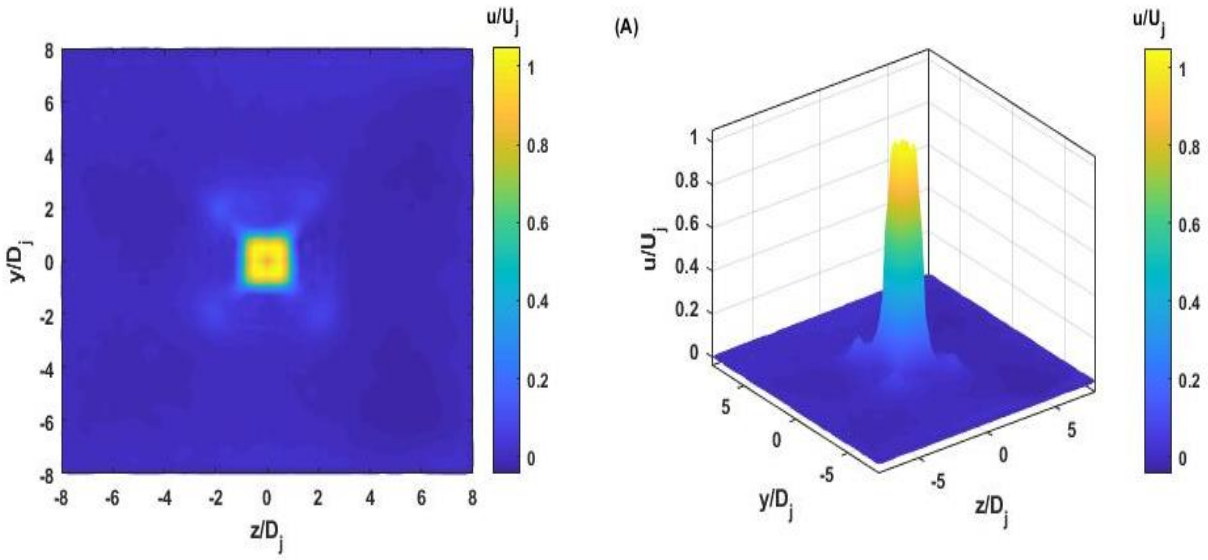

Figure 8.2 (a): Mean axial velocity at the jet exit, x = 0, M_j = 0.5.

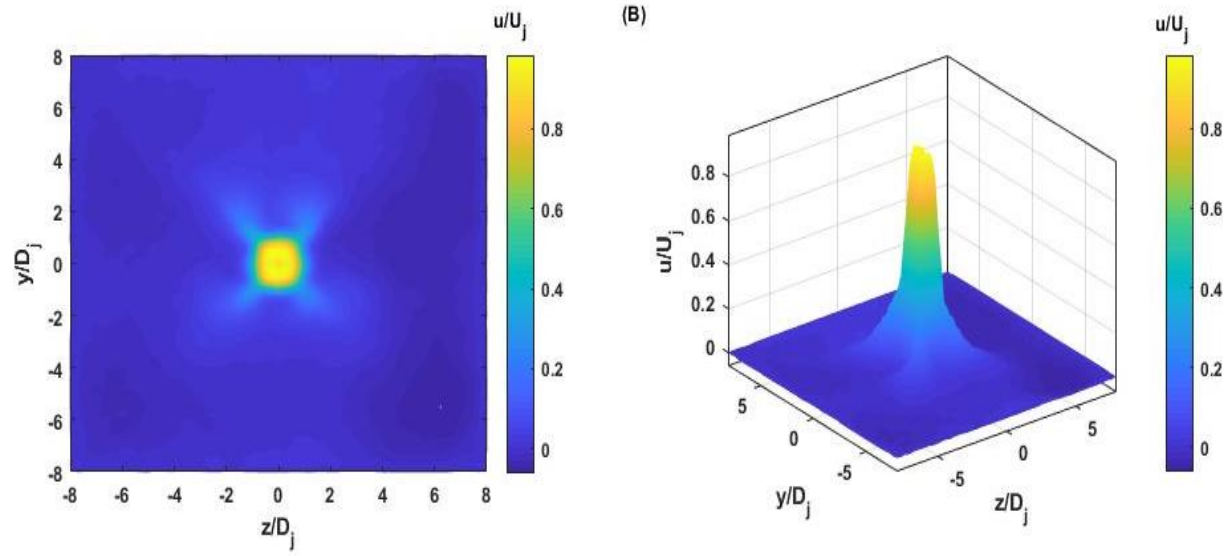

Figure 8.2 (b): Mean axial velocity at, $x = 5D_j$, M_j = 0.5.

The second region is known as the fully developed flow region from X = 5D to x = 20D. Here, the turbulence has penetrated to the jet axis flow, so the potential core has disappeared and the axial velocity profile of the jet has changed from a semi-uniform one to one with a turbulent velocity. This shift indicates a more

flattened profile than the parabolic profile in a laminar flow, as illustrated in Figures 8.1, 8.2 (c), and 8.2 (d). As a result, the potential core has disappeared, and a new flow region has been generated in which the flow is fully developed.

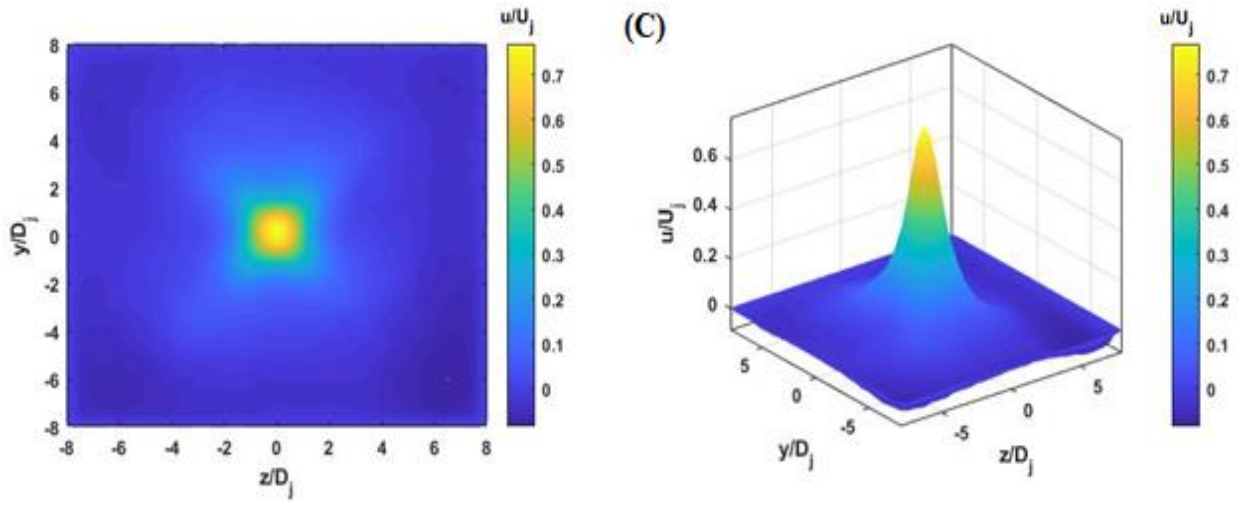

Figure 8.2 (c): Mean axial velocity at, $x = 10D_j$, M_j = 0.5.

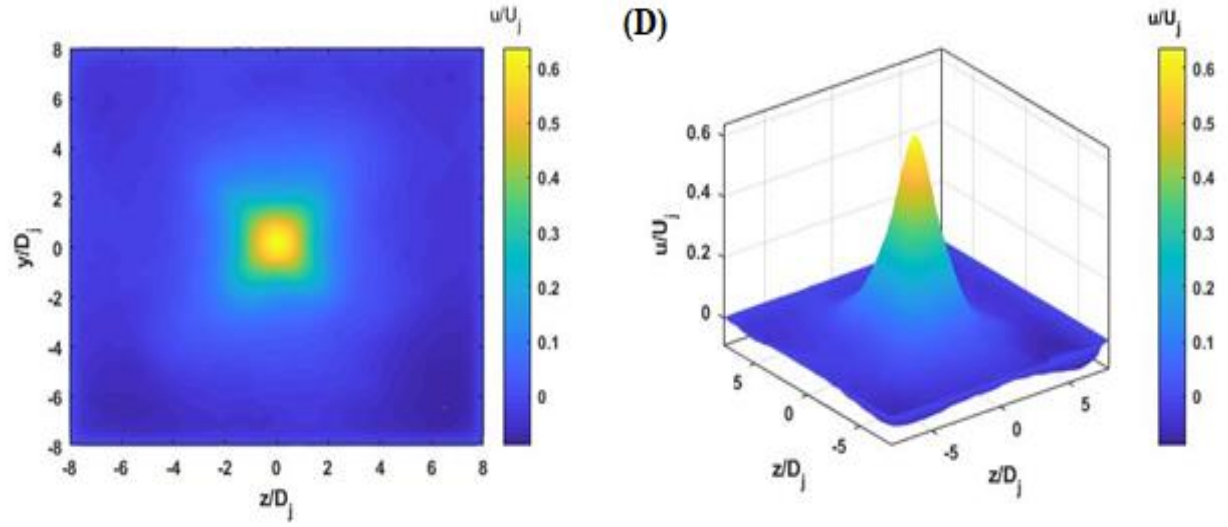

Figure 8.2 (d): Mean axial velocity at, $x = 13D_j$, M_j = 0.5.

After the axial distance $x > 10D_j$, the shear layer grows downstream with increasing $x/D_j$and more flow entering the stream from the surrounding regions, thus decreasing the velocity of the jet. As shown in Figure 8.2 (e), the velocity profile has expanded in the radial direction up to $4D_j$. As well, the three-dimensional surface velocity profile indicates that the velocity cone has become thicker and the time-average velocity has been reduced to $0.5U_j$.

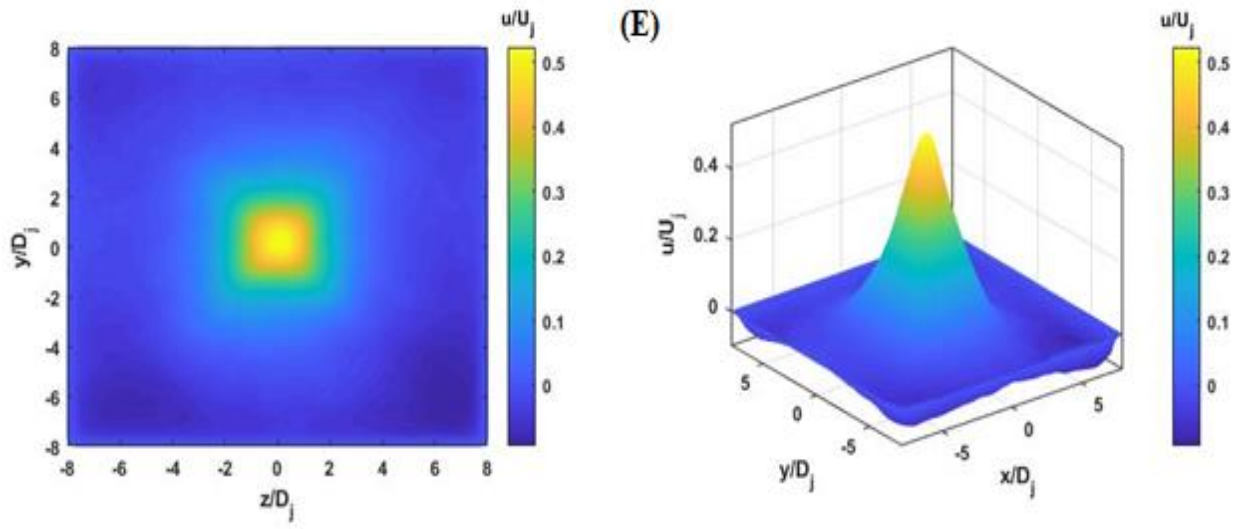

Figure 8.2 (e): Mean axial velocity at, $x = 16D_j$, M_j = 0.5.

The simulation results for the investigation of jets penetrating the same quiescent fluid (Figure 8.2) consistently reveal that the envelope containing the turbulence caused by the jet adopts a nearly conical shape. In other words, the jet flow cone radius R is proportional to the distance x downstream from the discharge

location, as shown in the three-dimensional velocity surface profile in Figures 8.2 (a) to 8.2 (f).

At the end of the simulation domain in the axial direction, $x = 20D_j$ in Figure 8.2 (f), the velocity has lost its high entrance value and has begun a gradual decrease. The surrounding regions and the streaming-generated shear layer in the contact area lose the high energy of the flow, thus reducing the velocity of the jet flow at the end. As a consequence, the velocity profile flattens to a value of $0.4U_j$ and a cone-diameter of $8D_j$.

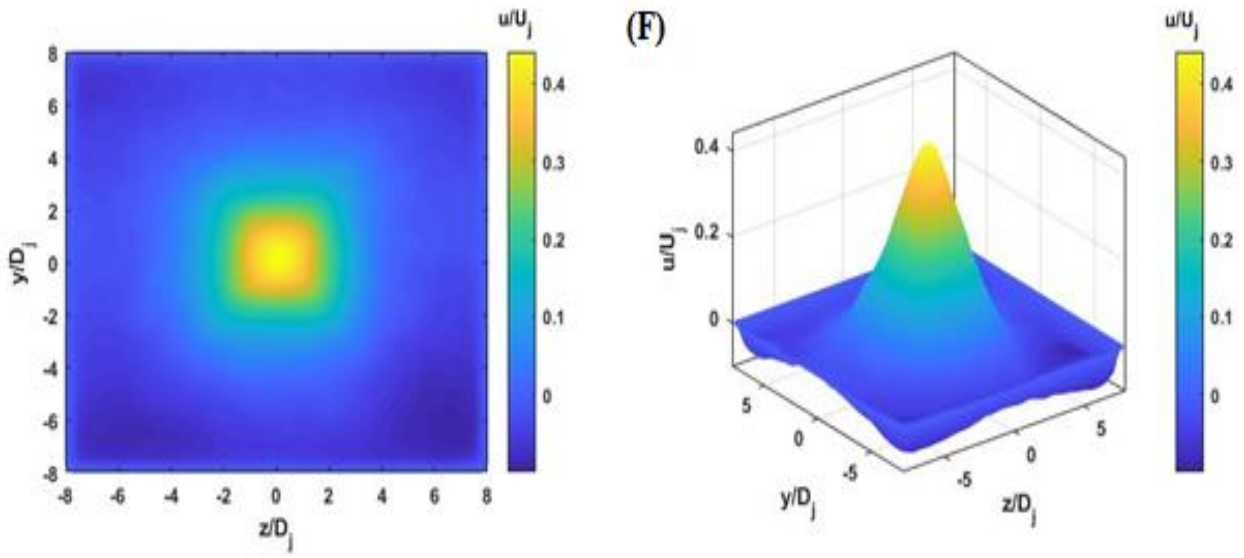

Figure 8.2 (f): Mean axial velocity at, $x = 20D_j$, M_j = 0.5.

Studying the turbulence is essential for an understanding of the mixing processes and noise-generating mechanisms. In free jet flow, the high turbulence intensity and shear stress occur in the outer mixing region, where the free jet interacts

with the surrounding quiescent air. Consideration of this area is very important for predicting free far-field jet noise and for identifying where the control surface should be placed.

Figure 8.3 illustrates the turbulence intensity of the jet along the centreline. The turbulence intensity increases beyond the jet exit due to the merging of the jet layers until it reaches its maximum at $x = 11D_j$, before decaying downstream, at which point the axial velocity gradually declines. Because of using initial perturbation at the jet exit simulation, the turbulence intensity near to the jet exit does not follow the experimental results and shown higher than Lyu's results.

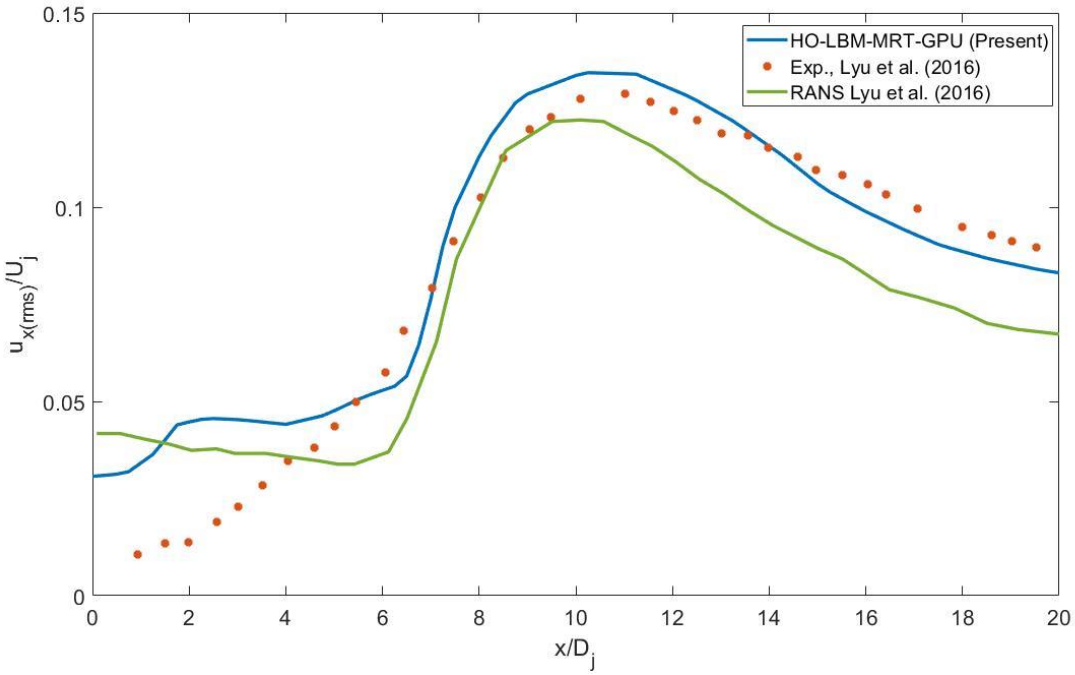

Figure 8.3: Mean jet turbulence intensity along the centerline, M_j = 0.5.

The turbulence intensity decays more slowly than with RANS and faster than in the experimental data from Lyu [94]. The high turbulence intensity values at the peak with LBM could be due to the use of different governing equations or to differences in the shape of the jet exit; they might also be caused by the application of different numerical methods, all of which can affect the results. Studying the jet-flow development and the turbulence structure is essential for an understanding of the mixing processes and the noise-generating mechanisms. Once this understanding has been acquired, near-field jet noise can be easily predicted, as explained in the next section.

8.4 Near-field jet noise

The overall sound pressure levels obtained at a radial distance $r = 7.5D_j$ parallel to the centerline of the jet from $x = 0$ to $x = 20D_j$ are plotted in Figure 8.4 for Mach number $M = 0.6$ and Reynolds number $R_{eD_j} = 5 * 10^5$. The LBM results compare very well with the Barré [95] experimental data (dotted line) and show good agreement with the structure of the jet flow. The overall sound pressure begins to increase beyond the potential core of the jet, $x = 5D_j$, where the stream exhibits the highest shear flow with the surrounding air. This increase elevates the turbulent perturbation in the interaction region ($x = 6D_j$- $x = 15D_j$). Compared to conditions

at the jet exit after $x > 15D_j$, the jet noise starts to decrease when the velocity gradually becomes evanescent.

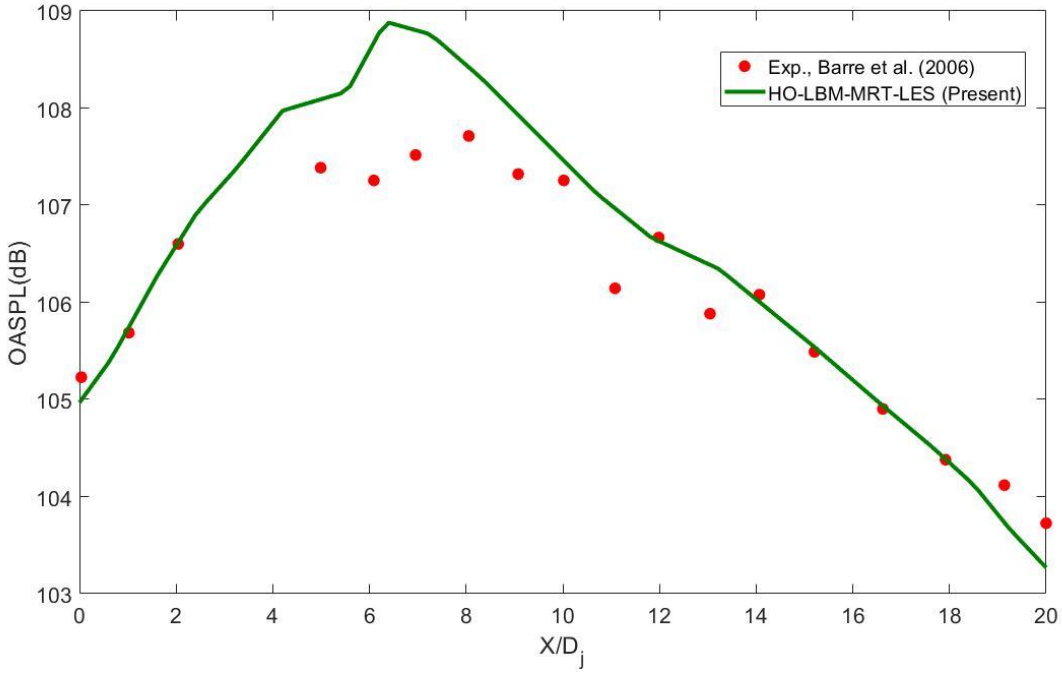

Figure 8.4: Overall sound pressure levels obtained along the horizontal line $\mathrm{r} = 7.5\mathrm{D_j}$ for the subsonic jet at a Mach number of $M_j = 0.6$

The sound pressure fluctuation spectra of near-field jet noise were investigated as functions of the Strouhal number $0.05 < St < 6.4$ along the horizontal line $r = 7.5D_j$ from the centerline of the jet at the axial locations $x = 0, 5D_j,\ x = 10D_j, x = 15D_j$, and $x = 20D_j$. These are depicted in Figure 8.5. The radiation patterns compare well overall with experimental data provided by, for example, Barré [95].

In Figure 8.5 (a), the sound pressure spectrum is shown at point $x = 0$ and $r = 7.5$ at the side of the potential core region in the radial direction. At $x = 0$, the sound pressure begins to rise with increases in the Strouhal number until a peak of 101 dB/St is reached, when the Strouhal number is about 0.5. At that point, the sound spectra slow down to 91dB/St at a Strouhal number of 6.4. At $x = 5D_j$, as shown in Figure 8.5 (b), the pressure spectra slow their decrease from 104 dB/St at $St = 0.2$ and then start to increase until reaching a peak at $St = 0.6$, when the pressure spectra decrease slightly again, to 94 dB/St at $St = 4.6$. The sound pressure spectra are affected mainly by the destiny spectra and the velocity fluctuation, which is the source of the sound generated by fluctuations in the turbulence [96].

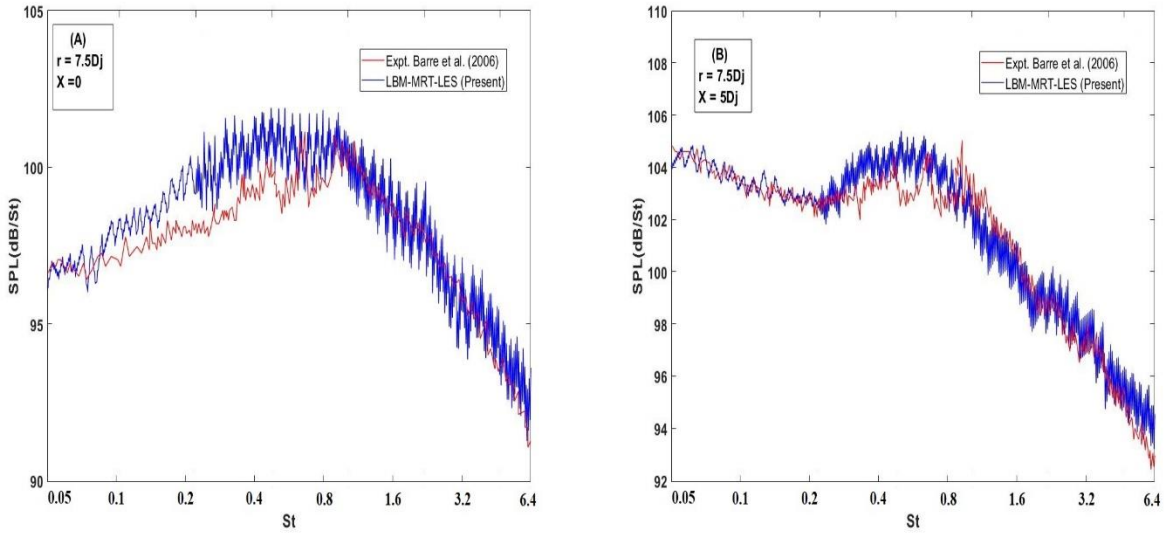

Figure 8.5: Sound pressure spectra at Mach number $M_j = 0.6$ at (a) $x = 0$, $r = 7.5D_j$ and (b) $x = 5D_j$, $r = 7.5D_j$

Figures 8.5 (b), 8.5 (c), and 8.5 (d) identify the study points located outside the fully developed region but on the same side. The fluctuations in turbulence in the interaction between the streamflow and the surrounding quiescent air generate the peak sound pressure. The simulation results show that the sound pressure spectra decrease slightly with increasing Strouhal numbers. In general, at the same radial distance as the axial distance increases, the sound pressure spectra levels are higher, whereas the sound spectra decrease with higher Strouhal numbers at the same position in the simulation domain.

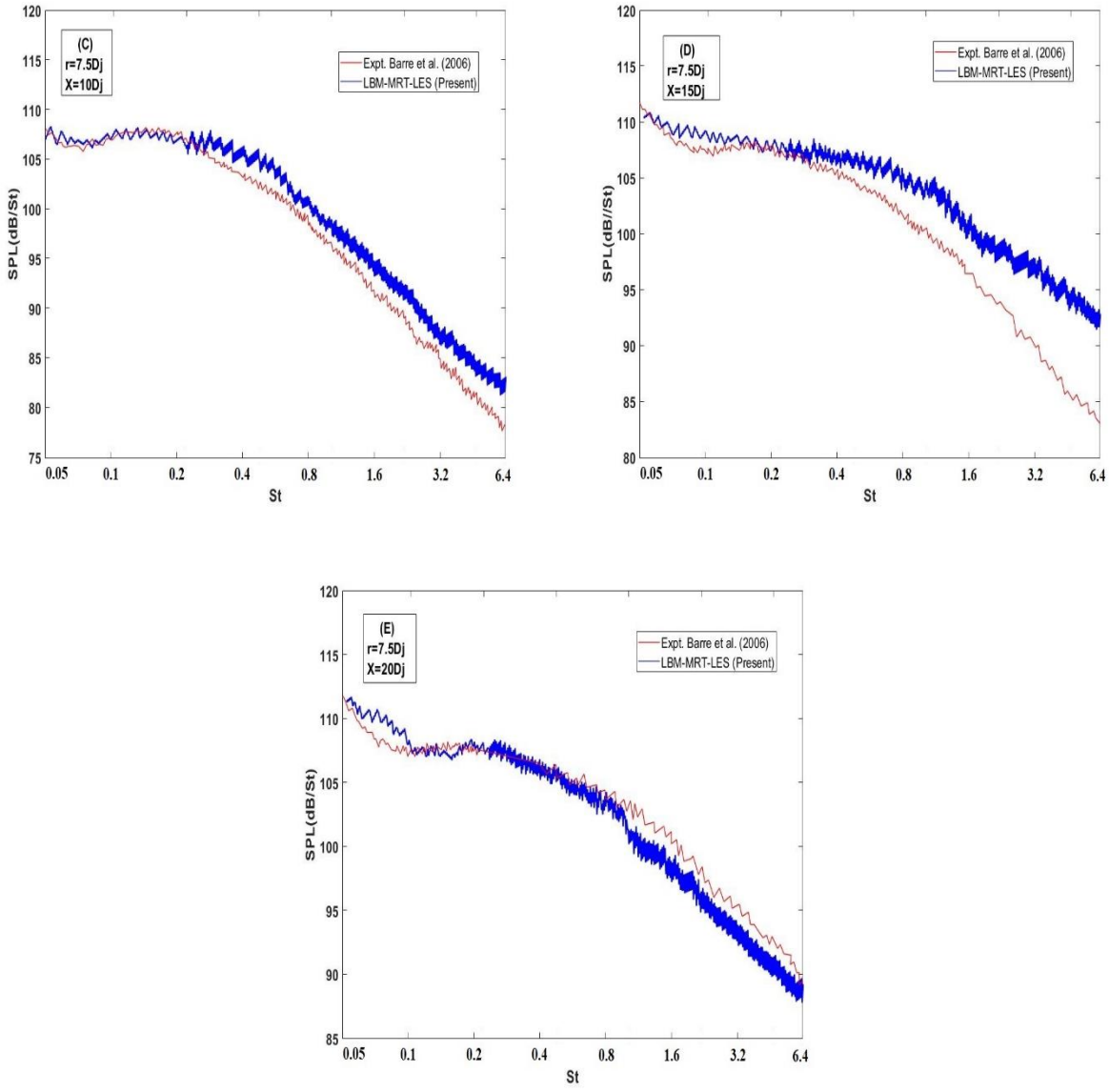

Figure 8.6: Sound pressure spectra at Mach number $M_j = 0.6$ obtained at $r = 7.5D_j$ at (c) $x = 10D_j$, (d) $x = 15D_j$, and (e) $x = 20D_j$.

8.5 Far-field jet noise

The numerical prediction of far-field jet noise has received significantly more attention during the past few decades. One of the main reasons for the increase in research interest is that numerical simulations have become faster due to high-

performance computing and the use of parallel computing for the simultaneous processing of simulation codes. For the work presented here, the LBM code was applied in a CUDA parallel computing platform in the Graham-SHARCNET supercomputer system. After the near-field noise prediction had been obtained as set out in section 8.4, the Kirchhoff surface integral method could be applied for predicting the far-field jet noise.

The correct placement of the Kirchhoff surface around the jet is essential for accurate predictions. The first step was to generate the control surface around the jet at radial direction $5D_j$ because the velocity becomes negligible near a radial distance of $5D_j$. As a case study in experimental research, the far-field noise was predicted for an observer located at arc $52D_j$ from the jet exit center and at a range of angles from θ = 15 to θ = 90.

Figure 8.7 presents the overall sound pressure levels evaluated in the far-field for two Mach numbers, $M_j = 0.5$ and $M_j = 0.75$, as functions of the polar angle measured to the jet axis. According to the characteristics of the experimental study, the jet sound pressure level is radiated predominantly in the downstream direction and reaches a peak at angles of θ = 20 to θ = 30. At Mach number 0.6, the sound pressure levels decrease slightly for the peak at an angle θ = 30, which compares well with the experimental data, with overpredictions of 1dB, which denotes excellence in aeroacoustics studies. The prediction results for Mach number 0.75

show a peak sound pressure between $\theta = 30$ and $\theta = 40$, but $\theta = 25$ in the experimental results, with an overprediction of about 3dB, which is acceptable. The LBM overpredicts at high Mach numbers due to the LBM limitations related to solving high Mach number flows.

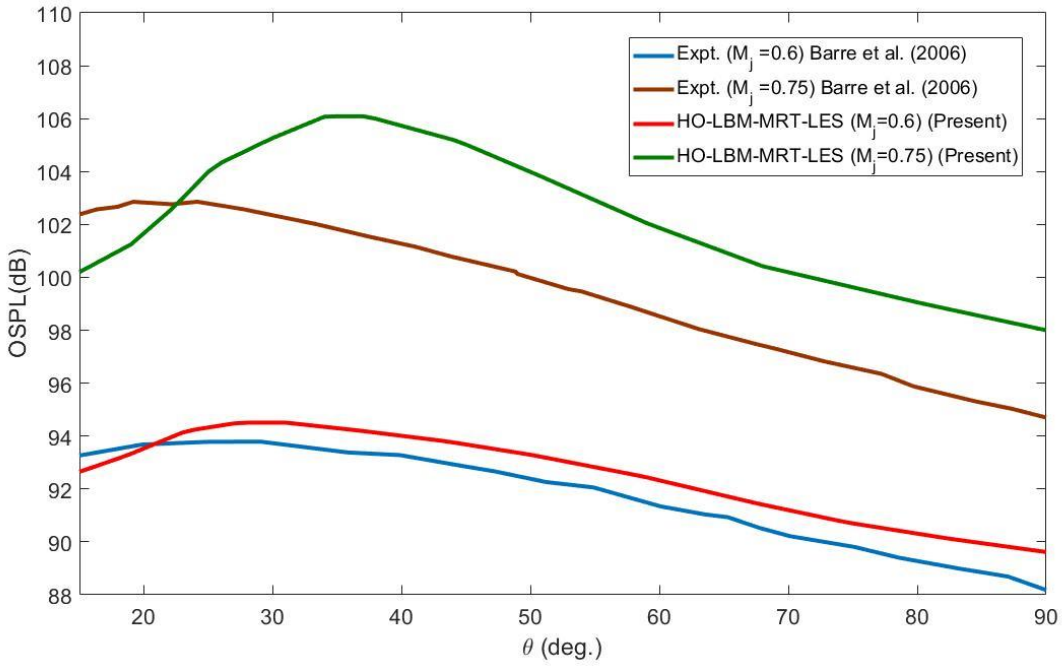

Figure 8.7: Overall sound pressure levels for jets at Mach numbers $M_j = 0.6$ and $M_j = 0.75$ obtained at a radial distance of $52D_j$ from the jet exit.

The results of the investigation of the far-field sound spectra for a subsonic jet with $M_j = 0.6$ are set out in Figure 8.8 as a function of the Strouhal numbers at $\theta = 25°$, $\theta = 40$ and $\theta = 60°$, with peaks that are collapsed using appropriate level scaling similar to the scales employed in the experimental studies. The LBM-Kirchhoff predictions are slightly higher than Barré's [95] experiment results, but with acceptable deviations: the worst case is 3dB higher. The amplitude of the sound

pressure spectrum appears higher than the experimental data due to the high frequency produced by the kinetic energy in the shear layer region. Some variations in the sound radiation angles between the experimental results and the LBM-Kirchhoff numerical predictions are due to the use of different measurement techniques for the sound radiation angle and the sound source distributions.

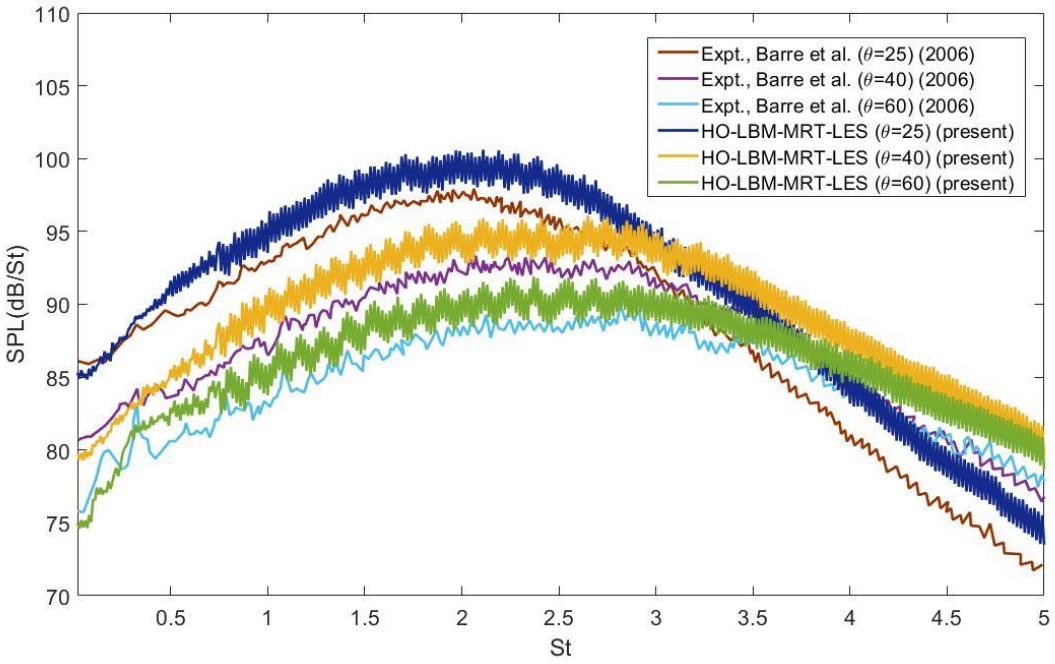

Figure 8.8: Sound pressure spectra levels for a jet at a Mach number of $M_j = 0.6$ obtained at a radial distance $52D_j$ from the jet exit.

8.6 Summary

The numerical simulation of a subsonic jet at Mach 0.5 and 0.75 was performed using LBM in combination with Kirchhoff's surface integral method. The

LES was implemented in LBM with multiple relaxation times (MRT) to simulate a highly turbulent flow using CUDA programming in a Graham heterogeneous cluster. The results show that the jet simulation was in good agreement with the experimental data and with the jet characteristics theory published in the literature. The mean axial velocity and the turbulence intensity were in good agreement with the results of Lyu's [94] recent numerical experiments. The overall sound pressure level (integrate SPL over all resolved frequencies) along a line parallel to the jet axis at a radial distance $r = 7.5D_j$ agrees reasonably well with Barré's experimental findings.

The sound spectra in the near-field were also studied at five different points in the domain. Here as well, the results were in very good agreement with other experimental findings but with higher and lower predictions at some frequencies. In the far-field jet noise predicted using the Kirchhoff method at an observer distance $r = 52D_j$, the centerline of the jet was compared with the Barré [95] experiment at $M_j = 0.6$. At a high subsonic value of $M_j = 0.75$ the results were overpredicted due to the LBM limitation with respect to solving high Mach number flows.

A powerful CFD tool for simulating most kinds of fluid flows, LBM can be merged with other CFD methods such as LED. High-performance computing is required for the in-depth study of three-dimensional flows. When MRT is used in

3D LBM models, the code run time becomes a critical aspect of the research, especially for large simulation domains. LBM implementation on a GPU is therefore beneficial and reduces the time by 120X compared to employing a CPU.

Chapter 9

Conclusion and Future Work

9.1 Conclusion

The lattice Boltzmann method (LBM) is a powerful numerical method that is fast increasing in popularity and has also become serious competition for traditional computational fluid dynamics methods such as finite difference, finite element, and finite volume. LBM is based on the kinetic theory method, in which the behaviour of a system is described at the kinetic level through the lattice Boltzmann discrete equation. This technique means that the method offers numerous advantages and also enables the efficient and accurate modelling of complex multi-physics phenomena [97].

LBM originated from the lattice gas automata (LGA) and operates based on distribution functions in space and time, which requires velocity space discretization. A limitation has been associated with solving high Mach number flows when using low-order Maxwell distribution functions in a polynomial form. In the research conducted for this thesis, this limitation has been overcome through the use of a high-order equilibrium distribution function along with an alternative equilibrium function introduced by Kataoka and Tsutahara [1]. Subsonic flows have been solved for different models under a number of boundary conditions. Simulated turbulent

subsonic jet flows provided excellent test cases for studying the ability of the LBM to solve high Mach number flows, which encouraged the use of the properties of the resulting near-field flows for the study of far-field jet aeroacoustics.

This research also involved the development of an in-house compressible LBM code in conjunction with large-eddy simulation (LES) and the Kirchhoff surface integral method as a means of predicting turbulent jet noise in the far-field. When the Kirchhoff surface integral approach is applied, the correct placement of the control surface around the jet is essential for accurate predictions. In addition, it might be difficult or even impossible to enclose all nonlinearities in the axial direction. That is, the control surface end might cut off some of the noise-producing portions of the downstream flow. To ensure that all nonlinearities are captured, the control surface end in the axial direction can be moved farther downstream, but then the study domain becomes so large that more memory might be needed for the computer to run the simulation code.

According to the results obtained, combining LBM with Kirchhoff's surface method produces a reasonable numerical technique, which gives highly accurate results compared to the corresponding experimental data available in the literature. A final component of the research was the implementation of the LBM-LES code on the CUDA program and its execution on graphics processing units (GPUs) in

order to further enhance its computational efficiency, particularly for 3D calculations.

9.2 Future Work

The findings from this research point to several directions in which the newly developed methods can be further extended and applied. Recommendations for future work include the following:

- Extend the D3Q19 lattice model to the D3Q27 lattice model using a higher-order equilibrium distribution function in a GPU, which can increase accuracy and enhance the simulation results.
- Simulate supersonic jet flows by using another alternative equilibrium distribution function, such as the circular distribution function, which is a probability distribution function on a unit circle. This technique would be simple to integrate into the particle velocity space and could be used for simulations involving high Mach numbers [29].
- Implement another hybrid acoustics approach such as that of Ffowcs Williams and Hawkings (FW-H) in LBM for solving rotor applications such as fan turbines. This work would require a surface and a volume integral, but it often produces good solutions through the use of the surface integral part in the equation alone [98], [99].

- Extend the C++ CUDA code capabilities to enable the use of GPUs on multiple compute nodes in a parallel computing process in the GPUs, which allows hundreds of GPUs to be employed in parallel.

References

[1] T. Kataoka and M. Tsutahara, "Lattice Boltzmann method for the compressible Euler equations," Physical Review E, vol. 69, no. 5, pp. 056702-1 -056702-14, 2004.

[2] T. Kataoka and M. Tsutahara, "Lattice Boltzmann model for the compressible Navier-Stokes equations with flexible specific-heat ratio," Physical Review, vol. 69, no. 3, pp. 035701-1 -035701-4, 2004.

[3] D. A. Perumal and A. K. Dass, "A Review on the development of lattice Boltzmann computation of macro fluid flows and heat transfer," Alexandria Engineering Journal, vol. 54, no. 4, pp. 955-971, 2015.

[4] K. Mattila, Implementation techniques for the lattice Boltzmann method, University of Jyväskylä, 2010.

[5] J. Tu, G. H. Yeoh and C. Liu, Computational fluid dynamics: a practical approach, Oxford: Butterworth-Heinemann, 2018.

[6] Y. He, Q. Li, Y. Wang and G. Tang, "Lattice Boltzmann method and its applications in engineering thermophysics," Chinese Science Bulletin, vol. 54, no. 22, pp. 4117-4134, 2009.

[7] Y. B. Bao and J. Meskas, "Lattice Boltzmann Method for Fluid Simulations," 2011.

[8] W. Feng, B. He, A. Song, Y. Wang, M. Zhang and W. Zhang, "Compressible Lattice Boltzmann Method and Applications," International

Journal of Numerical Analysis and Modeling, vol. 9, no. 2, p. 410–418, 2012.

[9] S. R. Rao, R. Deshmukh and S. Kotnala, "A Lattice Boltzmann Relaxation Scheme for Inviscid Compressible Flows," Bangalore, 2015.

[10] V. Malyshkin, Parallel computing technologies, 10, Ed., Berlin: Springer-Verlag Berlin and Heidelberg GmbH & Co. K, 2009.

[11] X. Shan and X. He, "Discretization of the velocity space in the solution of the Boltzmann equation," Physical Review Letters, vol. 80, no. 1, pp. 65-68, 1 1998.

[12] T. Krüger, H. Kusumaatmaja, A. Kuzmin, O. Shardt, G. Silva and E. M. Viggen, The lattice Boltzmann method: principles and practice, Cham: Springer International Publishing, 2017.

[13] Z. Guo and C. Shu, Lattice Boltzmann Method and Its Applications in Engineering, Singapore: World Scientific, 2013.

[14] Y.-T. Yang, S.-C. Chang and C.-S. Chiou, "Lattice Boltzmann method and large-eddy simulation for turbulent impinging jet cooling," International Journal of Heat and Mass Transfer, vol. 61, pp. 543-553, 2013.

[15] C. Cercignani, The Boltzmann equation and its applications, New York: Springer-Verlag, 1988.

[16] P. L. Bhatnagar, E. P. Gross and M. Krook, "A Model for Collision Processes in Gases. I. Small Amplitude Processes in Charged and Neutral

One-Component Systems," Physical Review, vol. 94, no. 3, pp. 511-525, 1954.

[17] D. Oztekin, "The Lattice Boltzmann Methods and Their Applications to Fluid Flows," 2014.

[18] A. A. Mohamad, Lattice boltzmann method: Fundamentals and engineering applications with computer codes, London: Springer London, 2011.

[19] A. N. Gorban and D. J. Packwood, "Enhancement of the stability of lattice Boltzmann methods by dissipation control," Physica A: Statistical Mechanics and its Applications, vol. 414, pp. 285-299, 11 2014.

[20] F. Higuera, "Boltzmann approach to lattice gas simulations," Europhysics Letters (EPL), vol. 9, no. 7, pp. 663-668, 8 1989.

[21] D. d'Humières, P. Lallemand and U. Frisch, "Lattice gas models for 3D Hydrodynamics," Europhysics Letters (EPL), vol. 2, no. 4, pp. 291-297, 8 1986.

[22] Y. H. Qian, D. D'Humières and P. Lallemand, "Lattice BGK models for Navier-Stokes equation," Europhysics Letters (EPL), vol. 17, no. 6, pp. 479-484, 2 1992.

[23] D. Dhumières, "Multiple–relaxation–time lattice Boltzmann models in three dimensions," Philosophical Transactions of the Royal Society of London. Series A: Mathematical, Physical and Engineering Sciences, vol. 360, no. 1792, pp. 437-451, 2002.

[24] H. Hamedi and M. Rahimian, "Numerical Simulation of Non-Newtonian Pseudo-Plastic Fluid in a Micro-Channel Using the Lattice Boltzmann Method," World Journal of Mechanics, vol. 05, no. 01, pp. 231-242, 2011.

[25] Q. Zou and X. He, "On pressure and velocity boundary conditions for the lattice Boltzmann BGK model," Physics of Fluids, vol. 9, no. 6, pp. 1591-1598, 1997.

[26] H. Shouxin, Y. Guangwu and S. Weiping, "A lattice boltzmann model for compressible perfect gas," Acta Mechanica Sinica, vol. 13, no. 3, pp. 218-226, 1997.

[27] X. Shan and X. He, "Discretization of the Velocity Space in the Solution of the Boltzmann Equation," Physical Review , vol. 80, no. 1, pp. 65-68, 1998.

[28] Y. Guangwu, C. Yaosong and H. Shouxin, "Simple lattice Boltzmann model for simulating flows with shock wave," Physical Review E, vol. 59, no. 1, pp. 454-459, 1999.

[29] K. Qu, C. Shu and Y. T. Chew, "Alternative method to construct equilibrium distribution functions in lattice-Boltzmann method simulation of inviscid compressible flows at high Mach number," Physical Review E, vol. 75, no. 3, pp. 036706 (1-13), 2007.

[30] X. Shan and X. He, "Discretization of the Velocity Space in the Solution of the Boltzmann Equation," Physical Review Letters, vol. 80, no. 1, pp. 65-68, 1998.

[31] J. Smagorinsky, "General Circulation Experiments With The Primitive Equations," Meteorologische Zeitschrift, vol. 91, no. 3, pp. 99-164, 1963.

[32] Q. Li, C. Zhong, K. Li, G. Zhang, X. Lu, Q. Zhang, K. Zhao and X. Chu, "Implementation of a Lattice Boltzmann Method for Large Eddy Simulation on Multiple GPUs," in 2012 IEEE 14th International Conference on High Performance Computing and Communication & 2012 IEEE 9th International Conference on Embedded Software and Systems, Liverpool, 2012.

[33] S. Hou, J. Sterling, S. Chen and G. Doolen, "A lattice Boltzmann subgrid model for high Reynolds number flows," vol. 6, pp. 151-166, 1994.

[34] J. Bridges and M. Wernet, "Measurements of Aeroacoustic Sound Sources in Turbulent Jets," in 9th AIAA/CEAS Aeroacoustics Conference and Exhibit, Hilton, 2003.

[35] H. Yu, L.-S. Luo and S. S. Girimaji, "LES of turbulent square jet flow using an MRT lattice Boltzmann model," Computers & Fluids, vol. 35, no. 8, pp. 957-965, 2006.

[36] L. M. Dale, M. Debia, O. C. Mudaheranwa, C. Plante and A. Smargiassi, "An Exploration of Transportation Source Contribution to Noise Levels Near an Airport," Environment and Pollution, vol. 3, no. 1, pp. 73-81, 2013.

[37] S. Marburg and B. Nolte, Computational acoustics of noise propagation in fluids: finite and boundary element methods, Berlin: Springer, 2008.

[38] B. Gracey, "Sound pressure level - definitions, terms, units, measurement: Acoustic glossary," London.

[39] M. J. Lighthill, "On sound generated aerodynamically II. Turbulence as a source of sound," Proceedings of the Royal Society of London. Series A. Mathematical and Physical Sciences, vol. A211, pp. 564-587, 1952.

[40] M. J. Lighthill , "On sound generated aerodynamically, II: Turbulence as a source of sound," Proceedings of the Royal Society of London. Series A. Mathematical and Physical Sciences, vol. A222, pp. 1-32, 1954.

[41] S. A. L. Glegg and W. J. Devenport, Aeroacoustics of low Mach number flows: fundamentals, analysis, and measurement, London: Academic Press, 2017.

[42] J. E. Williams and D. L. Hawkings, "Sound Generation by Turbulence and Surfaces in Arbitrary Motion," Philosophical Transactions of the Royal Society A: Mathematical, Physical and Engineering Sciences, vol. 264, no. 1151, pp. 321-342, 1969.

[43] D. G. Crighton, Modern methods in analytical acoustics: lecture notes, London: Springer, 1992.

[44] K. S. Brentner and F. Farassat, "Analytical comparison of the acoustic analogy and Kirchhoff formulation for moving surfaces," AIAA Journal, vol. 36, pp. 1379-1386, 1998.

[45] G. Kirchhoff, "Zur Theorie der Lichtstrahlen," Annalen der Physik, vol. 254, no. 4, pp. 663-695, 1883.

[46] W. R. Morgans, "XIV.The kirchhoff formula extended to a moving surface," The London, Edinburgh, and Dublin Philosophical Magazine and Journal of Science, vol. 9, no. 55, pp. 141-161, 1930.

[47] F. Farassat and M. K. Myers, "Extension of Kirchhoffs formula to radiation from moving surfaces," Journal of Sound and Vibration, vol. 123, no. 3, pp. 451-460, 1988.

[48] N. Andersson, L.-E. Eriksson and L. Davidson, "LES Prediction of Flow and Acoustic Field of a Coaxial Jet," in 11th AIAA/CEAS Aeroacoustics Conference, Goteborg, 2005.

[49] L. Morino, B. K. Bharadvaj, M. I. Freedman and K. Tseng, "Boundary integral equation for wave equation with moving boundary and applications to compressible potential aerodynamics of airplanes and helicopters," Computational Mechanics, vol. 4, pp. 267-277, 1989.

[50] L. Morino and R. Piva, Computational methods in potential aerodynamics, Roma: Springer, 1990.

[51] A. S. Lyrintzis and R. Mankbadi, "Prediction of the far-field jet noise using Kirchhoffs formulation," AIAA Journal, vol. 34, no. 2, pp. 413-416, 1996.

[52] F. L. Pan, A. Uzun and A. S. Lyrintzis, "Surface Integral Methods in Jet Aeroacoustics: Refraction Corrections," JOURNAL OF AIRCRAFT, vol. 45, no. 2, pp. 381-387, 2008.

[53] A. Dieter and Wolf-Gladrow, Lattice-gas cellular automata and lattice Boltzmann models: An introduction, Berlin: Springer-Verlag Berlin and Heidelberg GmbH & Co. K, 2002.

[54] A. Ghasemi, V. Roussinova, R. Balachandar and R. Barron, "Reynolds number effects in the near-field of a turbulent square jet," Experimental Thermal and Fluid Science, vol. 61, pp. 249-258, 2 2015.

[55] S. Chen, "A large-eddy-based lattice Boltzmann model for turbulent flow simulation," Applied mathematics and computation, vol. 215, no. 2, pp. 591-598, 2009.

[56] X. Jiang and C.-H. Lai, Numerical techniques for direct and large-eddy simulations, Raton: CRC Press, 2009.

[57] M. Fernandino, K. Beronov and T. Ytrehus, "Large eddy simulation of turbulent open duct flow using a lattice Boltzmann approach," Mathematics and Computers in Simulation, vol. 79, no. 5, pp. 1520-1526, 2009.

[58] Y.-H. Dong, P. Sagaut and S. Marie, "Inertial consistent subgrid model for large-eddy simulation based on the lattice Boltzmann method," Physics of Fluids, vol. 20, no. 3, pp. 035104-01-035104-12, 2008.

[59] Y.-H. Dong and P. Sagaut, "A study of time correlations in lattice Boltzmann-based large-eddy simulation of isotropic turbulence," Physics of Fluids, vol. 20, no. 3, pp. 035105(1-11), 2008.

[60] S. Chen, "A large-eddy-based lattice Boltzmann model for turbulent flow simulation," Applied Mathematics and Computation, vol. 215, no. 2, pp. 591-598, 2009.

[61] H. Si and Y. Shi, "Study on lattice Boltzmann method/large eddy simulation and its application at high Reynolds number flow," Advances in Mechanical Engineering, vol. 7, no. 3, pp. 1-8, 2015.

[62] J. M. Buick, C. A. Greated and D. B. Campbell, "Lattice BGK simulation of sound waves," Europhysics Letters (EPL), vol. 43, no. 3, pp. 235-240, 1998.

[63] P. T. Lew, L. Mongeau and A. Lyrintzis, "Noise prediction of a subsonic turbulent round jet using the lattice-Boltzmann method," The Journal of the Acoustical Society of America, vol. 128, no. 3, pp. 11-18, 2010.

[64] H. Yu and S. S. Girimaji, "Near-field turbulent simulations of rectangular jets using lattice Boltzmann method," Physics of Fluids, vol. 17, no. 12, pp. 125106(1-17), 2005.

[65] E. Laurendeau, J. P. Bonnet, P. Jordan and J. Delville, "Impact of fluidic chevrons on the turbulence structure of a subsonic jet," in 3rd AIAA Flow Control Conference, San Francisco, 2006.

[66] M. Mancinelli, T. Pagliaroli, A. D. Marco, R. Camussi and T. Castelain, "Wavelet decomposition of hydrodynamic and acoustic pressures in the near field of the jet," Journal of Fluid Mechanics, vol. 813, pp. 716-749, 2017.

[67] G. Brès, F. Pérot and D. Freed, "Properties of the Lattice Boltzmann Method for Acoustics," 15th AIAA/CEAS Aeroacoustics Conference (30th AIAA Aeroacoustics Conference), pp. 1-11, 2009.

[68] H. Tanna, "An experimental study of jet noise part I: Turbulent mixing noise," Journal of Sound and Vibration, vol. 50, no. 3, pp. 405-428, 1977.

[69] C. Morfey, V. Szewczyk and B. Tester, "New scaling laws for hot and cold jet mixing noise based on a geometric acoustics model," Journal of Sound and Vibration, vol. 61, no. 2, pp. 255-292 , 1978.

[70] A. Lyrintzis and R. Mankbadi, "On the prediction of the far-field jet noise using Kirchhoffs formulation," AIAA Journal, vol. 34, no. 2, pp. 413-416, 1996.

[71] M. Araghi and M. Yaghobi, "The study of noise pollution caused by Birjand airport on the surrounding residents," Indian Journal of Science and Technology, vol. 8, no. 11, pp. 1-7, 6 2015.

[72] E. K. Lawrence, R. F. Austin, B. C. Alan and V. S. James, Fundamentals of Acoustics, 4 ed., New York: John Wiley and Sons (WIE), 2000.

[73] C. H. Hansen, "FUNDAMENTALS OF ACOUSTICS," Occupational Exposure to Noise: Evaluation, Prevention and Control. World Health Organization, South Australia, 2001.

[74] B. E. Mitchell, S. K. Lele and P. Moin, "Direct computation of the sound generated by vortex pairing in an axisymmetric jet," Journal of Fluid Mechanics, vol. 383, pp. 113-142, 3 1999.

[75] P. Geert, "Airport Noise Pollution," 2013.

[76] D. Caridi, Industrial CFD Simulation of Aerodynamic Noise, PhD Thesis: University of Naples Federico II, 2008.

[77] V. Kraz, "Near-Field Methods of Locating EMI Sources," Compliance Engineering Magazine , pp. 1-7, 6 1995.

[78] M. Gorji-Bandpy and M. Azimi, "Technologies for jet noise reduction in turbofan engines," Aviation, vol. 16, no. 1, pp. 25-32, 3 2012.

[79] S. W. Rienstra and A. Hirschberg, "An Introduction to Acoustics," S.W. Rienstra & A. Hirschberg, North Brabant, 2004.

[80] H. M. Tanna, P. Dean and M. Fisher, "Effect of temperature on supersonic jet noise," in Aeroacoustics Conference AIAA, Seattle,WA,U.S.A., 1973.

[81] M. Harper-Bourne, "On Modelling the Near-Field Noise of the High-speed Jet Exhausts of Combat Aircraft," Breckenridge Colorado, 2002.

[82] C. Bogey, S. Barré, V. Fleury, C. Bailly and D. Juvé, "Experimental Study of the Properties of Near-Field and Far-Field Jet Noise," International Journal of Aeroacoustics, vol. 6, pp. 73-93, 2007.

[83] C. Loh, L. Hultgren and P. Jorgenson, "Near-Field Noise Computation for a Subsonic Coannular Jet," in 13th AIAA/CEAS Aeroacoustics Conference (28th AIAA Aeroacoustics Conference), Rome, Italy, 2007.

[84] D. J. Bodony and S. K. Lele, "Current Status of Jet Noise Predictions Using Large-Eddy Simulation," AIAA Journal, vol. 46, no. 2, pp. 364-380, 2008.

[85] S. A. E. Miller, "Prediction of Near-Field Jet Cross Spectra," AIAA Journal, vol. 53, no. 8, pp. 2130-2150, 2015.

[86] R. Kumar, A. Krothapalli and B. Greska, "Near-field Noise Characteristics of a Pulse Jet," in 14th AIAA/CEAS Aeroacoustics Conference (29th AIAA Aeroacoustics Conference), Vancouver, British Columbia Canada, 2008.

[87] S. Saxena and P. Morris, "Noise Predictions for High Subsonic Single and Dual-Stream Jets in Flight," in 18th AIAA/CEAS Aeroacoustics Conference (33rd AIAA Aeroacoustics Conference), Colorado Springs, 2012.

[88] H. Yu and S. S. Girimaji, "Near-field turbulent simulations of rectangular jets using lattice Boltzmann method," Physics of Fluids, vol. 17, no. 12, pp. 125106-1-17, 2005.

[89] G. Brès, F. Pérot and D. Freed, "A Ffowcs Williams - Hawkings Solver for Lattice-Boltzmann Based Computational Aeroacoustics," in 16th AIAA/CEAS Aeroacoustics Conference, Exa Corporation, Brisbane, USA, 2010.

[90] D. Casalino and S. K. Lele, "Lattice-Boltzmann simulation of coaxial jet noise generation," Center for Turbulence Research, 2014.

[91] J. Lei, X. Wang and G. Xie, "High Performance Computation of a Jet in Crossflow by Lattice Boltzmann Based Parallel Direct Numerical Simulation," Mathematical Problems in Engineering, vol. 2015, pp. 1-11, 2015.

[92] Y. Koda and F.-S. Lien, "The Lattice Boltzmann Method Implemented on the GPU to Simulate the Turbulent Flow Over a Square Cylinder Confined in a Channel," Flow, Turbulence and Combustion, vol. 94, no. 3, pp. 495-512, 2015.

[93] A. P. Markesteijn and S. A. Karabasov, "GPU CABARET Solutions for the CoJen Jet Noise Experiment," in 2018 AIAA/CEAS Aeroacoustics Conference, Atlanta, Georgia, 2018.

[94] B. Lyu and A. Dowling, "Noise Prediction for Installed Jet," Journal of Fluid Mechanics, vol. 881, pp. 234-268, 2017.

[95] S. Barré, V. Fleury, C. Bogey and C. Bailly, "Experimental Study of the Properties of Near-Field and Far-Field Jet Noise," in 12th AIAA/CEAS Aeroacoustics Conference (27th AIAA Aeroacoustics Conference), Ecully, France, 2006.

[96] A. Khavaran and J. Bridges, "Development of Jet Noise Power Spectral Laws Using SHJAR Data," in 15th AIAA/CEAS Aeroacoustics Conference (30th AIAA Aeroacoustics Conference), Miami,Florida, 2009.

[97] I. Pribec, T. Urbic and I. Plazl, "Modelling Reaction-Diffusion Dynamics in Microsystems," Computer Aided Chemical Engineering, vol. 38, pp. 1623-1628, 2016.

[98] O. Filippova and D. Hänel, "Grid refinement for Lattice-BGK models," Journal of Computational Physics, vol. 147, no. 1, pp. 219-228, 11 1998.

[99] D. P. Lockard, "A Comparison of Ffowcs Williams-Hawkings Solvers for Airframe Noise Applications," in 8th AIAA/CEAS Aeroacoustics Conference & Exhibit, Breckenridge, Colorado, 2002.

[100] Y. B. Bao and J. Meskas, "Lattice Boltzmann Method for Fluid Simulations," in 6th Annual IRMACS Day, 2011.

[101] W. Feng, B. He, A. Song, Y. Wang, M. Zhang and W. Zhang, "Compressible lattice Boltzmann method and applications," in International journal of numerical analysis and modeling, Shanghai, China, 2010.

Appendices

Appendix A

Maxwell distribution function

$$f^{eq}(\rho,u,\theta)=\rho(2\pi\theta)^{(-D/2)}e^{\left[-\frac{(c-u)^2}{2\theta}\right]} \qquad \text{(A. 1a)}$$

The special dimension $D=3$, and $\theta=RT$

$$f_i^{eq}(\rho,u,\theta)=\rho\left(\frac{1}{2\pi\theta}\right)^{3/2}e^{\left[-\frac{(c_i-u)^2}{2\theta}\right]} \qquad \text{(A. 1b)}$$

The Taylor series for the exponential term $e^{\left[-\frac{(c-u)^2}{2\theta}\right]}$ using Maple Software:

```
> taylor(exp(-x^2), x=0, 18);
```

$$1-x^2+\frac{1}{2}x^4-\frac{1}{6}x^6+\frac{1}{24}x^8-\frac{1}{120}x^{10}+\frac{1}{720}x^{12}-\frac{1}{5040}x^{14}+\frac{1}{40320}x^{16}+O(x^{18})$$

```
> exp(-(c[i]-u)^2/(2*theta));
```

$$e^{-\frac{(c_i-u)^2}{2\theta}}$$

Third-order

```
> g := taylor(exp(-(c[i]-u)^2/(2*theta)), u=0, 3);
```

$$e^{-\frac{c_i^2}{2\theta}}+\frac{e^{-\frac{c_i^2}{2\theta}}c_i}{\theta}u-\frac{1}{2}\frac{e^{-\frac{c_i^2}{2\theta}}(-c_i^2+\theta)}{\theta^2}u^2+O(u^3)$$

Fourth-order

$$> \; g : taylor\left(\exp\left(-\frac{(c[i]-u)^2}{2\cdot \text{theta}}\right), u=0, 4\right);$$

$$e^{-\frac{c_i^2}{2\theta}} + \frac{e^{-\frac{c_i^2}{2\theta}} c_i}{\theta} u - \frac{1}{2} \frac{e^{-\frac{c_i^2}{2\theta}} \left(-c_i^2+\theta\right)}{\theta^2} u^2 - \frac{1}{6} \frac{e^{-\frac{c_i^2}{2\theta}} c_i \left(-c_i^2+3\,\theta\right)}{\theta^3} u^3 + O(u^4)$$

Fifth-order

$$> \; g : taylor\left(\exp\left(-\frac{(c[i]-u)^2}{2\cdot \text{theta}}\right), u=0, 5\right);$$

$$e^{-\frac{c_i^2}{2\theta}} + \frac{e^{-\frac{c_i^2}{2\theta}} c_i}{\theta} u - \frac{1}{2} \frac{e^{-\frac{c_i^2}{2\theta}} \left(-c_i^2+\theta\right)}{\theta^2} u^2 - \frac{1}{6} \frac{e^{-\frac{c_i^2}{2\theta}} c_i \left(-c_i^2+3\,\theta\right)}{\theta^3} u^3 + \frac{1}{24} \frac{e^{-\frac{c_i^2}{2\theta}} \left(c_i^4-6\,\theta\, c_i^2+3\,\theta^2\right)}{\theta^4} u^4 + O(u^5)$$

Sixth-order

$$> \; g : taylor\left(\exp\left(-\frac{(c[i]-u)^2}{2\cdot \text{theta}}\right), u=0, 6\right);$$

$$e^{-\frac{c_i^2}{2\theta}} + \frac{e^{-\frac{c_i^2}{2\theta}} c_i}{\theta} u - \frac{1}{2} \frac{e^{-\frac{c_i^2}{2\theta}} \left(-c_i^2+\theta\right)}{\theta^2} u^2 - \frac{1}{6} \frac{e^{-\frac{c_i^2}{2\theta}} c_i \left(-c_i^2+3\,\theta\right)}{\theta^3} u^3 + \frac{1}{24} \frac{e^{-\frac{c_i^2}{2\theta}} \left(c_i^4-6\,\theta\, c_i^2+3\,\theta^2\right)}{\theta^4} u^4 + \frac{1}{120} \frac{e^{-\frac{c_i^2}{2\theta}} c_i \left(c_i^4-10\,\theta\, c_i^2+15\,\theta^2\right)}{\theta^5} u^5 + O(u^6)$$

Seventh-order

$$> \; g := taylor\left(\exp\left(-\frac{(c[i]-u)^2}{2\cdot \text{theta}}\right), u=0, 7\right);$$

$$e^{-\frac{c_i^2}{2\theta}} + \frac{e^{-\frac{c_i^2}{2\theta}} c_i}{\theta} u - \frac{1}{2}\frac{e^{-\frac{c_i^2}{2\theta}}\left(-c_i^2+\theta\right)}{\theta^2} u^2 - \frac{1}{6}\frac{e^{-\frac{c_i^2}{2\theta}} c_i\left(-c_i^2+3\theta\right)}{\theta^3} u^3$$
$$+ \frac{1}{24}\frac{e^{-\frac{c_i^2}{2\theta}}\left(c_i^4-6\theta c_i^2+3\theta^2\right)}{\theta^4} u^4 + \frac{1}{120}\frac{e^{-\frac{c_i^2}{2\theta}} c_i\left(c_i^4-10\theta c_i^2+15\theta^2\right)}{\theta^5} u^5$$
$$- \frac{1}{720}\frac{e^{-\frac{c_i^2}{2\theta}}\left(-c_i^6+15\theta c_i^4-45\theta^2 c_i^2+15\theta^3\right)}{\theta^6} u^6 + O(u^7)$$

Appendix B

Chapman-Enskog Expansion

The Chapman-Enskog expansion can be used for recovering the Navier-Stokes equations from the LBE. For simplicity, the SRT-LBE with the BGK collision operator is used.

$$f_i(\vec{x}+\vec{c}_i, t+1) + f_i(\vec{x}, t) - \frac{1}{\tau}\left(f_i - f_i^{eq}\right) \qquad \text{(B. 1)}$$

The incompressible Navier-Stokes equations can be recovered from this equation through the Chapman-Enskog analysis, which is essentially a formal multiple scaling expansion:

$$f_i = f_i^{(0)} + \epsilon f_i^{(1)} + \epsilon^2 f_i^{(2)} + \cdots \quad \text{(B. 2a)}$$

$$\frac{\partial}{\partial t} = Kn\frac{\partial}{\partial t_1} + Kn^2\frac{\partial}{\partial t_2}, \quad \text{(B. 2b)}$$

$$\frac{\partial}{\partial x} = Kn\frac{\partial}{\partial x_1}, \quad \text{(B. 2c)}$$

The expansion parameter ϵ, is the Knudsen number, defined as the ratio between the mean free path of a gas molecule and a macroscopic length scale.

$$Kn = \frac{\lambda}{L} \quad \text{(B. 3a)}$$

where λ is the mean free path and L is the representative physical length scale.

For the Boltzmann gas, the mean free path is calculated through

$$Kn = \frac{k_B T}{\sqrt{2}\pi d^2 pL} \quad \text{(B. 3b)}$$

where k_B is the Boltzmann constant, T is the temperature, d is the particle diameter, and p is the total pressure.

For particle dynamics in the atmosphere, at a temperature of 25 °C and a pressure of 1 atm,

$$\lambda \approx 8 \times 10^{-8} m$$

The non-dimensional relaxation time λ has the same scaling as the Knudsen number.

$$\hat{\tau} = \frac{\tau}{\Delta t} \sim \frac{\frac{l}{c_0}}{\frac{L}{c_0}} = \frac{l}{L} = Kn \tag{B. 3c}$$

From Eq. (B.1) the lattice Boltzmann equation can be written as

$$\Delta t \left(\frac{\partial}{\partial t} + \xi_{i\alpha} \frac{\partial}{\partial x_\alpha}\right) f_i + \frac{\Delta t^2}{2} \left(\frac{\partial}{\partial t} + \xi_{i\alpha} \frac{\partial}{\partial x_\alpha}\right)^2 f_i + \frac{1}{\hat{\tau}} \left(f_i - f_i^{eq}\right) + O(\Delta t^3) = 0 \tag{B. 4}$$

Using this technique, the particle distribution function f_i can be expanded about the local equilibrium function f_i^{eq} as

$$f_i = f_i^{eq} + Kn f_i^{neq} \tag{B. 5}$$

where f_i^{eq} is defined from the Maxwell equilibrium function as

$$f_i^{eq} = \rho\omega_i\left(1 + \frac{1}{c_s^2}\vec{c}_i.\vec{u} + \frac{1}{2c_s^2}Q_i:\vec{u}\vec{u}\right) \quad \text{(B. 6)}$$

and this equation must satisfy

$$\sum_{i=0}^{q-1} f_i^{eq} = \rho \quad \text{(B. 7a)}$$

$$\frac{1}{\rho}\sum_{i=0}^{q-1} \vec{c}_i f_i^{eq} = \vec{u} \quad \text{(B. 7b)}$$

The non-equilibrium distribution function

$$f_i^{neq} = f_i^1 + Knf_i^2 + \mathcal{O}(Kn^2) \quad \text{(B. 8)}$$

has the following constraints to ensure conservation of mass and momentum in the collision operator:

$$\sum_{i=0}^{q-1} f_i^{neq} = 0 \quad \text{(B. 9a)}$$

$$\sum_{i=0}^{q-1} \vec{c}_i f_i^{neq} = 0 \quad \text{(B. 9b)}$$

The collision operator for the BGK model is

$$\Omega_i = \frac{1}{\tau}(f_i - f_i^{eq}) \tag{B. 10}$$

The Taylor series is expanded and rewritten in the consecutive order of Kn as

$$f_i^0 = f_i^{eq}: \quad \mathcal{O}(Kn^0) \tag{B. 11}$$

$$(\partial_{t0} + \vec{c}_i.\nabla)f_i^0 = -\frac{1}{\tau}f_i^1: \quad \mathcal{O}(Kn^1) \tag{B. 12}$$

$$\partial_{t1}f_i^0 + \left(\frac{2\tau - 1}{2\tau}\right)(\partial_{t0} + \vec{c}_i.\nabla)f_i^1 = -\frac{1}{\tau}f_i^2: \quad \mathcal{O}(Kn^2) \tag{B. 13}$$

Using the constraints shown in Eq. (B. 6) to (B. 9), and summing the first-order expansion (Eq. (B. 12)) for all i, the continuity equation can be obtained as

$$\frac{\partial \rho}{\partial t} + \nabla.\rho\vec{u} = 0 \tag{B. 14}$$

Multiplying by $\vec{c}$ on both sides of Eq. (B. 12) and (B. 13) and combining them enables the momentum equation to be derived as

$$\frac{\partial(\rho\vec{u})}{\partial t} + \nabla.\left(\Pi^0 + \frac{2\tau - 1}{2\tau}\Pi^1\right) = 0 \tag{B. 15}$$

Multiplying Eq. (B. 12) by $\vec{c}_i$ gives

$$\vec{c}_i(\partial_{t0} + \vec{c}_i.\nabla)f_i^0 = \vec{c}_i * \frac{-1}{\tau} f_i^1: \tag{B. 16}$$

$$\frac{\partial(\rho\vec{u})}{\partial t} + \nabla.\left(p\delta_{\alpha\beta} + \rho u_\alpha u_\beta + \frac{2\tau - 1}{2\tau}\nu\left(\nabla_\alpha(\rho u_\beta) + \left(\nabla_\beta \rho u_\alpha\right)\right)\right) = 0 \tag{B. 17}$$

where Π^0 and Π^1 are momentum flux tensors defined as

$$\Pi^0 = \sum_{i=0}^{q-1} \vec{c}_i \vec{c}_i f_i^0 = p\delta_{\alpha\beta} + \rho u_\alpha u_\beta \tag{B. 18a}$$

$$\Pi^1 = \sum_{i=0}^{q-1} \vec{c}_i \vec{c}_i f_i^1 = \nu\left(\nabla_\alpha\left(\rho u_\beta\right) + \nabla_\beta(\rho u_\alpha)\right) \tag{B. 18b}$$

where p is the pressure and is related to the speed of sound and density as follows:

$$p = c_s^2 \rho = \frac{1}{3}\rho \tag{B. 18c}$$

The resulting momentum equation becomes

$$\rho\left(\frac{\partial\vec{u}}{\partial t}+\vec{u}.\nabla\vec{u}\right)=-\nabla p+\rho\nu\nabla^2\vec{u} \qquad \text{(B. 19)}$$

which is identical to the Navier-Stokes equations.

Appendix C

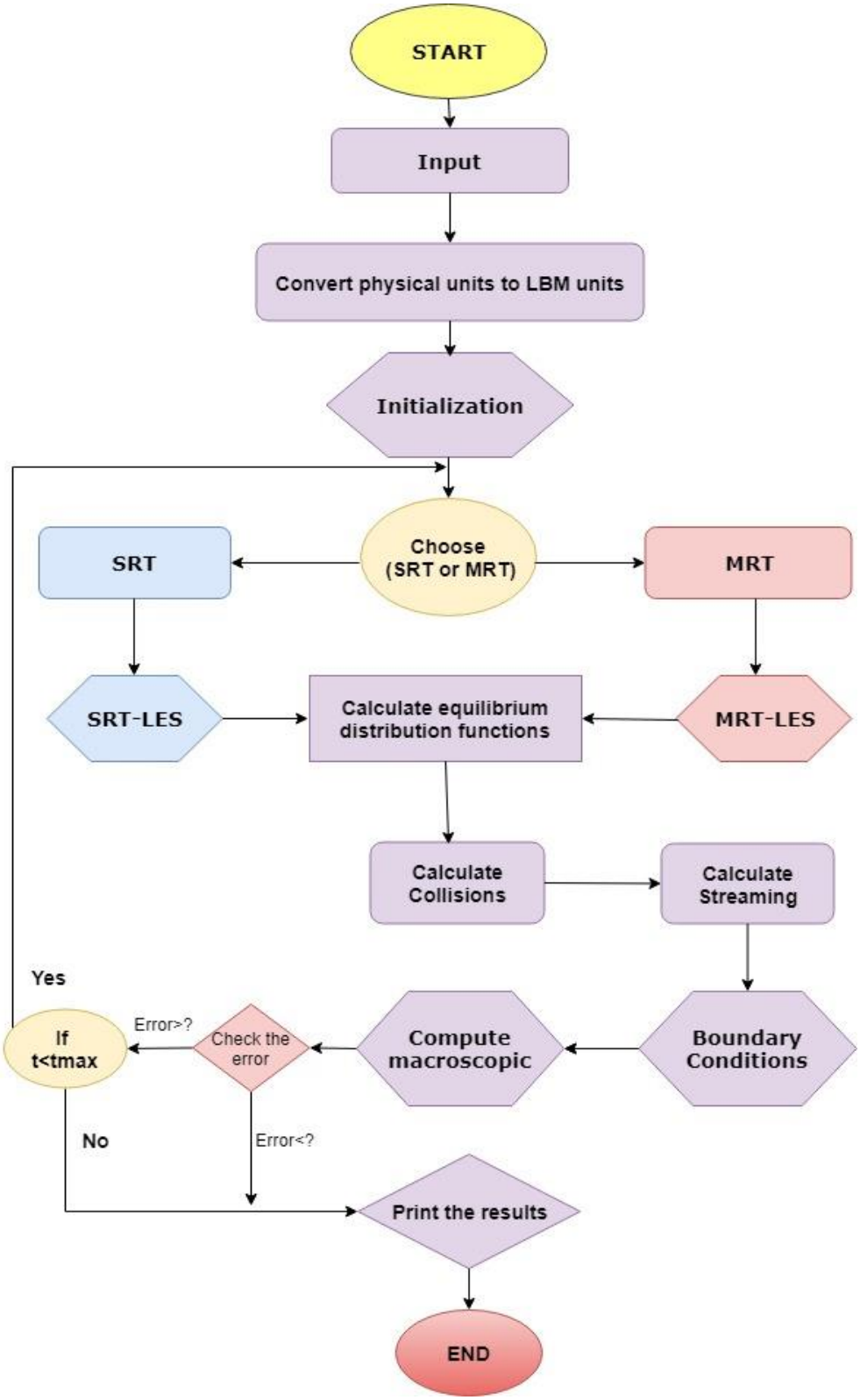

Simulation flowchart for the LBM-LES model

Computer system information

PC1:

Processor: Intel(R) Core(TM) i7-6700HQ CPU @ 2.60GHz, 2592 Mhz, 4 Core(s), 8 Logical Processor(s).

Installed Physical Memory: random access memory (RAM) 12.0 GB.

GPU: NVIDIA GeForce 940M, 4GB(DDR3).

PC 2:

Processor: Intel(R) Core(TM) i7-6700 CPU @ 3.40GHz, 3408 Mhz, 8 Cores, 8 Logical Processors.

Installed Physical Memory: random access memory (RAM) 16.0 GB.

GPU: Radeon R7 360 / R9 360 OEM, 2GB(DDR3).

Sharcnet graham cluster

Nods: 801-803:

56 cores

4 sockets x 14 cores per socket

Intel E7-4850 v3 (Haswell) @ 2.2 GHz

Memory: 3072.0 GB

Local storage: 1.2 TB

Nods: 828-987:

32 cores

2 sockets x 16 cores per socket

Intel E5-2683 v4 (Broadwell) @ 2.1 GHz

Notes: Accelerated compute nodes with 2 × NVIDIA Pascal P100 GPUs (12GB HBM2)

Memory: 128.0 GB

Local storage: 800 TB

LBM-LES C++ Code

Input subroutines

*LBM_Input.h

```
#include <vector>
using namespace std;

string casename ("SJ_case400-test1");
// The real problem
// A pipe with a length of L=0.508 m and a diameter of Dj=0.0508 m
// Uj=100 m/s  the jet centerline velocity at the exit of the pipe reaches approximately 130 m/s
const double Nuj = 1.81*10e-5;
const double Lj = 0.508;
const double Dj = 0.0508;
const double LjDj = Lj/Dj;   //=10
const double Ujin = 100;
const double Uj = 1.3*Ujin;
const double Re = Uj*Dj/Nuj; /// Re=6000

//Simulation Parameters
const double ObstR= 4;  /// the jet radius 4.572cm
const int D = ObstR*2;

const double CharLength = ObstR*2;
const double Mj = 0.30;
const double uMax = Mj;
double nu = uMax*(CharLength)/Re;
double omega1 = 1.0/(3.0*nu+0.5);

const int xDim = 20*D+1;   /// X = 30*ObstR
const int yDim = 8*D+1;   /// Y = 6*ObstR
const int zDim = 8*D+1;   /// Z = 6*ObstR
const int bdry=2;
const int NGRID=xDim*yDim*zDim;
const int surfaceXDim = (yDim*zDim);
const int surfaceYDim = (xDim*zDim);
const int surfaceZDim = (xDim*yDim);
const int xaDim = 20*D+1;   /// X = 60*ObstR
const int yaDim = 10*D+1;   /// Y = 72*ObstR
const int zaDim = 10*D+1;   /// Z = 80*ObstR*D

```

Ln 8, Col 31

Multidimensional Pointer Arithmetic in C++ for building the 3D dimensions

```
137
138     Node **** Grid;
139     Grid = new Node *** [xaDim];
140     for(i = 0; i<xaDim; i++){
141         Grid[i] = new Node ** [yaDim];
142         for(j = 0; j<yaDim; j++){
143             Grid[i][j] = new Node * [zaDim];
144             for(k = 0; k<zaDim; k++){
145                 Grid[i][j][k] = new Node();
146             }
147         }
148     }
149
```

```
165
166     double *** vort_i;
167     double *** vort_j;
168     double *** vort_k;
169     vort_i = new double ** [xDim];
170     vort_j = new double ** [xDim];
171     vort_k = new double ** [xDim];
172     for(i = 0; i<xDim; i++){
173         vort_i[i] = new double * [yDim];
174         vort_j[i] = new double * [yDim];
175         vort_k[i] = new double * [yDim];
176         for(j = 0; j<yDim; j++){
177             vort_i[i][j] = new double [zDim];
178             vort_j[i][j] = new double [zDim];
179             vort_k[i][j] = new double [zDim];
180             for(k = 0; k<zDim; k++){
181                 vort_i[i][j][k] = 0;
182                 vort_j[i][j][k] = 0;
183                 vort_k[i][j][k] = 0;
184             }
185         }
186     }
187
```

The monitoring parameters (while the code is running)

```
355     cout<<"\nCPU Number: "<<nCPU<<"\n\n";
356     cout<<"\nCASE NAME: "<<casename<<"\n\n";
357     cout<<"\nSIMULATION PARAMETERS:\n\n";
358     cout<<"xDim:\t"<<xDim<<"\n";
359     cout<<"yDim:\t"<<yDim<<"\n";
360     cout<<"zDim:\t"<<zDim<<"\n";
361     cout<<"NGRID:\t"<<NGRID<<"\n";
362     cout<<"jet radius :\t"<<ObstR<<"\n\n";
363     cout<<"Re:\t"<<Re<<"\n";
364     cout<<"uMax:\t"<<uMax<<"\n";
365     cout<<"CharLength:\t"<<CharLength<<"\n";
366     cout<<"D2Q9i:\t"<<D2Q9i<<"\n";
367     cout<<"MRT:\t"<<MRT<<"\n";
368     cout<<"LES:\t"<<LES<<"\n";
369     cout<<"SaveState:\t"<<SaveState<<"\n";
370     cout<<"Periodics:\t"<<Periodics<<"\n";
371     cout<<"InitPerturb:\t"<<InitPerturb<<"\n";
372     cout<<"InitCond:\t"<<InitCond<<"\n";
373     cout<<"U_fluct:\t"<< Random_U<<"\n";
374     cout<<"V_fluct:\t"<< Random_V<<"\n";
375     cout<<"W_fluct:\t"<< Random_W<<"\n";
376     //cout<<"StartRec:\t"<<StartRec<<"\n";
377     cout<<"tMax:\t"<<tMax<<"\n";
378     cout<<"StartAvg:\t"<<StartAvg<<"\n";
379     cout<<"Start Turbulence calculation:\t"<<TurbRec<<"\n";
380     cout<<"Start velocity recording :\t"<<VelRec<<"\n";
381
```

Calculations of the flow parameters

```
1258    ///==============================
1259    double i_vor= vort_i[i][j][k];
1260    double j_vor=vort_j[i][j][k];
1261    double k_vor=vort_k[i][j][k];
1262    ///==============================
1263    double drho_i= drhodt_i[i][j][k];
1264    double drho_x = drho_i;
1265    double drho_k= drhodt_k[i][j][k];
1266    double ux = Grid[i][j][k]->ux;
1267    double ui = Grid[i][j][k]->ux/uMax;
1268    double vi = Grid[i][j][k]->uy/uMax;
1269    double wi = Grid[i][j][k]->uz/uMax;
1270    double T  = Grid[i][j][k]->T;
1271    double uxavg = Grid[i][j][k]->uxavg; //// U/Uj
1272    double U = Grid[i][j][k]->uxavg/uMax; //// U/Uj
1273    double V = Grid[i][j][k]->uyavg/uMax; //// U/Uj
1274    double W = Grid[i][j][k]->uzavg/uMax; //// U/Uj
1275    double Vel_tot = Grid[i][j][k]->Vel_tot; //// U/Uj
1276    double Urms  = (sqrt(Grid[i][j][k]->uxflavg))/uMax; /// urms/uj
1277    double Vrms  = (sqrt(Grid[i][j][k]->uyflavg))/uMax; /// vrms/uj
1278    double Wrms  = (sqrt(Grid[i][j][k]->uzflavg))/uMax; /// vrms/uj
1279    double ReSt  = (Grid[i][j][k]->uxuyflavg)/(uMax*uMax);                  //// reynold stress uv/uj*uj
1280    double kturb = 0.5*(Grid[i][j][k]->uxflavg + Grid[i][j][k]->uyflavg + Grid[i][j][k]->uzflavg); /// turbulence kinetic energy
1281    double Rhoo = Grid[i][j][k]->rho;
1282    double UVrms;
1283    double Minf= Grid[i][j][k]->Minf;
1284    double Mach = Grid[i][j][k]->ComputeMach(Grid[i][j][k]->Vel_tot);
1285    double Pt_id =Grid[i][j][k]->Pt_id;
1286    double Pfl = Grid[i][j][k]->ComputePfl(Grid[i][j][k]->ux);
1287    double DPa = Grid[i][j][k]->ComputeDPa(Grid[i][j][k]->Vel_tot);
1288    double DPavg = Grid[i][j][k]->ComputeDPavg(Grid[i][j][k]->uxavg);
1289    double Pwav = Grid[i][j][k]->Pwav;
1290
```

LBM-LES

```
397
398    if(MRT == true && LES==true ){
399        //PI is the Strain rate tensor
400        double PI11 = -1.0/38.0*(s1*(m[1]-meq[1])+19.0*omega1*(m[9]-meq[9]));
401        double PI22 = -1.0/76.0*(2.0*s1*(m[1]-meq[1])-19.0*(omega1*(m[9]-meq[9])-3.0*omega1*(m[11]-meq[11])));
402        double PI33 = -1.0/76.0*(2.0*s1*(m[1]-meq[1])-19.0*(omega1*(m[9]-meq[9])+3.0*omega1*(m[11]-meq[11])));
403        double PI12 = -1.5*omega1*(m[13]-meq[13]);
404        double PI23 = -1.5*omega1*(m[14]-meq[14]);
405        double PI13 = -1.5*omega1*(m[15]-meq[15]);
406        nux = ((1.0/omega1)-0.5)/3.0;
407        Smag = sqrt(2.0*(PI11*PI11+PI22*PI22+PI33*PI33+2.0*(PI12*PI12+PI23*PI23+PI13*PI13)));///
408    }
409
```

Time-averaged velocity

```
614
615  double Node::VelAverage(int tStep)
616  {
617      uxavg = uxavg*(tStep-StartAvg)/(tStep-StartAvg+1)+ux/(tStep-StartAvg+1);
618      uyavg = uyavg*(tStep-StartAvg)/(tStep-StartAvg+1)+uy/(tStep-StartAvg+1);
619      uzavg = uzavg*(tStep-StartAvg)/(tStep-StartAvg+1)+uz/(tStep-StartAvg+1);
620       Vel_tot=sqrt( uxavg * uxavg + uyavg * uyavg + uzavg * uzavg );
621       DPavg = DPavg*(tStep-StartAvg)/(tStep-StartAvg+1)+DPa/(tStep-StartAvg+1);
622      drhoavg = drhoavg*(tStep-StartAvg)/(tStep-StartAvg+1)+drho/(tStep-StartAvg+1);
623              rhoavg= rho0+drhoavg;
624              rhoair=rhoavg*1.27;
625  }
626
```

Turbulence time-averaged velocity

```
637
638  void Node::TurbAverage(int tStep)
639  {
640    ////fluctuating velocity
641      uxfl= ux-uxavg;
642      uyfl= uy-uyavg;
643      uzfl= uz-uzavg;
644      uxuyfl= uxfl*uyfl;
645      DPafl= DPa-DPavg;
646      uxflavg  = uxflavg *(tStep-TurbRec)/(tStep-TurbRec+1)+ (uxfl*uxfl)/(tStep-TurbRec+1);
647      uyflavg  = uyflavg *(tStep-TurbRec)/(tStep-TurbRec+1)+ (uyfl*uyfl)/(tStep-TurbRec+1);
648      uzflavg  = uzflavg *(tStep-TurbRec)/(tStep-TurbRec+1)+(uzfl*uzfl)/(tStep-TurbRec+1);
649      uxuyflavg= uxuyflavg*(tStep-TurbRec)/(tStep-TurbRec+1)+uxuyfl/(tStep-TurbRec+1);
650      DPaflavg=  DPaflavg *(tStep-TurbRec)/(tStep-TurbRec+1)+(DPafl*DPafl)/(tStep-TurbRec+1);
651
652  }
653
```

Near-field noise

```
1348
1349    for(k = 0; k<zDim; k++){
1350        output9 << "val(:,:,"<<(k)<<")=";
1351        output9<<"\n";
1352        output13 << "val(:,:,"<<(k)<<")=";
1353        output13<<"\n";
1354        output14 << "val(:,:,"<<(k)<<")=";
1355        output14<<"\n";
1356        output15 << "val(:,:,"<<(k)<<")=";
1357        output15<<"\n";
1358    for(j = 0; j<yDim; j++){
1359    for(i = 0; i<xDim; i++){
1360      double PSD = Grid[i][j][k]->ComputePSD(Grid[i][j][k]->uxflavg);
1361      double SIL = Grid[i][j][k]->ComputeSIL(Grid[i][j][k]->ux);
1362      double SPLNF = Grid[i][j][k]->ComputeSPLNF(Grid[i][j][k]->DPavg);
1363     double Mach = Grid[i][j][k]->ComputeMach(Grid[i][j][k]->Vel_tot);
1364              output9 << PSD << "    ";
1365              output13 << SIL << "    ";
1366              output14 << SPLNF << "    ";
1367              output15 << Mach << "    ";
1368        }
1369              output9<<"\n";
1370              output13<<"\n";
1371              output14<<"\n";
1372              output15<<"\n";
1373    }}
1374
```

Building the Kirchhoff surface around the jet

```
1552        i = 0;
1553        // Extract Nodes for surface X
1554        for(j = 0; j<yDim; j++){
1555            for(k = 0; k<zDim; k++){
1556                gridSurfaceX[i] = &Grid[Xsur][j][k];
1557                /// cout << xDim-1 << ":" << j << ":" << k << endl;
1558                i++;
1559            }
1560        }
1561
1562        j = 0;
1563        // Extract Nodes for surface  Y
1564        for(i = 0; i<xDim; i++){
1565            for(k = 0; k<zDim; k++){
1566
1567                gridSurfaceY[j] = &Grid[i][Ysur][k];
1568                j++;
1569            }
1570
1571        }
1572
1573
1574        k = 0;
1575        // Extract Nodes for surface Z
1576        for(i = 0; i<xDim; i++){
1577            for(j = 0; j<yDim; j++){
1578                gridSurfaceZ[k] = &Grid[i][j][Zsur];
1579                k++;
1580            }
1581        }
1582
```

Far-field noise

```
1768
1769        for(k =(zDim-1)/2; k<(zDim-1)/2+1; k++){
1770                    output6<<"\n";
1771                    output6 << "val(:,:,"<<(k)<<")=";
1772                    output6<<"\n";
1773
1774        for(j = Ysur; j< Ra; j++){
1775        for(i = 1  ; i<(xDim-1); i++){
1776
1777         double SPL = Grid[i][j][k]->ComputeSPL(Grid[i][j][k]->pa);
1778                              output6 << SPL << " ";
1779                                 }
1780                              output6<<"\n";
1781                              }
1782
1783                          }
1784    //=============================================
```

```
1106
1107
1108    double Node::ComputeSPL(double pa)
1109    {
1110    SPL = abs(20*log10 (pa*100000/2));
1111    SPL= abs (SPL)<1.0*10e-15 ? 0:SPL;
1112    SPL= abs (SPL)>1.0*10e+15 ? 0:SPL;
1113    return SPL;
1114
1115    }
1116
```

Appendix D

GPU code

Set CUDA parameters

```
12  #define NUMGPU 1
13  #define BLOCKSIZEX 62     //64
14  #define BLOCKSIZEY 1      //1
15  #define BLOCKSIZEZ 1      //1
16  #define BLOCKSIZELRX 64
17  #define BLOCKSIZELRY 1
18  #define BLOCKSIZELRZ 1
19  #define BLOCKSIZEINTERP 8
20  #define XDIM 400   //450          60*D
21  #define YDIM 303   // 43    //60    15*D
22  #define ZDIM 64   //44    // 60    15*D
23  #define TMAX  40000
24  #define STARTF 0
25
26  #define OBSTR1 5.f
27  #define OBSTX1 50.5f
28  #define OBSTY1 20.5f
29  #define OBSTZ1 32.5f
30
31  #define OBSTR2 32.f
32  #define OBSTX2 319.5f
33  #define OBSTY2 511.5f
34  #define OBSTZ2 31.5f
35
36  #define LRFACTOR 0.5f
37  #define LRLEVEL 2
38  #define LRX0 30.25f    //minimum x coord of LR
39  #define XLRDIM 256    //number of nodes in x
40  #define LRY0 10.25f
41  #define YLRDIM 256
42  #define LRZ0 -0.75f
43  #define ZLRDIM 256
44  #define ORDER 2 //order of accuracy of interpolation
```

Input the flow parameters

```
66  const double Nuj = 1.81*10e-5; //; //1.1*10e-3;  ///1.81*10e-5;   // ;
67  const double Lj = 0.508;
68  const double Dj = 0.0508;
69  const double LjDj = Lj/Dj;   //=10
70  const double Ujin = 100;
71  const double Uj = 130;
72  //const double RE = Uj*Dj/Nuj; /// Re=6000
73  const double RE = 600000; /// Re=6000
74
75  const double CharLength = D;
76
77  ///#define RE 200.f//2000.f//100.f;
78  #define UMAX 0.35f
79  #define rhoIn 1.225f
80  double nu = UMAX*(CharLength)/RE;
81
82  #define SmagLES 1 //1,0
83  #define MODEL "MRT" //BGK,MRT,STREAM
84  #define REFINEMENT 0 //1,0
85  #define CS 0.02f
86
87
88  #define VELAV 1
89  #define START_VELAV   4000000
90  #define START_VELFLUC 8000000
91
```

The flow domain

```
115  inline __device__ int ImageFcn(int x, int y, int z)
116  {
117      int value = 0;
118
119      if ( x <= D){
120       if ( y>Ly1 && y<Ly2 && z>Lz1&& z<Lz2)
121    value = 400;//26;
122     else  value = 1;
123
124            }
125
126      if ( x <= D){
127       if ( y<=Ly1 && y>=Ly2 && z<=Lz1&& z>=Lz2)
128    value = 401;//26;
129            }
130
131      if(y == 0)
132          value = 1;//200;//22;
133      else if(y == YDIM-1)
134          value = 1;//100;
135
136      else if(x == XDIM-1)
137          value = 300;//25;
138      else if(z == 0)
139          value = 1;
140      else if(z > ZDIM-1)
141          value = 1;
142      return value;
143  }
144
```

Initialization

```
890  __global__ void initialize(float *fout, size_t pitch, int zInner, int GPU_N)
891  {
892      int x = threadIdx.x+blockIdx.x*blockDim.x;//coord in linear mem
893      int y = threadIdx.y+blockIdx.y*blockDim.y;
894      int z = threadIdx.z+blockIdx.z*blockDim.z;
895      float xcoord = x;
896      float ycoord = y;
897      float zcoord = z+1+GPU_N*ZDIM;
898      int j = x+y*pitch+z*YDIM*pitch;//index on padded mem (pitch in elements)
899      float f[19] = {0};
900      float m[19] = {0};
901
902      int im = ImageFcn(xcoord,ycoord,zcoord);
903      float u,v,w,rho;
904      rho = rhoIn;
905      u = 0.f;
906      v = 0.f;
907      w = 0.f;
908
909      if(im == 10 || im == 1){
910      u = 0.0f;
911      v = 0.0f;
912      w = 0.0f;
913      }
914
915
916      mrt_meq(m,rho,u,v,w);
917      InvertMoments(f,m);
918
919      for(int i = 0; i<19; i++)
920      fout[j+i *pitch*YDIM*zInner]=f[ i];
921  }
922
```

Appendix E

Basic Concepts in Acoustics and Noise

A propagating sound wave can be described as a pressure disturbance (fluctuation) in a fluid superposed to its mean pressure:

$$p' = \bar{p} + p \tag{E. 1}$$

where p is the fluid pressure, $\bar{p}$ represents the fluid mean pressure, and p'denotes the fluid fluctuation pressure.

The wavelength λ of the periodic pressure signal is defined as

$$\lambda = \frac{c}{f} \tag{E. 2}$$

where c is the speed of sound and f is the pressure frequency.

The sound pressure level (SPL) in dB is a logarithmic function that measures the fluid sound pressure relative to a reference pressure.

$$SPL = 10\log_{10}\left(\frac{p}{p_{ref}}\right)^2 = 20\log_{10}\left(\frac{p}{p_{ref}}\right) \tag{E. 3}$$

where p_{rms} is the root-mean-square sound pressure, and the reference sound pressure p_{ref} is typically the threshold of human hearing ($p_{ref} = 2 \times 10^{-5}$ pa).

The overall sound pressure level (SPL) in dB

$$OLSPL = 10\log_{10}\left(\frac{p_{rms}}{p_{ref}}\right)^2 = 20\log_{10}\left(\frac{p_{rms}}{p_{ref}}\right) \quad \text{(E. 4)}$$

were p_{rms} is root mean square velocity:

$$p_{rms} = \sqrt{\frac{\sum_n^N (p)^2}{N}}$$

The power spectral density per Strouhal number is

$$PSD = 10\log_{10}\left(\frac{p^2{}_{rms}U_j}{p^2{}_{ref}D}\right) \quad \text{(E. 5)}$$

The sound pressure in a frequency band is

$$SPL(f_c) = 20\,log\left[\frac{P_{\text{rms}}(f_c)}{P_{\text{ref}}}\right] \quad \text{(E. 6)}$$

where f_c is the band center frequency.